DOCTORAL DISSERTATION

# SYNTHESIS OF NANOSTRUCTURE-CONTROLLED SPHERICAL CARBON PARTICLES AND THEIR APPLICATION TO ENERGY STORAGE DEVICES

（ナノ構造が制御された球状炭素微粒子の合成とエネルギー貯蔵デバイスへの応用）

Written by

**Kiet Le Anh Cao**

Supervisor

Professor Takashi Ogi

Thermal Fluid Materials Engineering Laboratory

Department of Chemical Engineering

Graduate School of Engineering

Hiroshima University

July 2021

# Abstract

The fast-growing energy crises and depletion of fossil fuels as well as the emission of greenhouse gases lead to severe pollution of the environment. Therefore, the development of sustainable energy storage devices (*e.g.* batteries, supercapacitors) is very crucial for solving energy issues, which requires new and advanced materials as well as novel fabrication techniques in order to achieve high electrochemical performance. In recent years, the rational design and synthesis of nanostructured particulate materials in favorable morphologies have attracted significant attention. Among various materials with different morphologies, carbon spheres have received a great deal of interest due to their regular shape, low surface free energy, good fluidity, high packing density, and chemical stabilization.

The research covered in the scope of this dissertation is aimed to address the following objectives: (i) to develop the methodologies for design and synthesis of spherical carbon-based materials using soft template and template-free spray drying method, particularly the precisely tailored structure, pore texture, and surface properties, (ii) to provide a possible mechanism for obtaining an in-depth understanding of the particle formation of carbon-based materials, and (iii) to show how the morphology, pore size, and material composition may influence lithium-ion batteries (LIBs) and supercapacitors performance. This dissertation comprises five chapters, of which content is described briefly as follows.

**Chapter 1** summarizes the important properties of spherical carbon-based materials, the several synthetic strategies for producing carbon sphere materials with desirable structures and functionalities for energy storage applications, and the alternative material in response to the problem suffered by carbonaceous materials. This summary and problem statements lead to the motivation of the researches covered within the scope of this dissertation.

**Chapter 2** discusses the developed strategy for fabrication of carbon-coated $SiO_x$ ($SiO_x$@C core-shell) particles through a sol-gel method using the simultaneous hydrolysis-condensation of tetramethyl orthosilicate (TMOS) and polymerization of 3-aminophenol and formaldehyde followed by the carbonization process. The core−shell particles can be obtained with a well-controlled reaction rate and spherical morphology by using TMOS as an excellent

silica precursor for the first time instead of the traditionally used tetraethyl orthosilicate (TEOS). When used as the anode material for LIBs, the obtained $SiO_x$@C core–shell particles exhibited a reversible capacity of 509.2 mAh $g^{-1}$ at 100 mA $g^{-1}$ and the capacity retention was approximately 80% after 100 cycles. The significantly improved electrochemical performance due to the morphology and structure of the material.

**Chapter 3** focuses on the synthesis of spherical carbon particles derived from Kraft lignin via the spray drying method followed by the carbonization process. The developed synthetic strategy is highly significant because it allows the utilization of lignin as an abundant and sustainable carbon precursor. The carbon particles generated in this study could be obtained with spherical morphologies and it could be precisely controlled from dense to hollow sphere by varying the potassium hydroxide (KOH) concentration. In addition, to get a better understanding of the particle formation of carbon particles, a plausible mechanism has been discussed in detail, which provides insights with regard to the exploration of lignin-derived carbon materials. The resulting spherical carbon particles exhibited dense structures with a specific surface area (1233 $m^2$ $g^{-1}$) and tap density (1.46 g $cm^{-3}$) superior to those of irregular shape carbon particles. The carbon sphere particles having a high tap density as advanced materials can endow them for a broad prospect of applications in the areas of colloids and interface science as well as sustainable development.

**Chapter 4** provides the characterization of hollow carbon spheres (HCSs) derived from Kraft lignin with their structural, pore texture, surface morphology, and electrochemical performance for supercapacitors. HCSs with high specific surface area up to 2424.8 $m^2$ $g^{-1}$ and micro-mesoporous structure were obtained at low KOH-to-lignin mass ratios (below 1.5), which was in accordance with green chemistry principles. In addition, these HCSs can be used as electrode materials in supercapacitors for energy storage applications. This newly developed synthetic process is expected to lead an advanced carbon material and the value-added utilization of Kraft lignin.

**Chapter 5** provides a summary of all chapters and suggestions for future research.

# Contents

# List of Figures

# List of Tables

Chapter 1

# Introduction

## 1.1. Electrochemical energy storage devices

In recent years, the emission of greenhouse gases has been widely recognized as one of the main causes with a strong link to global climate change, which affects our daily life and becomes a serious issue influencing the survival of all living species [1]. Therefore, it is highly crucial to develop renewable and green energy technologies for a sustainable future to mitigate the worst impacts of greenhouse gas emissions, climate change, and global warming. Until now, numerous intensive research efforts are focused on the development of low-cost and environmentally friendly energy storage devices with high electrochemical performance, including rechargeable batteries (especially lithium-ion batteries (LIBs)) and supercapacitors [2,3].

Rechargeable battery technology is attracting interest due to the ability to balance capacity with discharge rate compared to other electrochemical energy storage [4]. Since the commercialization of LIBs released by Sony in 1991, LIBs have served as one of the state-of-the-art storage techniques in many fields, such as portal electronic devices, electrical tools, and electric vehicles [5,6]. LIBs offer higher energy and power densities, longer life expectancy, and lower self-discharge rate, and they can be smaller and lighter than other batteries. Li is the lightest metal and most powerful reducing element, with a theoretical electrochemical capacity of 3860 mAh g$^{-1}$ [7]. **Figure 1.1 (a)** depicts the representative configuration of LIBs. The LIBs operate by moving Li ions from the anode to the cathode during discharge and in the opposite direction during the charge. This battery involves insertion reactions at both electrodes during the charge–discharge process. Thus, the anode material (graphite) can intercalate Li, and the accommodation of Li between graphene layers results in a maximum configuration of $LiC_6$ with a theoretical capacity of 372 mAh g$^{-1}$. The cathode is generally a mixed oxide material, such as $Li_xCoO_2$, which can intercalate Li ions [8].

1

Apart from the rechargeable batteries mentioned above, supercapacitors are another critical member of electrochemical energy storage family and are widely used in portable electronics or hybrid electric vehicles [9]. Compared with LIBs in delivering outstanding energy densities and relatively large specific capacities, supercapacitors usually offer higher power densities, better cycling stability, and faster charge–discharge processes within seconds [10,11]. Accordingly, supercapacitors are classified on the basis of charge storage mechanisms (*e.g.* electrochemical double-layer capacitors (EDLCs) and pseudocapacitors). The EDLCs store energy by physical charge separation at the interfaces between the electrodes and electrolytes, without involving chemical reactions during charging–discharging processes, while pseudocapacitors store the electrical energy by a series of reversible redox reactions. EDLCs usually have high charge–discharge rates and long cycling performance, whereas pseudocapacitors have much larger storage capabilities due to the chemical reactions involved (**Figure 1.1 (b)** and **(c)**) [12].
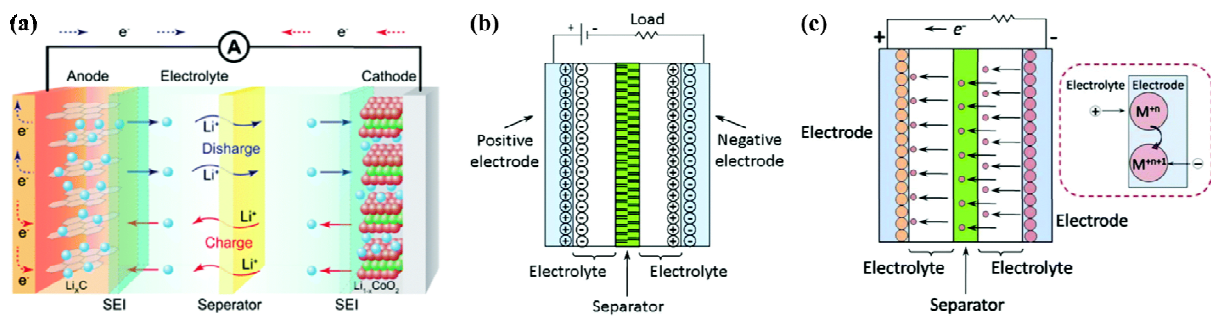


**Figure 1.1.** Representative scheme of (a) LIB, (b) EDLC type, and (c) pseudocapacitor type. Adapted from [8,12].

The energy and power densities of different electrochemical energy conversion systems are presented by the Ragone plot (**Figure 1.2**). This plot indicates that the fuel cells are high-energy systems, whereas supercapacitors are high-power systems. Batteries have intermediary power and energy capabilities. There exists some overlap in energy density and power density of fuel cells and supercapacitors with batteries. In addition, it is apparent from the figure that any single electrochemical device cannot compete with an internal combustion engine [13]. Therefore, the energy and power densities of electrochemical devices have to be increased to compete with the combustion engine. So far, the improvement has been focused mainly on the

development of the electrode material. The concern is not only limited to the electrode materials selection and functionalization, but also the morphological structure.
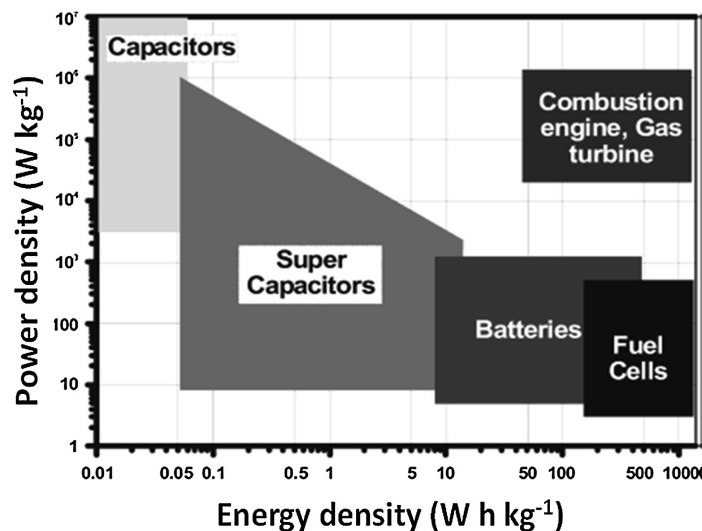


**Figure 1.2.** Ragone plot of different electrochemical energy conversion systems. Adapted from [13].

## 1.2. Nanostructured carbon spheres

Recently, nanostructured carbon materials have been considered as competitive candidates for highly efficient electrodes of energy storage devices [2,14–16]. They have higher surface energy compared with their macro scale counterparts, which means higher surface activity, and thus more electro-active sites in the nanostructured electrodes, leading to high-capacity utilization of the electrode materials. Furthermore, their intrinsic inner porous structures allow for effective electrolyte infiltration, and the reduced dimensions of particle size can shorten the transport and diffusion path lengths of electrolyte ions, facilitating fast kinetics and high charge−discharge rates. In addition, well-defined hierarchical structures can withstand strain/stress in the electrode matrix and provide stable tunnels for electron transportation, ensuring enhanced cycling capacity. The rational manipulation of the morphologies of nanostructured carbon electrodes seems to be very promising in further improvement of the

performances of electrodes, which may result in a novel class of highly efficient energy storage devices.

The creation of a spherical shape is preferable to the law of natural selection because objects in nature tend to approach minimum energy, while the sphere is one of the most perfect matter structures [17]. From an engineering viewpoint, the spherical particles offer a great number of advantages over than of other shapes because they have no sharp edges and so are less prone to damaging or breaking other materials during processing. In addition, the size and regular shape of spheres allow the efficient ordering of subjects in closely packed states, especially in the case that necks and pores are present. Finally, the spheres provide excellent fluidity [18,19]. In particular, compared with the other carbon-based materials, carbon spheres have captivated vast attention of researchers due to the combined advantages of carbon materials with colloidal spheres, which gives them several unique features such as regular geometry, high uniformity, good fluidity, superior packing, and controllable particle size distribution [16,20]. Despite the enormous achievements made in many fields, carbon spheres continue to emerge and fabricate from smart synthetic strategies. These intriguing advantages and promising prospects have stimulated worldwide research activities of carbon spheres, especially in energy-related applications. Therefore, the development and innovation of advanced carbon spheres materials with well-defined structural and surface properties play a decisive role in the energy field, which present a chance to improve the performance of energy storage devices with both high power and energy densities. In addition, from a fundamental and application point of view, the entire procedure should be low-cost, facile, convenient, and easy to scale up from its current laboratory scale to an industrial level. **Figure 1.3** shows the typical transmission electron microscopy images of spherical carbon materials with different particle sizes, pore sizes, and porous structures.
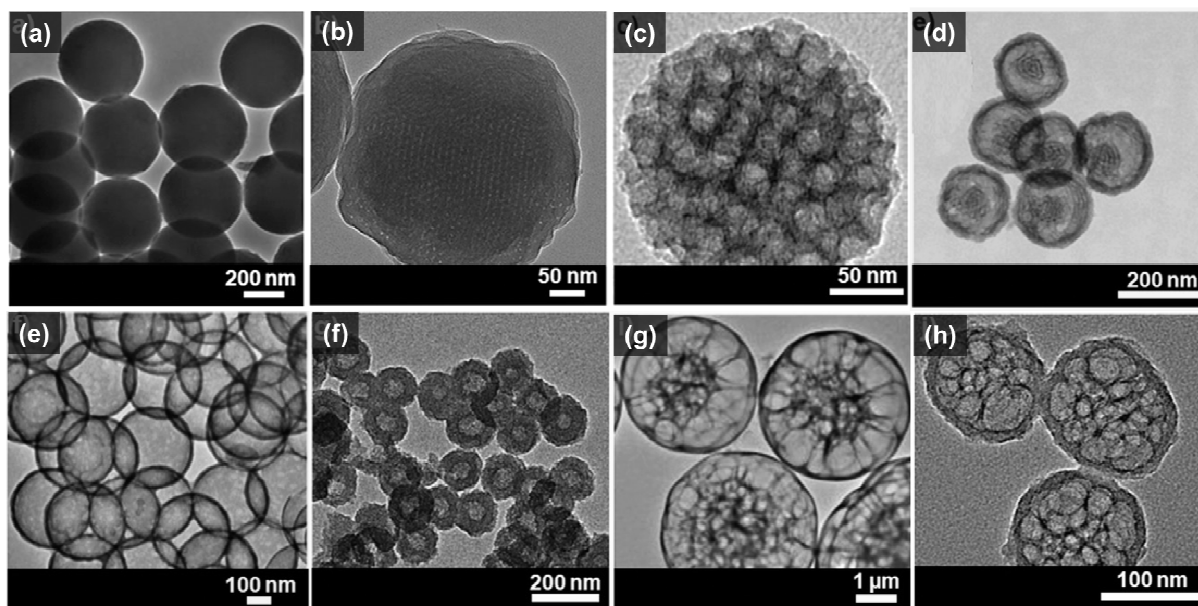
**Figure 1.3.** Typical transmission electron microscopy images of various carbon sphere nanoparticles fabricated by different methods. (a) Microporous carbon spheres, (b) Mesoporous carbon spheres, (c) N-doped mesoporous carbon nanospheres with large pores, (d) Yolk-shell carbon spheres, (e) Hollow carbon spheres, (f) Hollow carbon spheres with ultrahigh specific surface area, (g) Multichamber carbon microspheres, (h) Multiple-cavities carbon spheres. Adapted from [16].

## 1.3. Synthesis of carbon spheres

In recent years, the fabrication of carbon spheres with precisely tailored structures is an important research area and current hotspot in materials science. The various structures of carbon sphere materials benefit from numerous synthesis methods. According to whether the template is used and the type of template agents used, these synthesis methods are divided into three categories: hard template method (**Figure 1.4(a)**), soft template method (**Figure 1.4(b)**), and template-free method (**Figure 1.4(c-e)**).
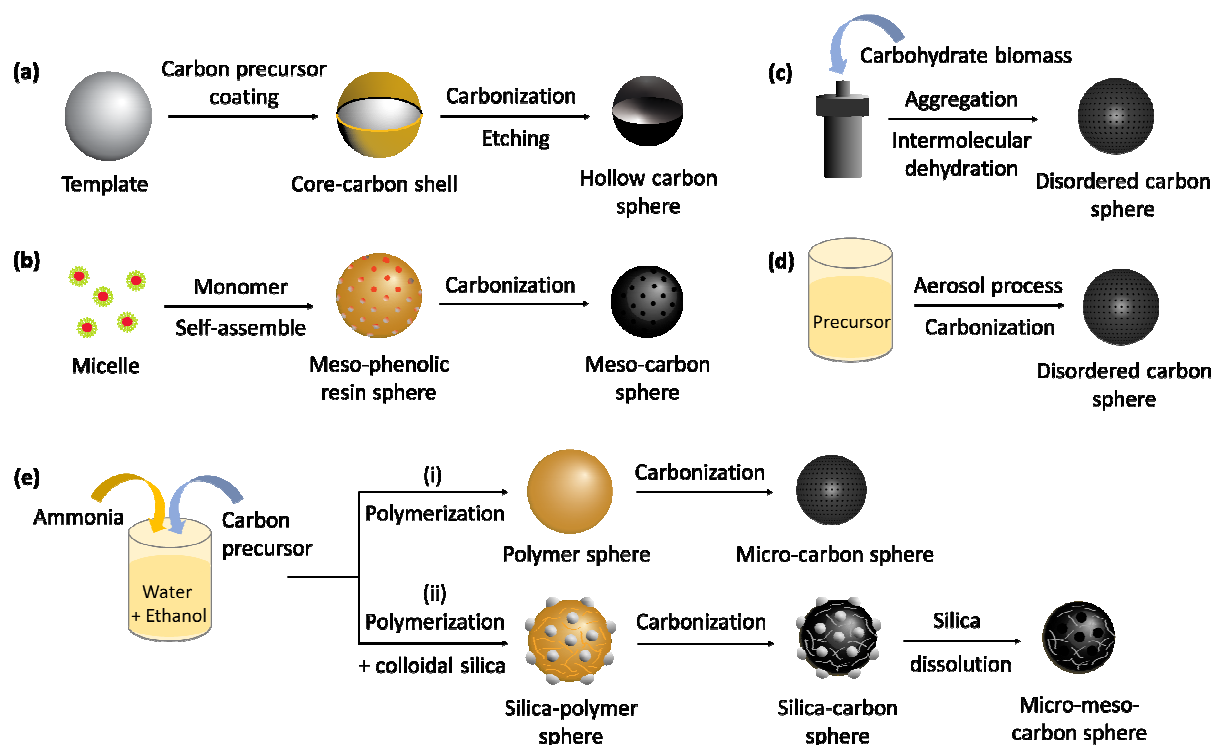
**Figure 1.4.** Primary methods for synthesizing carbon spheres. (a) Hard template method, (b) Soft template method, (c) Hydrothermal carbonization method, (d) Aerosol-assisted method, and (e) Extension of the Stöber method.

### 1.3.1. Hard template method

Hard templates are usually used materials with relatively rigid structures to guide the growth of materials by limiting space such as polymers including polystyrene (PS), resorcinol-formaldehyde (RF) polymer, poly(methyl methacrylate) (PMMA), and silica (SiO$_2$) [21,22]. The preparation of carbon spheres via a hard template approach involves four major steps: (i) the synthesis of sphere-shaped hard template materials, (ii) the preparation of the intermediate composite material containing both the carbon precursor and the hard template, (iii) the carbonization of the resulting composite material at high temperature in an inert gas atmosphere, and (iv) the removal of the hard template. To successfully incorporate the carbon precursor and hard template, the surface of the hard template usually needs to be modified to have the

appropriate surface charge and polarity features. To prepare the carbon spheres, a shell of the carbon precursor is deposited on the surface of the hard template through the traditional sol-gel or hydrothermal method. For the removal of the hard template, thermal decomposition or chemical etching methods are commonly used, depending on the nature of the hard templates. The as-obtained carbon spheres (*e.g.* porous or hollow carbon spheres) usually should be further treated to enhance certain properties, such as the degree of carbonization.

The typical hard templates and the common carbon precursors that are used for the fabrication of carbon spheres are summarized in **Table 1.1**. PS sphere templates can be easily removed by the thermal annealing procedure at a temperature of 400 ℃ [23]. White et al. reported the fabrication of hollow carbon spheres via PS spheres as hard templates [24]. RF colloid spheres, which can be synthesized by the Stöber method [25], also can be used as the hard templates to fabricate carbon spheres [26]. $SiO_2$ spheres have been commonly used as hard templates due to their easily tunable size, surface functionality, low cost, and high uniformity. $SiO_2$ solid spheres are usually synthesized through the Stöber method, where hydrolysis of the silica precursor takes place in a mixture of alcohol and water with ammonia as the catalyst [27]. Hollow carbon spheres can be achieved by coating different carbon precursors on the surface of $SiO_2$ particles by following the carbonization and etching process [28–31]. The hard template method for preparing hollow carbon spheres is usually easy to control and the obtained structure is often homogeneous and well-defined. Nevertheless, the major drawback of the hard template method is that it may involve a multi-step coating process and subsequent removal of the templates requires the use of dangerous chemicals (*e.g.* using an acid solution like HF or alkali solution like NaOH), which restricts its widespread application. In addition, the particle size, pore structure, and morphology of the obtained carbon spheres are predominantly dependent on the properties of the hard templates.

**Table 1.1.** Structures, templates, and precursors for carbon spheres obtained through the hard template method.

| Template | Carbon precursor | Structure | Reference |
|---|---|---|---|
| Latex nanoparticles | Glucose | Microporous | [24] |
| Latex nanoparticles | Glucose | Hierarchical micro and mesoporous | [32] |
| MCM-48 spheres | Glucose | Mesoporous | [33] |
| RF spheres | Phenolic resin | Hierarchical micro, meso, and macroporous | [26] |
| PMMA spheres | Phenolic resin | Mesoporous | [34] |
| $SiO_2$ spheres | Phenolic resin | Hierarchical micro and mesoporous | [35] |
| $SiO_2$ spheres | Dopamine | Mesoporous | [36,37] |
| $SiO_2$ spheres | Resorcinol and formaldehyde | Mesoporous | [38] |
| PMMA spheres | Resorcinol and formaldehyde | Microporous | [39] |
| $SiO_2$ spheres | Resorcinol and formaldehyde | Hierarchical micro, meso, and macroporous | [30] |
| $SiO_2$ spheres | Petroleum pitch | Mesoporous | [40] |
| $SiO_2$ spheres | Petroleum pitch | Hierarchical micro, meso, and macroporous | [41] |
| PS spheres | Aniline | Hierarchical micro and mesoporous | [42] |
| $SiO_2$ spheres | Aniline | Hierarchical micro, meso, and macroporous | [43] |
| $SiO_2$ spheres | Aniline | Mesoporous | [44] |
| $SiO_2$ spheres | Polyacrylonitrile | Mesoporous | [45] |
| $SiO_2$ spheres | Pyrrole | Micro and mesoporous | [46] |
| $SiO_2$ spheres | Polybenzoxazine | Mesoporous | [47] |
| MCM-48 spheres | Furfuryl alcohol | Mesoporous | [48] |
| $SiO_2$ opals | Resol | Mesoporous | [49] |

*1.3.2. Soft template method*

In contrast with the hard template method, soft templating synthesis does not need the preparation and removal of a template, which greatly reduces the reliance on the structure of the template, including size, shape, and physicochemical properties. There are four important requirements for successfully synthesizing porous carbon spheres materials through the soft template method [50]. Firstly, the soft template precursors should be able to assemble themselves into nanostructures. Secondly, the generation of intermediate composites with both the carbon precursor and the soft template is necessary. Thirdly, the soft templates should not only tolerate the temperature of carbon formation but also be easily decomposed during the subsequent carbonization process. Finally, the carbon precursors should become thermosetting before reaching the decomposition temperature of soft templates during the carbonization process.

Over the past decade, a significant process has been made in the direct synthesis of mesoporous carbon spheres from amphiphilic block copolymers (*e.g.* polystyrene-*block*-poly(ethylene oxide) (PS-*b*-PEO), PEO-*block*-poly(methyl methacrylate) (PEO-*b*-PMMA)), which follows the organic-organic self-assembly method using phenolic resin or its derivatives as the carbon precursor and amphiphilic surfactants as structure-directing agents. It was initiated by the pioneering works of Dai et al. [50,51], Nishiyama et al. [52], and Zhao et al [53,54]. However, considering that the carbon precursors are weakly self-assembled and that adjacent nanospheres are liable to crosslink during the hydrothermal carbonization process, the soft templating synthesis of monodisperse mesoporous carbon spheres is still a significant challenge. Until now, there are still only a few reports have been published about the successful fabrication of monodispersed mesoporous carbon spheres using the soft template method [55–59]. For example, self-polymerization of dopamine and spontaneous co-assembly of di-block copolymer micelles could assist the formation of mesopores. By using spray drying pyrolysis or spray drying followed by the carbonization process, monodispersed mesoporous carbon spheres could be fabricated on a large scale, but their particle size distribution was relatively broad and not uniform, ranging from several tens of nanometers to hundreds of nanometers [60,61]. Hollow mesoporous carbon spheres can also be achieved on the basis of a soft template strategy [62]. By taking Pluronic F127 as a soft template, Yang's group synthesized hollow mesoporous carbon spheres by the hydrothermal treatment of α-cyclodextrin, and the morphology as well as particle

size could also be controlled. The typical soft templates and the common carbon precursors that are used for the fabrication of mesoporous carbon spheres are summarized in **Table 1.2**.

Recently, it has been demonstrated that the self-assembly of tetraethyl orthosilicate (TEOS), phenolic resin (*e.g.* resorcinol/formaldehyde, 3-aminophenol/formaldehyde, *m*-phenylenediamine/formaldehyde), and cationic surfactant in water/ethanol in the presence of ammonia can lead to a series of porous carbon spheres [63–69]. For instance, Dai and co-workers developed a "silica-assisted" strategy for the synthesis of highly dispersed mesoporous carbon spheres, hollow mesoporous carbon spheres, and yolk-shell mesoporous carbon spheres through the co-assembly of resorcinol/formaldehyde and TEOS in the presence of hexadecyl trimethylammonium chloride as the soft template [63]. The particle size of the carbon spheres was controlled from 180 to 850 nm through variation of the water/ethanol volumetric ratio. This approach provides an efficient method to avoid severe aggregation of carbon spheres during the high-temperature carbonization process. Following this work, by tri-constituent co-assembly of 3-aminophenol, formaldehyde, and bis[3-(triethoxysilyl)propyl]tetrasulfide, N, S-doped carbon-silica nanospheres with either smooth or rough surface could be obtained by direct carbonization of the polymer-silica nanospheres [70].

Generally, the soft templating strategy is relatively simple and applicable for the fabrication of various carbon spheres. Compared with the hard template method, the soft template method always involves the co-assembly of the carbon precursors and soft templates for the formation of mesostructures without requiring the harsh conditions needed to remove the hard templates. Nevertheless, the high cost of soft templates, low yield of carbon spheres, limited types of usable soft templates, and difficulty in controlling the particle size distribution are the major challenges for the soft template method at the current stage. Therefore, it is highly desirable to further design and synthesize carbon spheres with lower cost, more uniform particle size, and suitability for large-scale production.

**Table 1.2.** Structures, templates, and precursors for carbon spheres obtained through the soft template method.

| Template | Carbon precursor | Structure | Reference |
|---|---|---|---|
| Pluronic F127 | Phenol-formaldehyde | Mesoporous | [55,60,61,71,72] |
| Pluronic F127 | Resorcinol-formaldehyde | Mesoporous | [56] |
| Pluronic F127 | α-cyclodextrin | Micro and mesoporous | [62] |
| Pluronic F127 | Dopamine | Micro and mesoporous | [58] |
| PS-*b*-PEO | Dopamine | Mesoporous | [57,59,73] |

*1.3.3. Template-free method*

From the above presentation, it is clear that the templating methods including hard templating and soft templating methods are very effective ways for the fabrication of carbon sphere materials. However, drawbacks related to high cost and tedious operational procedures have hindered mass production for large-scale applications. Ideally, template-free methods for the fabrication of carbon spheres with a wide scale of pore sizes would be preferred. In this part, three simpler and commonly used template-free synthetic strategies, including hydrothermal carbonization, extension of the Stöber method, and aerosol-assisted method will be investigated.

1.3.3.1. Hydrothermal carbonization

The hydrothermal carbonization method of carbohydrates and raw lignocellulosic biomass has been extensively explored for the preparation of carbon spheres at relatively low temperatures (160 – 220 °C) due to its simplicity, sustainability, low cost, and high efficiency [74]. There are four steps during the hydrothermal carbonization process, including dehydration, condensation, polymerization, and aromatization. It results in microporous carbon spheres with tunable particle size ranging from 200 nm to 5 μm and a range of different functionalities depending on the carbon precursors used, such as glucose [75–77], sucrose [78], fructose [79], xylose [80], cyclodextrin [81], starch [82], lignocellulose [83], and phytic acid [84]. Although

hydrothermal carbonization represents a feasible way of producing carbon spheres, its wider application is still limited due to difficulties in controlling the particle size and porosity, as well as problems associated with digesting real biomass. Nanoporous carbon spheres obtained by hydrothermal carbonization are usually microporous, an extension of this strategy for the preparation of carbon spheres with well-defined morphology and porosity (*e.g.* mesoporous carbon spheres) is still a significant challenge and thus further research in this direction is highly desirable.

### 1.3.3.2. Extension of the Stöber method

Nanostructured phenolic resins have attracted considerable attention due to the facile functionalities of their size and porosity [85]. A major breakthrough in the development of nanoporous carbon spheres was achieved in 2011 by extending the classical Stöber method [25,86]. It was recently realized that the sol-gel formation of $SiO_2$ spheres resembles the polymerization reaction between resorcinol or 3-aminophenol and formaldehyde under basic conditions to form RF or 3-aminophenol-formaldehyde (APF) resin polymer. The prepared RF or APF resin spheres can be easily converted into monodispersed and microporous carbon spheres through the carbonization process [25,87]. Recently, Zhou's group reported that the potassium salt of RF resin spheres was fabricated by the reaction of KOH and RF resin spheres and was carbonized into microporous carbon sphere materials [88]. It is found that the prepared carbon materials still maintain the monodisperse spherical shapes and possess highly developed ultra-microporosity with uniform pore size. In addition, various heteroatom-containing phenol derivatives (*e.g.* aminophenol, nitrophenol, and halide-substituted phenols) have been used to prepare phenolic resin spheres, which can be further converted to heteroatom-doped carbon spheres [89]. It has been found that 3-aminophenol and 4-amino-3-nitrophenol could be used to synthesize monodispersed carbon spheres with high nitrogen content ranging from 5.5 to 11.9 wt% in the carbon matrix. The inductive effect of the substitution group in phenol derivatives and the orientation effect of the aromatic ring toward electrophilic addition have played important roles in the successful formation of phenol resin spheres [89].

1.3.3.3. Aerosol-assisted method

Aerosol-assisted techniques, such as spray drying and spray pyrolysis, are simple, cost-effective, continuous, and scalable methods for preparing carbon spheres [90,91]. Owing to these advantages, they have been widely applied in the food, pharmaceutical, and chemical industries. For spray drying, the precursor solution or slurry is first atomized into fine droplets. The fine droplets are then carried by the carrier gas into the drying chamber, where the solvent evaporates and solid particles form. For spray pyrolysis, the operating temperature is substantially higher than that of spray drying, and thermal-induced chemical reactions may occur under such conditions.

Recently, a pomegranate-like carbon microsphere (PCS) built up with monodisperse, submicron carbon spheres are fabricated through a scalable spray drying-assisted method [92]. Firstly, monodisperse APF resin spheres can be obtained through the polymerization of 3-aminophenol and formaldehyde in deionized water without any catalyst. Secondly, during spray drying process, the monodisperse resin colloids are assembled into pomegranate-like resin microspheres. Finally, the pomegranate-like resin microspheres are converted into PCS after carbonization and KOH activation. The obtained PCS is composed of well-defined microspheres with a relatively broad size distribution ranging from 1 to 5 μm. Until now, considering the sustainable development of carbon sphere materials, using biomass has received increasing attention due to its renewability, reproducibility, readily availability, cost-effective, and environmentally benign [93,94]. Although biomass has been used as a raw material for the preparation of carbon materials, there have been few reports of the successful production of carbon spheres from biomass-based materials using spray drying [95,96]. Therefore, template-free spray drying is able to produce carbon spheres by simply using the appropriate precursors, and so provides a very simple and convenient method for obtaining these materials that also avoids the introduction of impurities.

Suslick's group developed a general ultrasonic spray pyrolysis method for the preparation of porous carbon spheres [97–100]. A wide variety of carbon-containing compounds, such as alkali halocarboxylate (chloroacetate and dichloroacetate), alkali propiolates, substituted benzoates, and carbohydrates, were employed as the precursors in the aerosol-assisted synthesis.

Interestingly, the micro-structure of the obtained porous carbon spheres is highly dependent on the choice of precursor. Through tuning the precursor and concentration, a variety of porous carbon spheres can be produced, including micro-/meso-/macroporous carbon spheres, hollow carbon spheres, double-shelled hollow carbon spheres, Janus carbon spheres, and jellyfish-like carbon spheres.

## 1.4. Application of carbon spheres

Energy storage has become a highly important challenge due to the increased development and use of portable electronics and electric and hybrid vehicles that require high power and energy densities. Two of the most viable current options for electrical energy storage are rechargeable batteries and supercapacitors [2,3]. These devices are mainly composed of anode, cathode, separator, and electrolyte, and their improvement is highly dependent on advances achieved in electrode materials, especially in carbon materials, which play an important role as electrodes in this technology.

Most applications of carbon spheres are mainly in relation to energy storage devices. This is because the performance of carbon spheres can be easily controlled by some parameters, including specific surface area, pore texture, and surface chemistry. In addition, the advantages of using carbon spheres rather than carbon materials with the other shapes in these applications are due to (i) their tunable sphere diameter and morphology (dense, hollow, and core−shell), (ii) their tunable specific surface area and porosity, in which guest species can be introduced, (iii) the ease of their doping with other heteroatoms, (iv) their high packing density and enhanced mass transport, and (v) their robust and structural stability.

### 1.4.1. LIBs

Porous carbon spheres can perform better than graphite as anode material, having a higher theoretical capacity ($400 - 700$ mAh g$^{-1}$), because Li can intercalate within graphite crystallites and micropores. These porous carbon spheres have been successfully designed and

synthesized with sizes from nanometers to micrometers, which have different pore structures, ranging from micropore (< 2 nm), mesopores (2 – 50 nm) to macropores (> 50 nm) to satisfy the requirement of LIBs [101]. According to the structure-property relationship, good conductivity, suitable surface chemistry, large specific surface area, and pore volume are critical to obtain a high Li storage capacity and stability, when employing carbon spheres as the anode material for LIBs. Specifically, good conductivity ensures efficient electron transport, while high specific surface area allows for good contact with the electrolyte to sustain high Li-ion flux through the interface, and large pore volume makes it possible to accommodate Li and the volume changes during lithiation. Furthermore, a hierarchy of pores is desired, as micropores promote reversible intercalation/de-intercalation of $Li^+$ to afford a high storage capacity, while meso/macropores favor $Li^+$ transfer kinetics and electrolyte mobility [101,102].

Potentially, doping of single or dual heteroatoms (*e.g.* B, N, O, P, S) into carbon, the electronic and chemical structure can be modulated, leading to potentially enhanced electronic conductivity, enlarged interlayer distance, $Li^+$/electrolyte absorbability, and more active sites for the improvements in Li storage and cycling performance [103–105]. N atoms with a higher electronegativity and similar atomic diameter to C are most widely used, which can donate free electrons to the π system of carbon to improve the electrical conductivity [106] and introduce active sites to enhance the electrochemical reactivity for higher Li-ion storage [107].

In addition, the loading of silicon [108] and transition metal oxides [2] is a feasible strategy to further increase the electrochemical performance of porous carbon anodes. Thus, the Li-Si system has the possibility of achieving capacity of up to 4200 mAh $g^{-1}$ through the formation of Li-Si alloys. Magnetite has also attracted attention as anode material for LIBs due to its higher specific capacitance (928 mAh $g^{-1}$) *versus* graphite (372 mAh $g^{-1}$) and its low cost, abundance, non-toxicity [109]. However, these anodes have poor cyclability due to agglomeration and volume expansion/shrinkage during lithiation/delithiation. Therefore, loading in carbon spheres represents an attempt to overcome these shortcomings. The high-capacity carbon-based anode materials (*e.g.* Si/C, $SiO_x$/C, carbon/sulfur) have been extensively investigated, which aims to attain the high energy density target. Despite the many advantages of this technique, it is worth noting that the potential pore blockage by loading other materials can

be detrimental. Therefore, the rational structure design is essential. The structure, synthesis method, and electrochemical performance of porous carbon sphere materials and active materials/porous carbon sphere composites as electrode materials in LIBs are summarized in **Table 1.3**.

**Table 1.3.** Structure, synthesis method, and electrochemical performance of porous carbon sphere materials and active materials/porous carbon sphere composites as electrode materials in LIBs.

| Electrode materials | Synthesis method | Current density (mA g$^{-1}$) | Highest reversible capacity (mAh g$^{-1}$) | Reference |
|---|---|---|---|---|
| N-doped mesoporous carbon hollow spheres | Hard templating | 500 | 1709 | [103] |
| Macro-mesoporous hollow carbon spheres | Hard templating | 500 | 646 | [110] |
| Hierarchical macro-, meso- and microporous carbon | Template-free | 100 | 2811 | [111] |
| Porous turbostratic carbon spheres | Template-free spray pyrolysis | 37.2 | 378 | [112] |
| N-doped hollow carbon nanospheres | Pyrolysis | 100 | 2053 | [104] |
| N-doped carbon spheres | Surfactant-assisted hydrothermal method | 20 | 580 | [77] |
| Porous carbon spheres doped with Fe$_3$C | Hydrothermal | 100 | 756.8 | [113] |
| Hollow porous carbon spheres | Microwave-assisted technique | 100 | 1750 | [114] |
| SnO$_2$/carbon hollow spheres | Hard templating | 100 | 2157 | [115] |
| MoO$_2$/C microspheres | Hard templating | 100 | 768 | [116] |
| MoS$_2$@hollow carbon spheres | Hard templating and carbonization | 1000 | 822.7 | [117] |

| Fe$_3$O$_4$/mesoporous carbon spheres | Hydrothermal and carbonization | 500 | 1214.3 | [118] |
|---|---|---|---|---|
| SiO$_x$@carbon nanocomposite spheres | Stöber strategy | 50 | 1144 | [119] |
| SnO$_2$@C yolk-shell nanospheres | Stöber sol-gel coating | 100 | 2190 | [120] |

*1.4.2. Supercapacitors*

Typically, porous carbon spheres have been employed as the electrode materials for commercial EDLC devices [3,11]. The spherical structure can decrease the transmission distance of electrolyte ions, so that the electric double-layer can be easily formed between the electrolyte and electrode [121]. The capacitance of EDLCs is directly linked with the contact area of the electrode with electrolyte. In principle, elevating specific surface area, pore volume, and electrical conductivity of a porous carbon sphere electrode can effectively enhance charge accumulation in electrical double layer formation to achieve a larger EDLC capacitance [122,123]. It is generally considered that the existence of micropores in carbon materials can significantly increase the specific surface area, which plays a key role in enhancing specific capacitance. However, some studies found that ultrahigh specific surface area may lead to decreased volumetric capacitance due to a relatively lower packing density [124]. On account of this, rational control over the pore sizes to maximize ion accessible specific surface area and decrease the dead volume is of a great account [125]. Both experimental [126] and theoretical studies [127] have manifested that the maximum capacitance can be acquired when carbon pore size (mainly micropores) is well matched to the ion size of the liquid electrolyte, which is favorable to charge accommodation. However, restricted by the slow ion diffusion and desolvation in these sub-nanometer micropores, a high capacitance can only be achieved at a low or moderate charge−discharge rate, which limits the rate capability and power density performance [10]. This issue can be resolved by introducing meso-/macropores in microporous carbon structure as the mesopores can serve as reservoirs to shorten the transport pathway and boost efficient ion diffusion, allowing for high capacitance retention during the fast charging/discharging process [128]. To obtain these goals, the rational combination of micro,

meso, and macropores in a porous carbon sphere electrode is pivotal to achieve high specific capacitance and rate performance.

The introduction of heteroatom (*e.g.* N, S, B, O, P) into porous carbon spheres also plays a vital role in the EDLC properties [58,65,129,130]. Take the most extensively used N-doping as an example, it improves not only the electrical conductivity but also the electrolyte wettability. In addition, it also provides extra active sites for reversible redox reactions, contributing to the overall capacitance of the sample [131]. **Table 1.4** summarizes the supercapacitor performance of typical porous carbon spheres prepared by various synthetic methods.

**Table 1.4.** The electrochemical performance of porous carbon spheres with different structures in EDLCs.

| Electrode material | Synthesis method | Current density (A g$^{-1}$) | Capacitance (F g$^{-1}$) | Reference |
|---|---|---|---|---|
| Mesoporous hollow carbon spheres | Hard templating | 0.3 | 162 | [132] |
| N, O-doped double-shell hollow carbon spheres | Hard templating | 1 | 320 | [129] |
| N-doped mesoporous hollow carbon spheres | Soft templating | 1 | 240 | [65] |
| Yolk-shell porous carbon spheres | Soft templating | 0.1 | 268 | [68] |
| Interconnected hollow carbon spheres | Soft templating | 1 | 208 | [67] |
| Hollow carbon nanospheres | Template-free | 1 | 180 | [133] |
| Mesoporous hollow carbon spheres | Modified Stöber method | 1 | 310 | [134] |
| Double-shelled hollow carbon spheres | Modified Stöber method | 1 | 381 | [135] |
| N-doped porous carbon spheres | Modified Stöber method | 0.5 | 433 | [58] |

| | | | | |
|---|---|---|---|---|
| Hierarchically porous carbon spheres | Hydrothermal carbonization | 0.5 | 248 | [82] |
| S-doped porous carbon spheres | Hydrothermal carbonization | 0.5 | 405 | [130] |
| Porous carbon spheres | Soft templating and hydrothermal carbonization | 1 | 350 | [136] |
| Porous hollow carbon spheres | Hard templating and hydrothermal carbonization | 0.5 | 270 | [137] |
| Activated carbon spheres | Hydrothermal carbonization and chemical activation | 1 | 238 | [80] |
| Pomegranate-like carbon microspheres | Spray drying-assisted method | 1 | 338 | [92] |
| Hollow carbon spheres | Spray pyrolysis-assisted method | 0.1 | 112 | [138] |

## 1.5. Objectives and outline of dissertation

This dissertation is intended to address the following objectives: (i) to develop the methodologies for design and synthesis of spherical carbon-based materials using soft template and template-free spray drying method, particularly the precisely tailored structure, pore texture, and surface properties, (ii) to provide a possible mechanism for obtaining an in-depth understanding of the particle formation of carbon-based materials, and (iii) to show how the morphology, pore size, and material composition may influence LIBs and supercapacitors performance. This dissertation comprises five chapters, of which content is described briefly as follows.

**Chapter 1** summarizes the important properties of spherical carbon-based materials, the several synthetic strategies for producing spherical carbon materials with desirable structures and functionalities for energy storage applications, and the alternative material in response to the problem suffered by carbonaceous materials. This summary and problem statements lead to the motivation of the researches covered within the scope of this dissertation.

**Chapter 2** discusses the developed strategy for fabrication of carbon-coated $SiO_x$ ($SiO_x@C$ core−shell) particles through a sol-gel method using the simultaneous hydrolysis-

condensation of tetramethyl orthosilicate (TMOS) and polymerization of 3-aminophenol and formaldehyde followed by the carbonization process. The core−shell particles can be obtained with a well-controlled reaction rate and spherical morphology by using TMOS as an excellent silica precursor for the first time instead of the traditionally used tetraethyl orthosilicate (TEOS). When used as the anode material for LIBs, the obtained $SiO_x@C$ core−shell particles exhibited a reversible capacity of 509.2 mAh $g^{-1}$ at 100 mA $g^{-1}$ and the capacity retention was approximately 80% after 100 cycles. The significantly improved electrochemical performance due to the morphology and structure of the material.

**Chapter 3** focuses on the synthesis of spherical carbon particles derived from Kraft lignin via the spray drying method followed by the carbonization process. The developed synthetic strategy is highly significant because it allows the utilization of lignin as an abundant and sustainable carbon precursor. The carbon particles generated in this study could be obtained with spherical morphologies and it could be precisely controlled from dense to hollow sphere by varying the KOH concentration. In addition, to get a better understanding of the particle formation of carbon particles, a plausible mechanism has been discussed in detail, which provides insights with regard to the exploration of lignin-derived carbon materials. The specific surface area and tap density of spherical carbon particles having a dense structure were determined to be 1233 $m^2$ $g^{-1}$ and 1.46 g $cm^{-3}$, respectively, both of which are significantly higher than values reported for irregularly shaped carbon particles.

**Chapter 4** provides the characterization of hollow carbon spheres (HCSs) derived from Kraft lignin with their structural, pore texture, surface morphology, and electrochemical performance for supercapacitors. HCSs with high specific surface area up to 2424.8 $m^2$ $g^{-1}$ and micro-mesoporous structure were obtained at low KOH-to-lignin mass ratios (below 1.5), which was in accordance with green chemistry principles. In addition, these HCSs can be used as electrode materials in supercapacitors for energy storage applications. This newly developed synthetic process is expected to lead an advanced carbon material and the value-added utilization of Kraft lignin.

**Chapter 5** provides a summary of all chapters and suggestions for future research.

**1.6. References**

[1]     S. Chu, A. Majumdar, Opportunities and challenges for a sustainable energy future, Nature 488 (2012) 294–303.

[2]     W. Long, B. Fang, A. Ignaszak, Z. Wu, Y.J. Wang, D. Wilkinson, Biomass-derived nanostructured carbons and their composites as anode materials for lithium ion batteries, Chem. Soc. Rev. 46 (2017) 7176–7190.

[3]     M. Zhang, L. He, T. Shi, R. Zha, Nanocasting and direct synthesis strategies for mesoporous carbons as supercapacitor electrodes, Chem. Mater. 30 (2018) 7391–7412.

[4]     J.B. Goodenough, Y. Kim, Challenges for rechargeable Li batteries, Chem. Mater. 22 (2010) 587–603.

[5]     J.-M.Tarascon, M. Armand, Issues and challenges facing rechargeable lithium batteries, Nature 414 (2001) 359–367.

[6]     Z.A. Ghazi, Z. Sun, C. Sun, F. Qi, B. An, F. Li, H.M. Cheng, Key aspects of lithium metal anodes for lithium metal batteries, Small 15 (2019) 1900687.

[7]     H. Ye, S. Xin, Y.X. Yin, Y.G. Guo, Advanced porous carbon materials for high-efficient lithium metal anodes, Adv. Energy Mater. 7 (2017) 1700530.

[8]     S. Zhang, K. Zhao, T. Zhu, J. Li, Electrochemomechanical degradation of high-capacity battery electrode materials, Prog. Mater. Sci. 89 (2017) 479–521.

[9]     Poonam, K. Sharma, A. Arora, S.K. Tripathi, Review of supercapacitors: Materials and devices, J. Energy Storage 21 (2019) 801–825.

[10]    P. Simon, Y. Gogotsi, Materials for electrochemical capacitors, Nat. Mater. 7 (2008) 845–854.

[11]    Z. Bi, Q. Kong, Y. Cao, G. Sun, F. Su, X. Wei, X. Li, A. Ahmad, L. Xie, C.M. Chen, Biomass-derived porous carbon materials with different dimensions for supercapacitor electrodes: A review, J. Mater. Chem. A 7 (2019) 16028–16045.

[12]   M. Vangari, T. Pryor, L. Jiang, Supercapacitors: Review of materials and fabrication methods, J. Energy Eng. 139 (2013) 72–79.

[13]   M. Winter, R.J. Brodd, What are batteries, fuel cells, and supercapacitors?, Chem. Rev. 104 (2004) 4245–4269.

[14]   Z. Yang, J. Ren, Z. Zhang, X. Chen, G. Guan, L. Qiu, Y. Zhang, H. Peng, Recent advancement of nanostructured carbon for energy applications, Chem. Rev. 115 (2015) 5159–5223.

[15]   S. Schrettl, B. Schulte, H. Frauenrath, Templating for hierarchical structure control in carbon materials, Nanoscale 8 (2016) 18828–18848.

[16]   H. Tian, J. Liang, J. Liu, Nanoengineering carbon spheres as nanoreactors for sustainable energy applications, Adv. Mater. 31 (2019) 1903886.

[17]   P. Qiu, B. Ma, C. Te Hung, W. Li, D. Zhao, Spherical mesoporous materials from single to multilevel architectures, Acc. Chem. Res. 52 (2019) 2928–2938.

[18]   T. Ogi, A.B.D. Nandiyanto, W.N. Wang, F. Iskandar, K. Okuyama, Direct synthesis of spherical YAG:Ce phosphor from precursor solution containing polymer and urea, Chem. Eng. J. 210 (2012) 461–466.

[19]   M. Österberg, M.H. Sipponen, B.D. Mattos, O.J. Rojas, Spherical lignin particles: A review on their sustainability and applications, Green Chem. 22 (2020) 2712–2733.

[20]   J. Liu, N.P. Wickramaratne, S.Z. Qiao, M. Jaroniec, Molecular-based design and emerging applications of nanoporous carbon spheres, Nat. Mater. 14 (2015) 763–774.

[21]   W. Li, J. Liu, D. Zhao, Mesoporous materials for energy conversion and storage devices, Nat. Rev. Mater. 1 (2016) 16023.

[22]   S. Li, A. Pasc, V. Fierro, A. Celzard, Hollow carbon spheres, synthesis and applications–a review, J. Mater. Chem. A 4 (2016) 12686–12713.

[23]   A.F. Arif, Y. Kobayashi, R. Balgis, T. Ogi, H. Iwasaki, K. Okuyama, Rapid microwave-

assisted synthesis of nitrogen-functionalized hollow carbon spheres with high monodispersity, Carbon 107 (2016) 11–19.

[24]    R.J. White, K. Tauer, M. Antonietti, M.M. Titirici, Functional hollow carbon nanospheres by latex templating, J. Am. Chem. Soc. 132 (2010) 17360–17363.

[25]    J. Liu, S.Z. Qiao, H. Liu, J. Chen, A. Orpe, D. Zhao, G.Q. Lu, Extension of the Stöber method to the preparation of monodisperse resorcinol-formaldehyde resin polymer and carbon spheres, Angew. Chemie - Int. Ed. 50 (2011) 5947–5951.

[26]    T. Yang, R. Zhou, D.W. Wang, S.P. Jiang, Y. Yamauchi, S.Z. Qiao, M.J. Monteiro, J. Liu, Hierarchical mesoporous yolk-shell structured carbonaceous nanospheres for high performance electrochemical capacitive energy storage, Chem. Commun. 51 (2015) 2518–2521.

[27]    W. Stöber, A. Fink, Controlled growth of monodisperse silica spheres in the micron size range, J. Colloid Interface Sci. 26 (1968) 62–69.

[28]    R. Liu, S.M. Mahurin, C. Li, R.R. Unocic, J.C. Idrobo, H. Gao, S.J. Pennycook, S. Dai, Dopamine as a carbon source: The controlled synthesis of hollow carbon spheres and yolk-structured carbon nanocomposites, Angew. Chemie - Int. Ed. 50 (2011) 6799–6802.

[29]    A. Chen, Y. Yu, H. Lv, Y. Wang, S. Shen, Y. Hu, B. Li, Y. Zhang, J. Zhang, Thin-walled, mesoporous and nitrogen-doped hollow carbon spheres using ionic liquids as precursors, J. Mater. Chem. A 1 (2013) 1045–1047.

[30]    S. Feng, W. Li, Q. Shi, Y. Li, J. Chen, Y. Ling, A.M. Asiri, D. Zhao, Synthesis of nitrogen-doped hollow carbon nanospheres for $CO_2$ capture, Chem. Commun. 50 (2014) 329–331.

[31]    J. Song, C. Zhang, X. Guo, J. Zhang, L. Luo, H. Liu, F. Wang, G. Wang, Entrapping polysulfides by using ultrathin hollow carbon sphere-functionalized separators in high-rate lithium-sulfur batteries, J. Mater. Chem. A 6 (2018) 16610–16616.

[32]    K. Tang, L. Fu, R.J. White, L. Yu, M.M. Titirici, M. Antonietti, J. Maier, Hollow carbon

nanospheres with superior rate capability for sodium-based batteries, Adv. Energy Mater. 2 (2012) 873–877.

[33]  J. Gu, S. Su, Y. Li, Q. He, J. Shi, Hydrophilic mesoporous carbon nanoparticles as carriers for sustained release of hydrophobic anti-cancer drugs, Chem. Commun. 47 (2011) 2101–2103.

[34]  Z. Wang, F. Li, A. Stein, Direct synthesis of shaped carbon nanoparticles with ordered cubic mesostructure, Nano Lett. 7 (2007) 3223–3226.

[35]  K. Zhang, Q. Zhao, Z. Tao, J. Chen, Composite of sulfur impregnated in porous hollow carbon spheres as the cathode of Li-S batteries with high performance, Nano Res. 6 (2013) 38–46.

[36]  Z. Zhang, G. Wang, Y. Lai, J. Li, Z. Zhang, W. Chen, Nitrogen-doped porous hollow carbon sphere-decorated separators for advanced lithium-sulfur batteries, J. Power Sources 300 (2015) 157–163.

[37]  V. Duraisamy, R. Krishnan, S.M. Senthil Kumar, N-doped hollow mesoporous carbon nanospheres for oxygen reduction reaction in alkaline media, ACS Appl. Nano Mater. 3 (2020) 8875–8887.

[38]  J. Zang, T. An, Y. Dong, X. Fang, M. Zheng, Q. Dong, N. Zheng, Hollow-in-hollow carbon spheres with hollow foam-like cores for lithium–sulfur batteries, Nano Res. 8 (2015) 2663–2675.

[39]  J. Ye, J. Zang, Z. Tian, M. Zheng, Q. Dong, Sulfur and nitrogen co-doped hollow carbon spheres for sodium-ion batteries with superior cyclic and rate performance, J. Mater. Chem. A 4 (2016) 13223–13227.

[40]  N. Jayaprakash, J. Shen, S.S. Moganty, A. Corona, L.A. Archer, Porous hollow carbon@sulfur composites for high-power lithium-sulfur batteries, Angew. Chemie - Int. Ed. 50 (2011) 5904–5908.

[41]  Q. Ma, L. Wang, W. Xia, D. Jia, Z. Zhao, Nitrogen-doped hollow amorphous carbon

spheres@graphitic shells derived from pitch: New structure leads to robust lithium storage, Chem. - A Eur. J. 22 (2016) 2339–2344.

[42]    J. Zhu, H. Zhou, C. Zhang, J. Zhang, S. Mu, Dual active nitrogen doped hierarchical porous hollow carbon nanospheres as an oxygen reduction electrocatalyst for zinc-air batteries, Nanoscale 9 (2017) 13257–13263.

[43]    Z. Lei, Z. Chen, X.S. Zhao, Growth of polyaniline on hollow carbon spheres for enhancing electrocapacitance, J. Phys. Chem. C 114 (2010) 19867–19874.

[44]    Z. Lei, M. Zhao, L. Dang, L. An, M. Lu, A.Y. Lo, N. Yu, S. Bin Liu, Structural evolution and electrocatalytic application of nitrogen-doped carbon shells synthesized by pyrolysis of near-monodisperse polyaniline nanospheres, J. Mater. Chem. 19 (2009) 5985–5995.

[45]    A. Chen, K. Xia, L. Zhang, Y. Yu, Y. Li, H. Sun, Y. Wang, Y. Li, S. Li, Fabrication of nitrogen-doped hollow mesoporous spherical carbon capsules for supercapacitors, Langmuir 32 (2016) 8934–8941.

[46]    D. Li, H. Chen, G. Liu, M. Wei, L.X. Ding, S. Wang, H. Wang, Porous nitrogen doped carbon sphere as high performance anode of sodium-ion battery, Carbon 94 (2015) 888–894.

[47]    F. Pei, T.H. An, J. Zang, X.J. Zhao, X.L. Fang, M.S. Zheng, Q.F. Dong, N.F. Zheng, From hollow carbon spheres to N-doped hollow porous carbon bowls: Rational design of hollow carbon host for Li-S batteries, Adv. Energy Mater. 6 (2016) 1502539.

[48]    T.W. Kim, P.W. Chung, I.I. Slowing, M. Tsunoda, E.S. Yeung, V.S.Y. Lin, Structurally ordered mesoporous carbon nanoparticles as transmembrane delivery vehicle in human cancer cells, Nano Lett. 8 (2008) 3724–3727.

[49]    Z. Sun, Y. Liu, B. Li, J. Wei, M. Wang, Q. Yue, Y. Deng, S. Kaliaguine, D. Zhao, General synthesis of discrete mesoporous carbon microspheres through a confined self-assembly process in inverse opals, ACS Nano 7 (2013) 8706–8714.

[50]    C. Liang, Z. Li, S. Dai, Mesoporous carbon materials: Synthesis and modification, Angew.

Chemie - Int. Ed. 47 (2008) 3696–3717.

[51] C. Liang, K. Hong, G.A. Guiochon, J.W. Mays, S. Dai, Synthesis of a large-scale highly ordered porous carbon film by self-assembly of block copolymers, Angew. Chemie - Int. Ed. 43 (2004) 5785–5789.

[52] S. Tanaka, N. Nishiyama, Y. Egashira, K. Ueyama, Synthesis of ordered mesoporous carbons with channel structure from an organic-organic nanocomposite, Chem. Commun. (2005) 2125–2127.

[53] Y. Meng, D. Gu, F. Zhang, Y. Shi, H. Yang, Z. Li, C. Yu, B. Tu, D. Zhao, Ordered mesoporous polymers and homologous carbon frameworks: Amphiphilic surfactant templating and direct transformation, Angew. Chemie - Int. Ed. 44 (2005) 7053–7059.

[54] Y. Wan, Y. Shi, D. Zhao, Supramolecular aggregates as templates: Ordered mesoporous polymers and carbons, Chem. Mater. 20 (2008) 932–945.

[55] Y. Fang, D. Gu, Y. Zou, Z. Wu, F. Li, R. Che, Y. Deng, B. Tu, D. Zhao, A low-concentration hydrothermal synthesis of biocompatible ordered mesoporous carbon nanospheres with tunable and uniform size, Angew. Chemie - Int. Ed. 49 (2010) 7987–7991.

[56] J. Liu, T. Yang, D.W. Wang, G.Q. Lu, D. Zhao, S.Z. Qiao, A facile soft-template synthesis of mesoporous polymeric and carbonaceous nanospheres, Nat. Commun. 4 (2013) 2798.

[57] J. Tang, J. Liu, C. Li, Y. Li, M.O. Tade, S. Dai, Y. Yamauchi, Synthesis of nitrogen-doped mesoporous carbon spheres with extra-largepores through assembly of diblock copolymer micelles, Angew. Chemie - Int. Ed. 54 (2015) 588–593.

[58] S. Xiong, J. Fan, Y. Wang, J. Zhu, J. Yu, Z. Hu, A facile template approach to nitrogen-doped hierarchical porous carbon nanospheres from polydopamine for high-performance supercapacitors, J. Mater. Chem. A 5 (2017) 18242–18252.

[59] H.F. Fei, Y. Long, H.J. Yu, B.M. Yavitt, W. Fan, A. Ribbe, J.J. Watkins, Bimodal

mesoporous carbon spheres with small and ultra-large pores fabricated using amphiphilic brush block copolymer micelle templates, ACS Appl. Mater. Interfaces 12 (2020) 57322–57329.

[60]   Y. Yan, F. Zhang, Y. Meng, B. Tu, D. Zhao, One-step synthesis of ordered mesoporous carbonaceous spheres by an aerosol-assisted self-assembly, Chem. Commun. 1 (2007) 2867–2869.

[61]   Z. Wu, W.D. Wu, W. Liu, C. Selomulya, X.D. Chen, D. Zhao, A general "surface-locking" approach toward fast assembly and processing of large-sized, ordered, mesoporous carbon microspheres, Angew. Chemie - Int. Ed. 52 (2013) 13764–13768.

[62]   Z.C. Yang, Y. Zhang, J.H. Kong, S.Y. Wong, X. Li, J. Wang, Hollow carbon nanoparticles of tunable size and wall thickness by hydrothermal treatment of α-cyclodextrin templated by F127 block copolymers, Chem. Mater. 25 (2013) 704–710.

[63]   Z.A. Qiao, B. Guo, A.J. Binder, J. Chen, G.M. Veith, S. Dai, Controlled synthesis of mesoporous carbon nanostructures via a "silica-assisted" strategy, Nano Lett. 13 (2013) 207–212.

[64]   J. Hou, T. Cao, F. Idrees, C. Cao, A co-sol-emulsion-gel synthesis of tunable and uniform hollow carbon nanospheres with interconnected mesoporous shells, Nanoscale 8 (2016) 451–457.

[65]   C. Liu, J. Wang, J. Li, M. Zeng, R. Luo, J. Shen, X. Sun, W. Han, L. Wang, Synthesis of N-doped hollow-structured mesoporous carbon nanospheres for high-performance supercapacitors, ACS Appl. Mater. Interfaces 8 (2016) 7194–7204.

[66]   J. Qi, Y. Li, G. Wei, J. Li, X. Sun, J. Shen, W. Han, L. Wang, Nitrogen doped porous hollow carbon spheres for enhanced benzene removal, Sep. Purif. Technol. 188 (2017) 112–118.

[67]   J. Cheng, X. Zhang, X. Miao, C. Chen, Y. Liu, Y. Chen, J. Lin, S. Chen, W. Wang, Y. Zhang, Interconnected hollow carbon spheres with tunable wall-thickness for improving the high-rate performance of energy storage devices, Electrochim. Acta 312 (2019) 358–

368.

[68] X. Wei, X. Li, C. Lv, X. Mo, K. Li, Hierarchically yolk-shell porous carbon sphere as an electrode material for high-performance capacitive deionization, Electrochim. Acta 354 (2020) 136590.

[69] J. Du, Y. Zhang, H. Wu, S. Hou, A. Chen, N-doped hollow mesoporous carbon spheres by improved dissolution-capture for supercapacitor, Carbon 156 (2020) 523–528.

[70] H. Tian, M. Saunders, A. Dodd, K. O'Donnell, M. Jaroniec, S. Liu, J. Liu, Triconstituent co-assembly synthesis of N,S-doped carbon-silica nanospheres with smooth and rough surfaces, J. Mater. Chem. A 4 (2016) 3721–3727.

[71] C. Chen, Y. Yu, C. He, L. Wang, H. Huang, R. Albilali, J. Cheng, Z. Hao, Efficient capture of $CO_2$ over ordered micro-mesoporous hybrid carbon nanosphere, Appl. Surf. Sci. 439 (2018) 113–121.

[72] Z. Jiang, X. Xi, S. Qiu, D. Wu, W. Tang, X. Guo, Y. Su, R. Liu, Ordered mesoporous carbon sphere-based solid-contact ion-selective electrodes, J. Mater. Sci. 54 (2019) 13674–13684.

[73] J. Tang, J. Wang, L.K. Shrestha, M.S.A. Hossain, Z.A. Alothman, Y. Yamauchi, K. Ariga, Activated porous carbon spheres with customized mesopores through assembly of diblock copolymers for electrochemical capacitor, ACS Appl. Mater. Interfaces 9 (2017) 18986–18993.

[74] B. Hu, K. Wang, L. Wu, S.H. Yu, M. Antonietti, M.M. Titirici, Engineering carbon materials from the hydrothermal carbonization process of biomass, Adv. Mater. 22 (2010) 813–828.

[75] M. Inada, N. Enomoto, J. Hojo, K. Hayashi, Structural analysis and capacitive properties of carbon spheres prepared by hydrothermal carbonization, Adv. Powder Technol. 28 (2017) 884–889.

[76] K. Xiang, S. Cai, X. Wang, M. Chen, S. Jiang, Nitrogen-doped activated microporous

carbon spheres as a sulfur matrix for advanced lithium-sulfur batteries, J. Alloys Compd. 740 (2018) 687–694.

[77] H. Zhang, M. Hu, Q. Lv, L. Yang, R. Lv, Monodisperse nitrogen-doped carbon spheres with superior rate capacities for lithium/sodium ion storage, Electrochim. Acta 297 (2019) 365–371.

[78] Y. Wang, G. Yu, X. Chen, A. Wang, High capacity nano-sized carbon spheres for lithium-ion battery anode materials, Polymers 11 (2019) 645.

[79] J. Ryu, Y.W. Suh, D.J. Suh, D.J. Ahn, Hydrothermal preparation of carbon microspheres from mono-saccharides and phenolic compounds, Carbon 48 (2010) 1990–1998.

[80] W. Sun, Y. Zhang, F. Yang, Tuning electrochemical performance of carbon-sphere-based supercapacitors by compressive stress, Electrochim. Acta 357 (2020) 136874.

[81] Y.C. Zhao, L. Zhao, L.J. Mao, B.H. Han, One-step solvothermal carbonization to microporous carbon materials derived from cyclodextrins, J. Mater. Chem. A 1 (2013) 9456–9461.

[82] X. Lu, C. Jiang, Y. Hu, H. Zhong, Y. Zhao, X. Xu, H. Liu, Preparation of hierarchically porous carbon spheres by hydrothermal carbonization process for high-performance electrochemical capacitors, J. Appl. Electrochem. 48 (2018) 233–241.

[83] C. Falco, N. Baccile, M.M. Titirici, Morphological and structural differences between glucose, cellulose and lignocellulosic biomass derived hydrothermal carbons, Green Chem. 13 (2011) 3273–3281.

[84] L. Liu, Q. Li, Z. Wang, Y. Chen, Phosphorus-doped hollow carbon sphere derived from phytic acid for superior sodium-ion batteries, Mater. Technol. 33 (2018) 748–753.

[85] C. Liang, S. Dai, Synthesis of mesoporous carbon materials via enhanced hydrogen-bonding interaction, J. Am. Chem. Soc. 128 (2006) 5316–5317.

[86] A.H. Lu, G.P. Hao, Q. Sun, Can carbon spheres be created through the stöber method?, Angew. Chemie - Int. Ed. 50 (2011) 9023–9025.

[87]   S. Wang, Y. Li, F. Ma, X. Wu, P. Zhou, Z. Miao, P. Gao, S. Zhuo, J. Zhou, Phenolic resin-based carbon microspheres for potassium ion storage, Appl. Surf. Sci. 506 (2020) 144805.

[88]   X. Wang, J. Zhou, W. Xing, B. Liu, J. Zhang, H. Lin, H. Cui, S. Zhuo, Resorcinol–formaldehyde resin-based porous carbon spheres with high $CO_2$ capture capacities, J. Energy Chem. 26 (2017) 1007–1013.

[89]   H. Tian, J. Liu, K. O'Donnell, T. Liu, X. Liu, Z. Yan, S. Liu, M. Jaroniec, Revisiting the Stöber method: Design of nitrogen-doped porous carbon spheres from molecular precursors of different chemical structures, J. Colloid Interface Sci. 476 (2016) 55–61.

[90]   A.F. Arif, R. Balgis, T. Ogi, T. Mori, K. Okuyama, Experimental and theoretical approach to evaluation of nanostructured carbon particles derived from phenolic resin via spray pyrolysis, Chem. Eng. J. 271 (2015) 79–86.

[91]   A.B.D. Nandiyanto, T. Ogi, W.N. Wang, L. Gradon, K. Okuyama, Template-assisted spray-drying method for the fabrication of porous particles with tunable structures, Adv. Powder Technol. 30 (2019) 2908–2924.

[92]   S. Feng, Z. Liu, Q. Yu, Z. Zhuang, Q. Chen, S. Fu, L. Zhou, L. Mai, Monodisperse carbon sphere-constructed pomegranate-like structures for high-volumetric-capacitance supercapacitors, ACS Appl. Mater. Interfaces 11 (2019) 4011–4016.

[93]   R.S. Varma, Biomass-derived renewable carbonaceous materials for sustainable chemical and environmental applications, ACS Sustain. Chem. Eng. 7 (2019) 6458–6470.

[94]   F. Shen, X. Xiong, J. Fu, J. Yang, M. Qiu, X. Qi, D.C.W. Tsang, Recent advances in mechanochemical production of chemicals and carbon materials from sustainable biomass resources, Renew. Sustain. Energy Rev. 130 (2020) 109944.

[95]   J. Pang, W.F. Zhang, J.L. Zhang, H.M. Zhang, G.P. Cao, M.F. Han, Y.S. Yang, Oxygen and nitrogen co-enriched sustainable porous carbon hollow microspheres from sodium lignosulfonate for supercapacitors with high volumetric energy densities, ChemElectroChem 5 (2018) 1306–1320.

30

[96]   H. Zhou, D. Wang, A. Fu, X. Liu, Y. Wang, Y. Li, P. Guo, H. Li, X.S. Zhao, Mesoporous carbon spheres with tunable porosity prepared by a template-free method for advanced lithium–sulfur batteries, Mater. Sci. Eng. B Solid-State Mater. Adv. Technol. 227 (2018) 9–15.

[97]   S.E. Skrabalak, K.S. Suslick, Carbon powders prepared by ultrasonic spray pyrolysis of substituted alkali benzoates, J. Phys. Chem. C 111 (2007) 17807–17811.

[98]   M.E. Fortunato, M. Rostam-Abadi, K.S. Suslick, Nanostructured carbons prepared by ultrasonic spray pyrolysis, Chem. Mater. 22 (2010) 1610–1612.

[99]   H. Kim, M.E. Fortunato, H. Xu, J.H. Bang, K.S. Suslick, Carbon microspheres as supercapacitors, J. Phys. Chem. C 115 (2011) 20481–20486.

[100]  H. Xu, J. Guo, K.S. Suslick, Porous carbon spheres from energetic carbon precursors using ultrasonic spray pyrolysis, Adv. Mater. 24 (2012) 6028–6033.

[101]  A.D. Roberts, X. Li, H. Zhang, Porous carbon spheres and monoliths: Morphology control, pore size tuning and their applications as Li-ion battery anode materials, Chem. Soc. Rev. 43 (2014) 4341–4356.

[102]  X. Cao, C. Tan, M. Sindoro, H. Zhang, Hybrid micro-/nano-structures derived from metal-organic frameworks: Preparation and applications in energy storage and conversion, Chem. Soc. Rev. 46 (2017) 2660–2677.

[103]  K. Huo, W. An, J. Fu, B. Gao, L. Wang, X. Peng, G.J. Cheng, P.K. Chu, Mesoporous nitrogen-doped carbon hollow spheres as high-performance anodes for lithium-ion batteries, J. Power Sources 324 (2016) 233–238.

[104]  Y. Yang, S. Jin, Z. Zhang, Z. Du, H. Liu, J. Yang, H. Xu, H. Ji, Nitrogen-doped hollow carbon nanospheres for high-performance Li-ion batteries, ACS Appl. Mater. Interfaces 9 (2017) 14180–14186.

[105]  W. Ni, L. Shi, Review article: Layer-structured carbonaceous materials for advanced Li-ion and Na-ion batteries: Beyond graphene, J. Vac. Sci. Technol. A 37 (2019) 040803.

[106] Q. Lin, J. Zhang, W. Lv, J. Ma, Y. He, F. Kang, Q.H. Yang, A functionalized carbon surface for high-performance sodium-ion storage, Small 16 (2020) 1902603.

[107] F. Zheng, Y. Yang, Q. Chen, High lithium anodic performance of highly nitrogen-doped porous carbon prepared from a metal-organic framework, Nat. Commun. 5 (2014) 5261.

[108] H.W. Kim, D.J. Lee, H. Lee, J. Song, H.T. Kim, J.K. Park, Glucosamine-derived encapsulation of silicon nanoparticles for high-performance lithium ion batteries, J. Mater. Chem. A 2 (2014) 14557–14562.

[109] S.M. Yuan, J.X. Li, L.T. Yang, L.W. Su, L. Liu, Z. Zhou, Preparation and lithium storage performances of mesoporous $Fe_3O_4$@C microcapsules, ACS Appl. Mater. Interfaces 3 (2011) 705–709.

[110] X. Yue, W. Sun, J. Zhang, F. Wang, Y. Yang, C. Lu, Z. Wang, D. Rooney, K. Sun, Macro-mesoporous hollow carbon spheres as anodes for lithium-ion batteries with high rate capability and excellent cycling performance, J. Power Sources 331 (2016) 10–15.

[111] X. Yang, C. Wei, C. Sun, X. Li, Y. Chen, High performance anode of lithium-ion batteries derived from an advanced carbonaceous porous network, J. Alloys Compd. 693 (2017) 777–781.

[112] V. Etacheri, C. Wang, M.J. O'Connell, C.K. Chan, V.G. Pol, Porous carbon sphere anodes for enhanced lithium-ion storage, J. Mater. Chem. A 3 (2015) 9861–9868.

[113] S. Chen, J. Wu, R. Zhou, L. Zuo, P. Li, Y. Song, L. Wang, Porous carbon spheres doped with $Fe_3C$ as an anode for high-rate lithium-ion batteries, Electrochim. Acta 180 (2015) 78–85.

[114] S. Zou, X. Xu, Y. Zhu, C. Cao, Microwave-assisted preparation of hollow porous carbon spheres and as anode of lithium-ion batteries, Microporous Mesoporous Mater. 251 (2017) 114–121.

[115] X.W. Lou, D. Deng, J.Y. Lee, L.A. Archer, Preparation of $SnO_2$/carbon composite hollow spheres and their lithium storage properties, Chem. Mater. 20 (2008) 6562–6566.

[116] X. yan Li, Q. gui Xiao, Y. ying Gao, H. ling Zhang, H. bin Xu, Y. Zhang, Hierarchical MoO$_2$/C microspheres: Preparation and application as anode materials for lithium ion batteries, J. Alloys Compd. 723 (2017) 1113–1120.

[117] Z. Sun, Y. Yao, J. Wang, X. Song, P. Zhang, L. Zhao, L. Gao, High rate lithium-ion batteries from hybrid hollow spheres with a few-layered MoS$_2$-entrapped carbon sheath synthesized by a space-confined reaction, J. Mater. Chem. A 4 (2016) 10425–10434.

[118] Y. Chen, B. Song, M. Li, L. Lu, J. Xue, Fe$_3$O$_4$ nanoparticles embedded in uniform mesoporous carbon spheres for superior high-rate battery applications, Adv. Funct. Mater. 24 (2014) 319–326.

[119] M. Li, Y. Zeng, Y. Ren, C. Zeng, J. Gu, X. Feng, H. He, Fabrication and lithium storage performance of sugar apple-shaped SiO$_x$@C nanocomposite spheres, J. Power Sources 288 (2015) 53–61.

[120] J. Wang, W. Li, F. Wang, Y. Xia, A.M. Asiri, D. Zhao, Controllable synthesis of SnO$_2$@C yolk-shell nanospheres as a high-performance anode material for lithium ion batteries, Nanoscale 6 (2014) 3217–3222.

[121] J. Wang, L. Shen, B. Ding, P. Nie, H. Deng, H. Dou, X. Zhang, Fabrication of porous carbon spheres for high-performance electrochemical capacitors, RSC Adv. 4 (2014) 7538–7544.

[122] Z. Wu, W. Li, Y. Xia, P. Webley, D. Zhao, Ordered mesoporous graphitized pyrolytic carbon materials: Synthesis, graphitization, and electrochemical properties, J. Mater. Chem. 22 (2012) 8835–8845.

[123] P. Simon, Y. Gogotsi, Capacitive energy storage in nanostructured carbon-electrolyte systems, Acc. Chem. Res. 46 (2013) 1094–1103.

[124] J.W.F. To, Z. Chen, H. Yao, J. He, K. Kim, H.H. Chou, L. Pan, J. Wilcox, Y. Cui, Z. Bao, Ultrahigh surface area three-dimensional porous graphitic carbon from conjugated polymeric molecular framework, ACS Cent. Sci. 1 (2015) 68–76.

[125] T. Kou, B. Yao, T. Liu, Y. Li, Recent advances in chemical methods for activating carbon and metal oxide based electrodes for supercapacitors, J. Mater. Chem. A 5 (2017) 17151–17173.

[126] C. Largeot, C. Portet, J. Chmiola, P.L. Taberna, Y. Gogotsi, P. Simon, Relation between the ion size and pore size for an electric double-layer capacitor, J. Am. Chem. Soc. 130 (2008) 2730–2731.

[127] G. Feng, P.T. Cummings, Supercapacitor capacitance exhibits oscillatory behavior as a function of nanopore size, J. Phys. Chem. Lett. 2 (2011) 2859–2864.

[128] F. Zhang, T. Liu, M. Li, M. Yu, Y. Luo, Y. Tong, Y. Li, Multiscale pore network boosts capacitance of carbon electrodes for ultrafast charging, Nano Lett. 17 (2017) 3097–3104.

[129] T. Cai, W. Xing, Z. Liu, J. Zeng, Q. Xue, S. Qiao, Z. Yan, Superhigh-rate capacitive performance of heteroatoms-doped double shell hollow carbon spheres, Carbon 86 (2015) 235–244.

[130] S. Liu, Y. Cai, X. Zhao, Y. Liang, M. Zheng, H. Hu, H. Dong, S. Jiang, Y. Liu, Y. Xiao, Sulfur-doped nanoporous carbon spheres with ultrahigh specific surface area and high electrochemical activity for supercapacitor, J. Power Sources 360 (2017) 373–382.

[131] M. Seredych, D. Hulicova-Jurcakova, G.Q. Lu, T.J. Bandosz, Surface functional groups of carbons and the effects of their chemical character, density and accessibility to ions on electrochemical performance, Carbon 46 (2008) 1475–1488.

[132] D. Bhattacharjya, M.S. Kim, T.S. Bae, J.S. Yu, High performance supercapacitor prepared from hollow mesoporous carbon capsules with hierarchical nanoarchitecture, J. Power Sources 244 (2013) 799–805.

[133] F. Xu, Z. Tang, S. Huang, L. Chen, Y. Liang, W. Mai, H. Zhong, R. Fu, D. Wu, Facile synthesis of ultrahigh-surface-area hollow carbon nanospheres for enhanced adsorption and energy storage, Nat. Commun. 6 (2015) 7221.

[134] H. Zhang, O. Noonan, X. Huang, Y. Yang, C. Xu, L. Zhou, C. Yu, Surfactant-free

assembly of mesoporous carbon hollow spheres with large tunable pore sizes, ACS Nano 10 (2016) 4579–4586.

[135] C. Liu, J. Wang, J. Li, R. Luo, J. Shen, X. Sun, W. Han, L. Wang, Controllable synthesis of functional hollow carbon nanostructures with dopamine as precursor for supercapacitors, ACS Appl. Mater. Interfaces 7 (2015) 18609–18617.

[136] H. Liu, Y. Zhang, Q. Ke, K.H. Ho, Y. Hu, J. Wang, Tuning the porous texture and specific surface area of nanoporous carbons for supercapacitor electrodes by adjusting the hydrothermal synthesis temperature, J. Mater. Chem. A 1 (2013) 12962–12970.

[137] Y. Han, X. Dong, C. Zhang, S. Liu, Hierarchical porous carbon hollow-spheres as a high performance electrical double-layer capacitor material, J. Power Sources 211 (2012) 92–96.

[138] C. Wang, Y. Wang, J. Graser, R. Zhao, F. Gao, M.J. O'Connell, Solution-based carbohydrate synthesis of individual solid, hollow, and porous carbon nanospheres using spray pyrolysis, ACS Nano 7 (2013) 11156–11165.

# Chapter 2

# Controllable Synthesis of Carbon-Coated SiO$_x$ Particles through a Simultaneous Reaction between the Hydrolysis-Condensation of Tetramethyl Orthosilicate and the Polymerization of 3-Aminophenol

## 2.1. Introduction

Nanostructured materials are potential next-generation materials with enhanced performances and new functionalities for energy and environmental applications [1–4]. Among nanostructured particles, core−shell particles have recently received considerable attention as highly functional materials with distinctive and fascinating properties [5–8]. These excellent properties make them good candidates for use in a broad range of potential applications, such as optical devices [9], sensing [10], magnetic imaging [11], catalysis [12], water splitting [13], drug delivery [14], and energy storage [15–17]. Although many methods have been developed for preparing core−shell particles, the synthesis of core−shell particles with well-controlled morphologies and structures is still a great challenge.

Lithium-ion batteries (LIBs) have a wide range of applications; for example, in portable electronic devices, electrical tools, electric and hybrid electric vehicles, due to their high energy densities, long life-expectancies, high operational voltages, low self-discharge rates, and environmental benignity [18–20]. Silicon suboxide (SiO$_x$) has been extensively investigated as one of the most promising anode materials for LIBs because of its high theoretical specific capacity (1965 mAh g$^{-1}$ for SiO$_2$ and 2680 mAh g$^{-1}$ for SiO), satisfactory working potential, high abundance in the earth's crust, and low cost [21–23]. However, SiO$_x$-based anodes easily undergo a large volume expansion (>200%) and low electrical conductivity leads to a poor rate capability [24]. To address these problems, several approaches have been developed for effective

modification of SiO$_x$. One effective strategy is to reduce the SiO$_x$ particle size, which alleviates the strain induced by the volume change and improves the cycling stability [25,26]. However, practical applications of SiO$_x$ are still hindered by its poor electrical conductivity and low coulombic efficiency (CE). Hence, a potential and straightforward solution is to integrate SiO$_x$ with carbon because the benefits of the carbon with excellent mechanical elasticity and intrinsic conductivity are considered to increase the electrical conductivity of the composite as well as accommodate volume expansion during charge–discharge processes to maintain a stable electrochemical performance [27]. Izawa et al. [28] reported the preparation of SiO$_x$/C nanocomposite by simultaneous hydrolysis-condensation of tetraethyl orthosilicate (TEOS) and polymerization of 3-aminophenol. In this case, the hydrolysis of TEOS was slower than 3-aminophenol polymerization; therefore, the SiO$_x$ nanoparticles were dispersed on the polymer surface and the carbon layer did not perfectly coat the SiO$_x$. The composite had a low reversible capacity of 383 mAh g$^{-1}$, which indicates that the electrochemical performance was significantly affected by the structure of SiO$_x$/C. For this reason, precise design and control the structure of SiO$_x$/C is therefore necessary. Design of the ideal structure should enable optimum contact with the carbon matrix, which will lead to a better electron transfer from/to SiO$_x$ and the local structural stability of the electrode during cycling [29]. Spherical carbon-coated SiO$_x$ particles (*i.e.* SiO$_x$@C core−shell particles) are one candidate because of the possibility for good electron transfer among the composite constituents and improved resilience toward internal stress. The development of new processes for the preparation of SiO$_x$@C particles with spherical morphologies and excellent lithium storage abilities is therefore important. It is noteworthy that the use of an appropriate precursor is very important for obtaining desired structures and functionalities.

In this contribution, we report a fundamental modification of the synthetic process by using an alternative silica precursor rather than the conventionally used TEOS. It has been demonstrated that the alkyl-chain length governs the reactivity of tetraalkoxysilanes [30]. Thus, we reasonably assume that the alkyl-chain length can also affect the substituting abilities of tetraalkoxysilanes. With this in mind, tetramethyl orthosilicate (TMOS) was selected for this study. It is known that the methoxy residue (Me−O−Si) usually hydrolyzes faster than the ethoxy residue (Et−O−Si) [31]. Furthermore, the hydrolysis and condensation reactions involving

TMOS generate methanol as a byproduct that could be recycled. A process that releases methanol may be more appealing for commercial applications that involve a large scale of the process. From that point, control of the TMOS reaction rate enables the nucleation of SiO$_2$ in the formation of SiO$_x$@C particles. Other advantages of TMOS are that it is inexpensive, readily available, simple to handle, and easy to remove from the reaction mixtures. Moreover, to the best of our knowledge, the use of TMOS in the preparation of core−shell particles has not been previously investigated. A combination of these advantages make TMOS a promising silica precursor to produce SiO$_x$@C particles and renders this approach attractive for future applications.

Our proposed strategy for synthesizing SiO$_x$@C particles is shown in **Figure 2.1**. The fabrication process used 3-aminophenol and formaldehyde as carbon precursors, TMOS as a silica precursor, ammonia as a basic catalyst, and cetyltrimethylammonium bromide (CTAB) as a cationic surfactant in a mixed water-methanol solvent. First, CTAB micelles are formed in the ternary solution (ammonia-water-methanol). Then, the simultaneous hydrolysis-condensation of TMOS and polymerization of 3-aminophenol generated 3-aminophenol/formaldehyde (APF) resin-coated SiO$_2$ particles (*i.e.* SiO$_2$@APF resin core−shell particles) [32]. These could be converted into carbon through a simple carbonization process to obtain the SiO$_x$@C particles. These core−shell particles provide great potential interest because the constituent materials have complementary properties: the carbon shell has high electrical conductivity and the silica core is easily functionalized. The benefits of the core−shell structure in energy storage were investigated by evaluating the performance of SiO$_x$@C as an anode material in LIBs.

$$(i) \quad Si(OCH_3)_4 \quad + \quad 2H_2O \quad \xrightarrow{\text{NH}_{3\,\text{cat.}}} \quad SiO_2 \quad + \quad 4CH_3OH$$
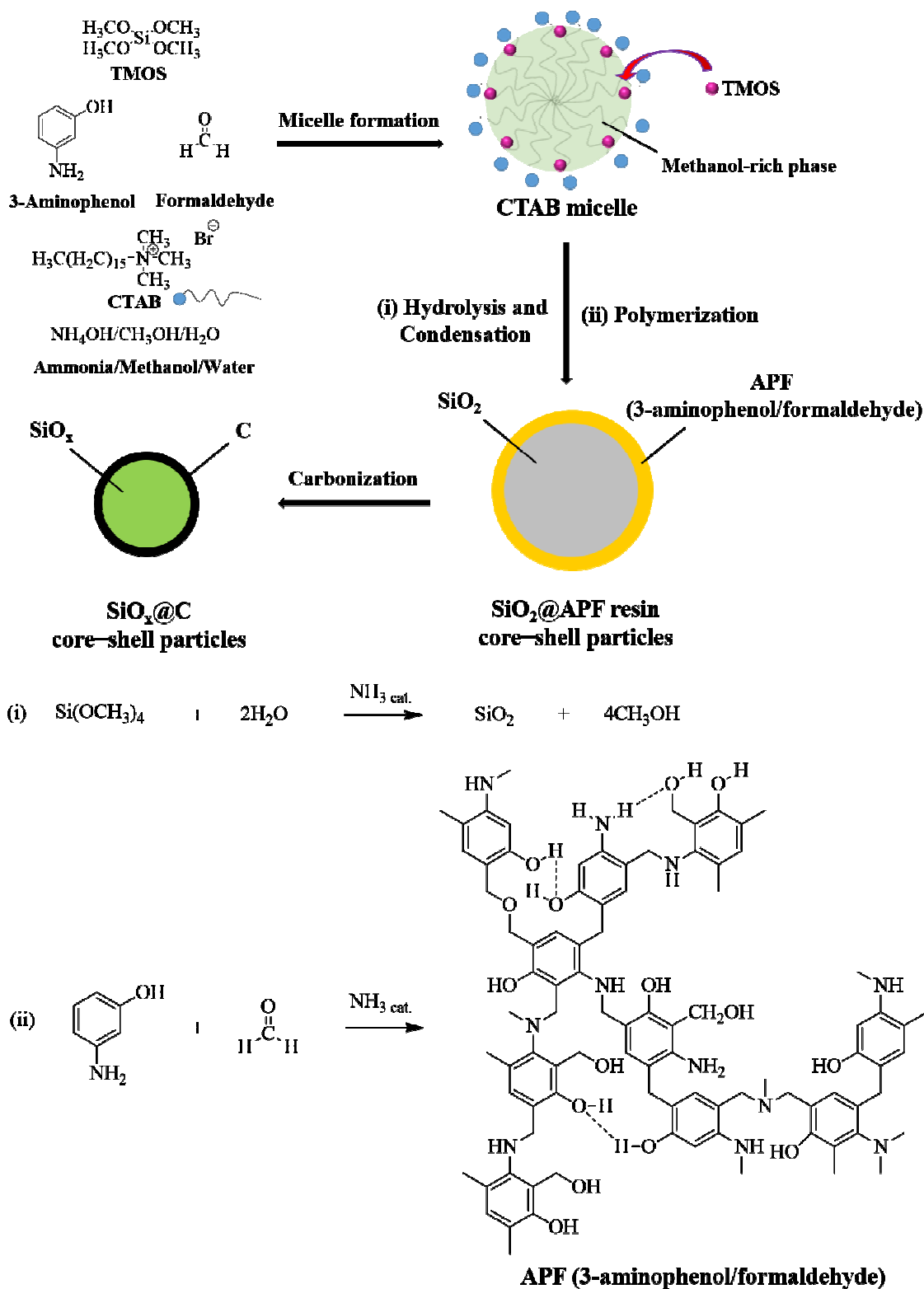
**Figure 2.1.** Schematic illustration of the synthesis of SiO$_x$@C particles.

## 2.2. Experimental

### 2.2.1. Synthesis of SiOx@C particles

All the chemicals and solvents used in this work were analytical grade and used as received without further purification. In a typical procedure, ammonia solution (1 M, Kanto Chemical Co., Inc., Tokyo, Japan) was mixed with 3-aminophenol (Sigma-Aldrich, St. Louis, MO) in ultrapure water. After stirring at room temperature until the solution became clear, CTAB (Sigma-Aldrich, St. Louis, MO) dissolved in methanol was added and continually stirred for 15 min. Then TMOS (99.9%, Sigma-Aldrich, St. Louis, MO) and formaldehyde (Kanto Chemical Co., Inc., Tokyo, Japan) were simultaneously added to the solution. The reaction mixture was placed in a microwave reactor ($\mu$-Reactor, Shikokukeisokukogyo, Kagawa, Japan) and stirred at 40 °C. After 15 min, the temperature was increased to 70 °C and kept constant for 75 min. The resulting $SiO_2$@APF resin particles were isolated from the solution by centrifugation at 8000 rpm and washed with ethanol and ultrapure water several times. After drying in a vacuum oven, the particles were carbonized in a tube furnace at 1200 °C for 3 h under nitrogen atmosphere (1.0 L min$^{-1}$). The samples were then cooled to room temperature to obtain $SiO_x$@C particles. Details of the conditions for sample preparation for $SiO_2$@APF resin and $SiO_x$@C particles are summarized in **Table 2.1**.

**Table 2.1a.** List of SiO$_2$@APF resin particles and their corresponding figure(s) in the chapter 2.

| Sample | Methanol (mL) | CTAB (g) | 3-Aminophenol (g) | Water (mL) | Ammonia (mL) | TMOS (mL) | Formaldehyde (mL) | Corresponding figure(s) |
|---|---|---|---|---|---|---|---|---|
| R1 | 52.0 | 0.75 | 0.266 | 47.4 | 2.32 | 0.0884 | 0.368 | 2.2(a), 2.4(d) |
| R2 | 0 | 0.75 | 0.266 | 99.4 | 2.32 | 0.0884 | 0.368 | 2.2(b) |
| R3 | 52.0 | 0 | 0.266 | 47.4 | 2.32 | 0.0884 | 0.368 | 2.2(c) |
| R4 | 17.3 | 0.75 | 0.266 | 47.4 | 2.32 | 0.0884 | 0.368 | 2.4(a) |
| R5 | 34.6 | 0.75 | 0.266 | 47.4 | 2.32 | 0.0884 | 0.368 | 2.4(b) |
| R6 | 43.3 | 0.75 | 0.266 | 47.4 | 2.32 | 0.0884 | 0.368 | 2.4(c) |
| R7 | 60.6 | 0.75 | 0.266 | 47.4 | 2.32 | 0.0884 | 0.368 | 2.4(e) |

**Table 2.1b.** List of SiO$_x$@C particles and their corresponding figure(s) in the chapter 2.

| Sample[a] | Methanol (mL) | CTAB (g) | 3-Aminophenol (g) | Water (mL) | Ammonia (mL) | TMOS (mL) | Formaldehyde (mL) | Corresponding figure(s) |
|---|---|---|---|---|---|---|---|---|
| C1 | 52.0 | 0.75 | 0.266 | 47.4 | 2.32 | 0.0884 | 0.368 | 2.6(a) |
| C2 | 52.0 | 0.75 | 0.199 | 47.4 | 2.32 | 0.0884 | 0.368 | 2.6(b) |
| C3 | 52.0 | 0.75 | 0.133 | 47.4 | 2.32 | 0.0884 | 0.368 | 2.6(c), 2.7(a) |

[a]: Carbonization conditions: nitrogen atmosphere, 3 h, 1200 °C.

## 2.2.2. Characterization

The morphologies of the synthesized SiO$_2$@APF resin and SiO$_x$@C particles were examined by field emission scanning electron microscopy (SEM; S-5200, 20 kV, Hitachi High-Technologies. Corp., Tokyo, Japan) and transmission electron microscopy (TEM; JEM-2010, 200 kV, JEOL Ltd., Tokyo, Japan). The particle size and shell thickness were determined by measuring approximately 350 randomly selected particles totally from SEM and TEM images. The elemental distribution in the prepared samples was carried out via an energy-dispersive X-ray spectroscopy (EDX) attached to the TEM apparatus. The micelle size and zeta potential were determined at 25 °C by dynamic light scattering (DLS; Zetasizer Nano ZSP, Malvern Instruments Ltd., Malvern, UK). The functional groups and chemical compositions of the

prepared samples during the microwave irradiation process were investigated by Fourier-transform infrared (FT-IR) spectroscopy (Spectrum One, Perkin Elmer Inc., Waltham, MA, USA). The content of SiO$_x$ in SiO$_x$@C particles was investigated by thermogravimetric analysis (TGA; TGA-50/51 Shimadzu Corp., Kyoto, Japan). Elemental analysis was carried out using X-ray photoelectron spectroscopy (XPS; PHI Quantera II, Physical Electronics, Chanhassen, MN, USA). The nitrogen adsorption−desorption properties of the SiO$_x$@C particles were measured using gas adsorption measurement equipment (BELSORP-max, MicrotracBEL Corp., Osaka, Japan), and the specific surface area was calculated using Brunauer−Emmett−Teller (BET) method from the nitrogen isotherm curve. The existence of carbon was investigated using Raman spectroscopy (Renishaw in Viamicro-Raman spectroscopy system equipped with a 514.5 nm laser).

### *2.2.3. Electrochemical measurements*

The electrode was prepared by coating copper foil with a slurry consisting of the active material powder (96 wt%) and poly(vinylidene fluoride) (4 wt%). After drying at 80 ℃ on a hot plate for 30 min, the copper foil containing the active materials was tightly pressed using a roll press. The pressed electrode was placed in a vacuum drying oven for 3 h and punched into circular discs with a diameter of 14 mm for use as the working electrode. For measuring the electrochemical performance of electrode, 2032 coin-type half-cells were assembled in a high purity argon-filled glove box using lithium foil as the counter electrode, and lithium hexafluorophosphate (1 M) in a mixture of ethylene carbonate, dimethyl carbonate, and ethyl methyl carbonate with a volume ratio of 1:1:1 as the electrolyte. The cell performance was evaluated by the galvanostatic charge−discharge cycling tests, which were measured in the potential range of 0.01 − 1.4 V versus Li/Li$^+$ using a TOSCAT-3100 (Tokyo System Co., Ltd., Japan) battery system. The whole process was carried out using a constant current density for charging and discharging. The current density was determined in terms of the rate of charging and denoted as C rate. In this study, the current density applied was 0.2 C (100 mA$_{SiOx@C}$-g$^{-1}$) for SiO$_x$@C electrode. SiO$_x$@C particles were developed for the negative electrode. However, for the batteries test, SiO$_x$@C particles were used as the cathode. Cyclic voltammetry (CV) and electrochemical impedance spectroscopy (EIS) measurements were recorded at room

temperature using an electrochemical workstation (CHI 760D, Shanghai CH Instruments Co., China). The CV curves were measured at a scan rate of 0.1 mV s$^{-1}$ in the potential range of 0.01 – 1.4 V. The EIS spectra were carried out in the frequency region from 100 kHz to 0.01 Hz with a signal amplitude of 5 mV.

## 2.3. Results and Discussion

### 2.3.1. Preparation of SiO$_2$@APF resin particles

In a typical coating process, the compatibility between the core surface and the shell is one of the most important factors in achieving successful coating [31,33–35]. In the initial experiment, when methanol and CTAB were present in the reaction system, the core−shell particles with a highly uniform spherical morphology were successfully formed as shown in the SEM and TEM results (**Figure 2.2(a)**). The TEM image in **Figure 2.2(a-2)** implies that the coating of APF resin is well-distributed outside as the shell and most part of SiO$_2$ particles act as the core were inserted. A clear contrast indicates a gap between the core and the shell, which further confirms the core−shell structure. In addition, EDX analysis was used to determine the elemental distributions of carbon, silicon, and oxygen in the sample. As seen in **Figure 2.2(a-3)** and **2.2(a-4)**, the contents of silicon and oxygen elements inside the obtained particles are higher than those outside. On the other hand, comparative experiments were performed to understand the functions of methanol and CTAB in the core−shell particle formation. In the absence of methanol, no core−shell structure was obtained after the reaction as shown in **Figure 2.2(b)**. The formation of irregular morphologies and a large amount of aggregated particles were observed, indicating the shape of the particles can be adjusted through control the presence of methanol. In the absence of CTAB, APF resin particles and SiO$_2$ particles were formed without a uniform core−shell structure as shown in **Figure 2.2(c)**. Furthermore, EDX analysis was performed to determine the chemical composition of these particles (**Figure 2.2(c-3)** and **2.2 (c-4)**). Compared with **Figure 2.2(a-3)** and **2.2(a-4)**, a large amount of silicon and oxygen constituents were present outside the sample, which strongly indicates that no core−shell structure formation occurred in this case. These results clearly show that methanol and CTAB play a crucial role in

the formation of particles with a core−shell structure. If either of these reactants is absent, the synthesis will be unsuccessful.
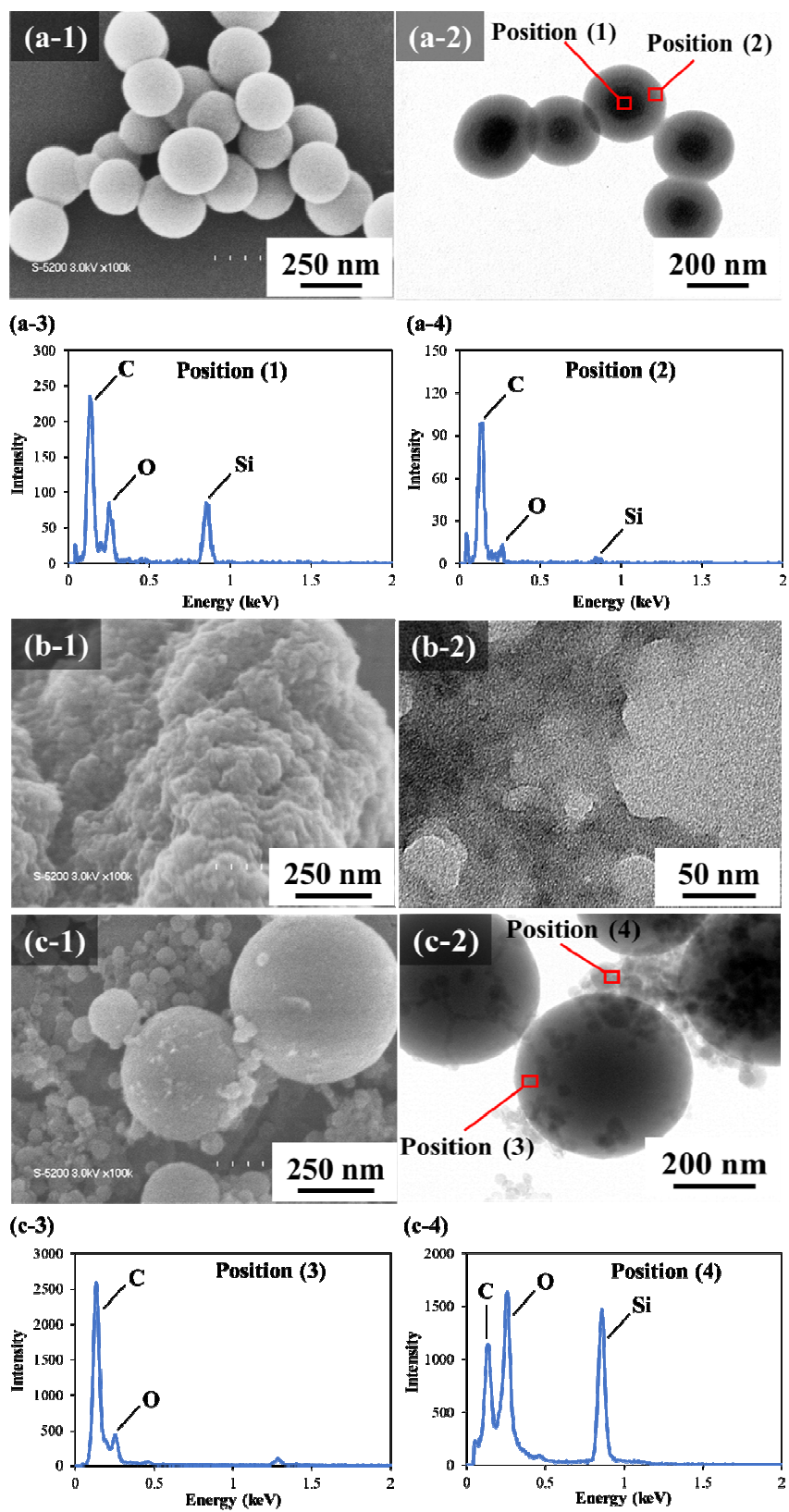
**Figure 2.2.** Images of SiO$_2$@APF resin particles synthesized (a) with methanol and CTAB (**R1**), (b) without methanol (**R2**), and (c) without CTAB (**R3**); (a-1, b-1, c-1) SEM images, (a-2, b-2, c-2) TEM images, and (a-3, a-4, c-3, c-4) EDX results.

On the basis of these observations, we propose a possible mechanism for the formation of a core−shell structure (**Figure 2.3(i)**). With respect to nucleation, the formation of core−shell structure is dominated by homogeneous and heterogeneous nucleation, and the heterogeneous nucleation is favored due to the lower energy barrier [36]. In the case of using methanol and CTAB, the cationic surfactant (*i.e.* CTAB) formed micelles in the ternary solution (ammonia-methanol-water). Because the dielectric constant of methanol (32.6) is lower than that of water (78.5) [37], it is easier for methanol to penetrate the interior of the CTAB micelle due to the hydrophobic interaction, forming a methanol-rich phase inside the micelle. Upon adding TMOS under stirring, it would diffuse into the internal hydrophobic region of the CTAB micelles together with methanol due to their hydrophobic properties (**Figure 2.3(i)-(1)**). The CTAB micelle is positively charged with a zeta potential value of around +19.1 mV. The SiO$_2$ species from the hydrolysis and condensation reactions of TMOS can first assemble with CTAB micelles through electrical interactions (**Figure 2.3(i)-(2)** and **(i)-(3)**). Then, the reaction between 3-aminophenol and formaldehyde will occur in the presence of ammonia as a catalyst [32], which generates APF resin intermediates in the ternary solution (**Figure 2.3(i)-(4)**). According to our previous paper [35], the APF resin generated from a similar reaction system has a negative charge (−20.0 mV). Therefore, the APF resin can assemble with the positively charged CTAB micelle through the assistance of electrostatic interactions, which results in the formation of an APF outer shell surrounding a SiO$_2$ core (**Figure 2.3(i)-(5)**). Because the hydrolysis and condensation rate of TMOS are faster than the polymerization rate of APF in the initial stage, the SiO$_2$ particles are formed as the core, eventually producing a core−shell structure.

In the absence of methanol (**Figure 2.3(ii)**), the polarity of the solvent is increased and the hydrolysis rate of TMOS is fast, thus resulting in a fast nucleation of SiO$_2$. When CTAB is dissolved in only water, the hydrophobic carbon chain, which has a lower dielectric constant, rapidly escapes from the water medium and smaller diameter micelles are formed [38]. The negatively charged SiO$_2$ nuclei and APF resin can easily connect with CTAB to form aggregation. It is accepted that methanol plays an essential role in the formation of stable APF

resin/$SiO_2$ aggregates, which contributes to control the hydrolysis and condensation rate of TMOS, and TMOS hydrolysis takes place in the CTAB-stabilized methanol/water micelle.

From this proposed mechanism, it is noteworthy that the participation of CTAB plays an important role in the formation of core−shell structure. Without CTAB (**Figure 2.3(iii)**), it is difficult to induce an efficient assembly, the negatively charged APF resin and $SiO_2$ particles do not attract each other due to the electrostatic repulsion; therefore, most of them remain stable in the ternary solution. This result demonstrated that the corresponding self-assembly between the APF resin and $SiO_2$ particles cannot take place, so the core−shell structure cannot be obtained.

○ :SiO$_2$      ● :Resin      ● :3-AP      ∿ :CTAB      ● :TMOS

## (i) With methanol and CTAB

TMOS (2) SiO$_2$    3-AP (4) resin    resin    SiO$_2$

(1)   (3)   (5)

Methanol-rich phase

CTAB micelle

SiO$_2$@APF resin core−shell particles

(1) Hydrophobic interaction
(2) Hydrolysis reaction
(3) Electrical interaction

(4) 3-AP polymerization
(5) Electrical interaction

## (ii) Without methanol

TMOS (1) SiO$_2$    resin (2) 3-AP

CTAB micelle

SiO$_2$ + APF resin aggregates

(1) Hydrolysis reaction (fast)
(2) Polymerization

## (iii) Without CTAB

TMOS (1) SiO$_2$

3-AP (2) resin

SiO$_2$ and APF resin remained stable

(1) Hydrolysis reaction
(2) Polymerization

**Figure 2.3.** Schematic illustration of the formation mechanism of SiO$_2$@APF resin particles.

48

We further evaluated the effect of methanol concentration in the reaction system by varying the methanol/water molar ratio and observing the morphologies of the resulting particles as shown in **Figure 2.4**.

**Figure 2.4(a–e)** show the SEM and TEM images of SiO$_2$@APF resin particles synthesized with different amounts of methanol. **Figure 2.4(f)** shows that the composite particle size increases from 29 to 316 nm with increasing methanol/water molar ratio from 0.16 to 0.57. As a control, the relationship between the CTAB micelle size and the methanol/water molar ratio was also carried out by DLS. The overall trend in the SiO$_2$@APF resin particle size was consistent with the trend in the CTAB-stabilized micelle size at different methanol/water ratios (**Figure 2.4(f)**). This consistency in the trend strongly indicates that both 3-aminophenol polymerization and TMOS hydrolysis took place in the CTAB-stabilized methanol/water micelle. Furthermore, it is interesting that a change of methanol/water ratio in the synthesis solution also affects the composite structure. The core−shell structure was not formed at a low methanol/water ratio (0.16) as shown in **Figure 2.4(a-2)**. In this case, the hydrolysis reaction rate of TMOS is fast, and homogeneous nucleation tends to occur rapidly, which leads to the formation of APF resin/SiO$_2$ aggregates. This phenomenon was the same as that observed in the case of without methanol, which has been discussed earlier. Addition of more methanol to the reaction system up to a certain methanol/water ratio improves the dispersion of the particles. **Figure 2.4(b-2)**, **2.4(c-2)**, **2.4(d-2)**, and **2.4(e-2)** show that the core−shell particles with a relatively smooth surface were successfully produced at methanol/water ratios of 0.32, 0.40, 0.49, and 0.57, respectively, indicating the high quality of our synthetic method. In comparison with the heavily necking particles in **Figure 2.4(a-2),** the particles are homogeneously dispersed as shown in **Figure 2.4(d-2)**. Therefore, the optimum methanol/water ratio is 0.49. The particle size distribution of SiO$_2$@APF resin at this ratio was determined and the results are shown in **Figure 2.4(g)**. The average particle size ($D_P$) is 206 nm and the size distribution is very narrow with a geometric standard deviation $\sigma_g \approx 1.1$.
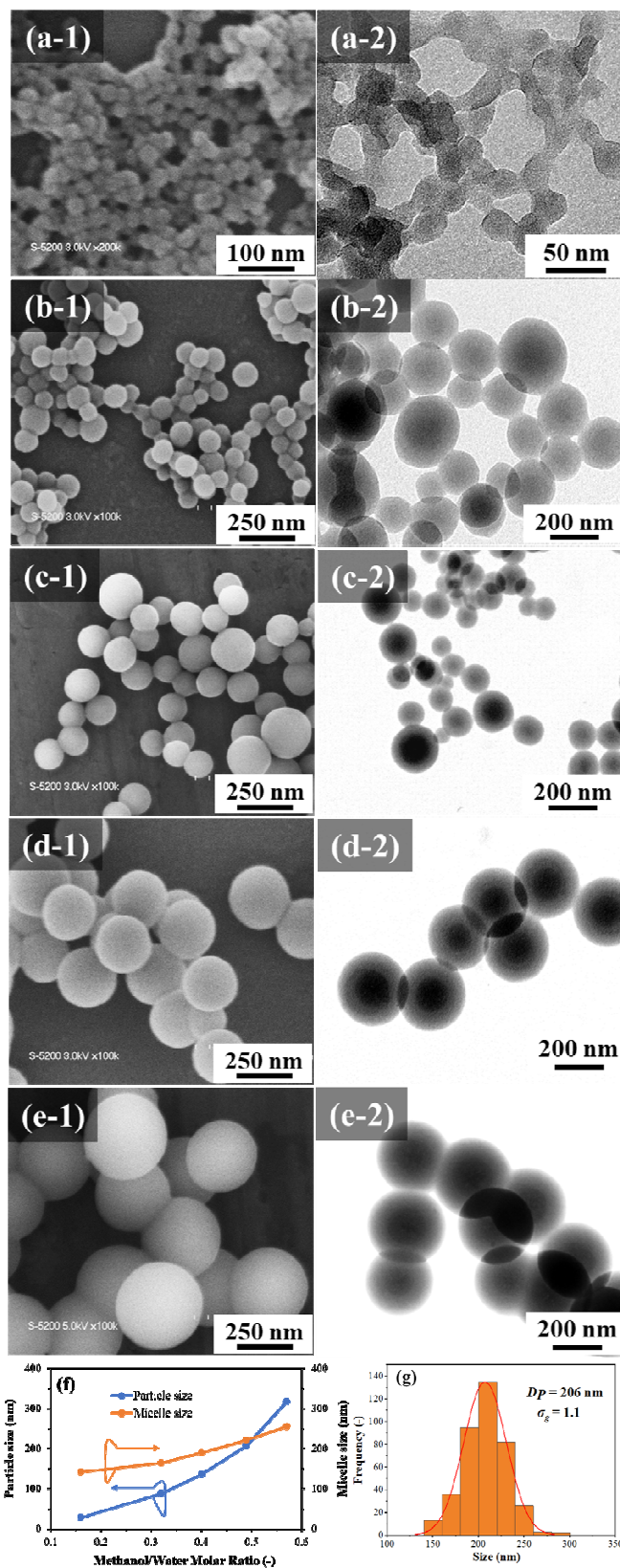
**Figure 2.4.** Images of SiO$_2$@APF resin particles synthesized using different methanol/water molar ratio of 0.16 (**R4**), 0.32 (**R5**), 0.40 (**R6**), 0.49 (**R1**), and 0.57 (**R7**); (a-1−e-1) SEM images, (a-2−e-2) TEM images; (f) Relationship between methanol/water molar ratio and particle size, micelle size; (g) Particle size distribution for sample (**R1**) SiO$_2$@APF resin particles using methanol/water ratio of 0.49.

The SiO$_2$@APF resin particles formed at a methanol/water molar ratio of 0.49 were further examined by FT-IR spectroscopy (**Figure 2.5**). FT-IR spectroscopy is used to identify the material composition and functional groups present in a sample. The FT-IR spectra were measured at room temperature in the spectral range from 500 to 4000 cm$^{-1}$. The absorption peak at 1080 cm$^{-1}$ corresponds to C–O–C stretching [39]. The peaks at 1620, 1506, and 1456 cm$^{-1}$ are assigned to C=C stretching vibrations in the aromatic rings [40]. The peak at 2359 cm$^{-1}$ corresponds to the absorbance of CO$_2$ from ambient air [41]. The two obvious peaks at 2922 and 2853 cm$^{-1}$ are attributed to the stretching vibration of –CH$_2$– [42]. The appearance of these peaks may contribute to the APF resin of the core−shell particles.
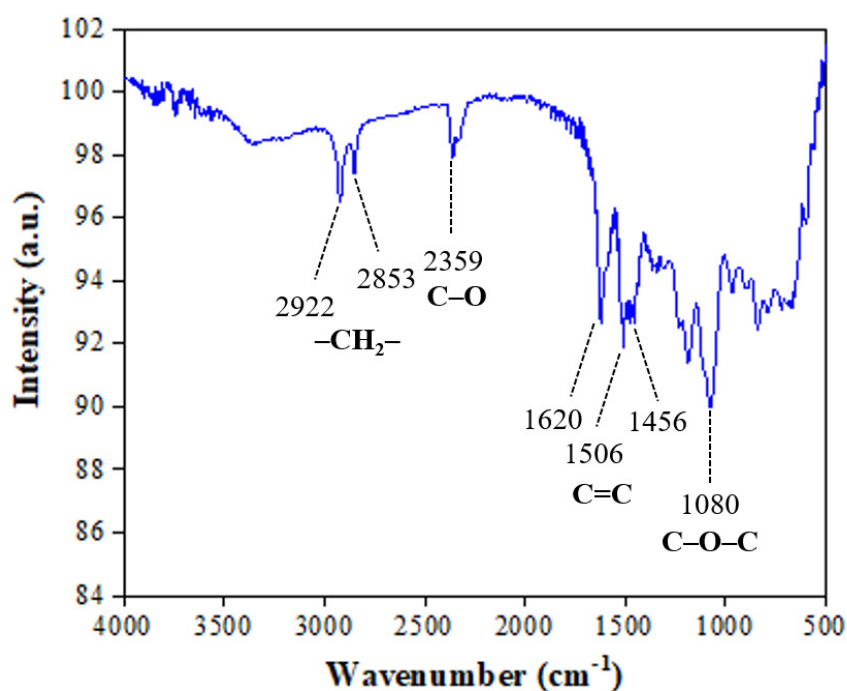


**Figure 2.5.** FT-IR spectrum of sample (**R1**) SiO$_2$@APF resin particles formed at methanol/water molar ratio of 0.49.

51

*2.3.2. Preparation of SiO$_x$@C particles*

The SiO$_2$@APF resin particles can be readily converted into carbon through a simple carbonization process in a nitrogen atmosphere at 1200 °C to obtain the SiO$_x$@C particles, which maintained their structural integrity and spherical morphology, as can be observed in the SEM and TEM images in **Figure 2.6(a)**. The resulting particles exhibited excellent thermal stability. However, the carbon shell thickness became smaller than that of the shell before carbonization; for example, it decreases from 76 nm in the SiO$_2$@APF resin to 29 nm due to the shrinkage during the carbonization process. A primary advantage of the developed synthetic approach is that the shell thickness of the core−shell particles can be precisely adjusted by simply controlling the amount of 3-aminophenol precursor, while keeping all the other synthetic parameters constant. This provides an effective method for creating core−shell particles with a thin shell, which is highly desirable for application in high-performance LIBs. **Figure 2.6** shows that the carbon shell thickness of the particles decreases from 29 to 13 nm by gradually decreasing amount of 3-aminophenol from 0.266 to 0.133 g. This result is consistent with the previously reported results for the synthesis of SiO$_2$ or carbon spheres via sol-gel method [43].
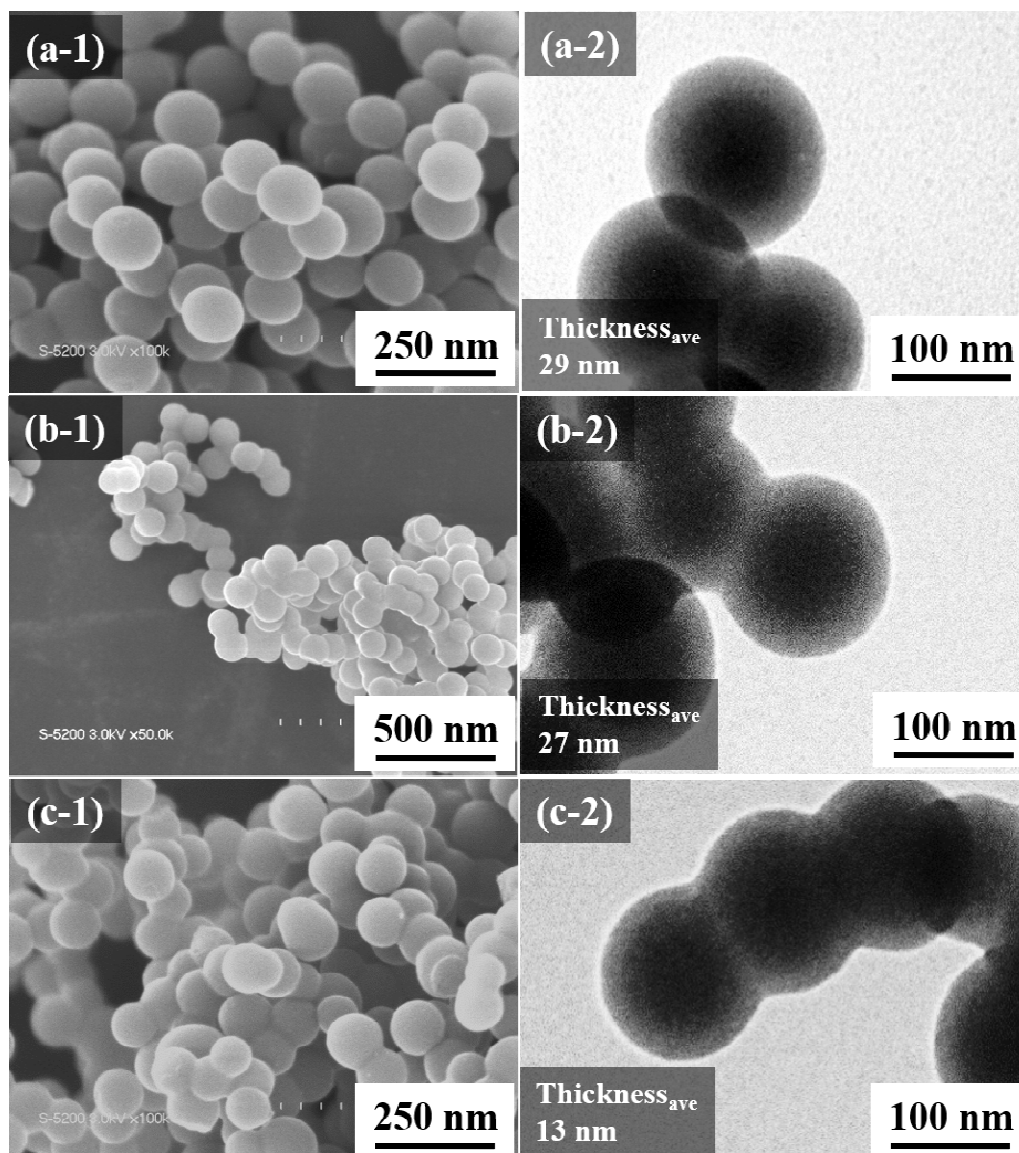
**Figure 2.6.** Images of SiO$_x$@C particles synthesized at different amount of 3-aminophenol of (a) 0.266 g (**C1**), (b) 0.199 g (**C2**), and (c) 0.133 g (**C3**); (a-1−c-1) SEM, (a-2−c-2) TEM images.

For a better understanding of the SiO$_x$@C particle properties, different characterizations were carried out as shown in **Figure 2.7**. Sample **C3** with a thin shell (13 nm) as shown in **Figure 2.7(a)** was used as an example. Compared with **Figure 2.4(d-2)**, the particles in **Figure 2.7(a-2)** were not homogeneously dispersed. However, the core−shell particles with a thin shell may be expected to be very beneficial to enhance the diffusion of ions and electrons, relieve the

53

volume change and pulverize the active material upon discharge−charge processes [44]. This can contribute to the fully utilizing the active SiO$_x$ and provides a positive effect on the electrochemical performance of LIBs. In order to verify the SiO$_x$ content in this sample, the TGA data were collected. The result shown in **Figure 2.7(b)** demonstrates that the SiO$_x$ content in the SiO$_x$@C particles is approximately 33.3 wt%.

XPS was applied to reveal the elemental information and their chemical valence states in the composite constituents, as illustrated in **Figure 2.7(c–e)**. The C 1s spectrum (**Figure 2.7(c)**) shows a sharp peak at a binding energy of about 283.8 eV, which is related to C–C bond [24]. Furthermore, no peaks at 282.2 eV were observed, which suggested the absence of C–Si bond [45]. The peak observed at about 532.1 eV in the O 1s spectrum (**Figure 2.7(d)**) corresponds to C–O–C bond. This peak consisted of overlapped peaks for C–O–Si and Si–O–Si bonds, which suggested a formation of SiOC phase [46]. In addition, the Si 2p spectrum (**Figure 2.7(e)**) showed that a broad peak could be fitted to the contribution of the two peaks centered at 102.0 and 102.5 eV, which corresponded to Si$^{2+}$ and Si$^{3+}$, respectively [47]. According to the fitted peak areas of **Figure 2.7(e)**, the proportion of these valence states of Si$^{2+}$ and Si$^{3+}$ were estimated to be 19.9% and 80.1%, respectively. The average valence state of Si was 2.8, calculated based on the deconvoluted peak area of two components, which corresponded to the chemical formula of SiO$_{1.4}$. Moreover, no peaks centered at around 99 eV were detected, it can be assured that there was no elemental silicon in the SiO$_x$@C particles [48]. The results indicated that there were different chemical states of Si in SiO$_x$, which was probably caused by the carbothermal reduction occurring between silica and carbon during the heating process (SiO$_2$ + C → SiO$_x$ + CO$_{2-x}$).

Raman spectroscopy was further applied to analyze the chemical bonding in the composites due to its high sensitivity to the electronic structures. As shown in **Figure 2.7(f)**, two obvious characteristic peaks at approximately 1362 and 1589 cm$^{-1}$ in the spectrum were clearly observed, which correspond to the typical Raman modes of the D band and G band of carbon refer to disordered *sp$^3$* and *sp$^2$*-bonded carbon atoms, respectively [49]. The results demonstrate that the APF shell was successfully transformed into a conductive carbon layer through the high temperature treatment. The integral intensity ratio of the D peak (red line) and G peak (green line) (I$_D$/I$_G$) was derived from the fitting method of separate Gaussian curves. A Gaussian function was used to fit the peaks with R$^2$ > 0.99. The graphitization degree of carbon materials

can be generally acquired from the $I_D/I_G$ ratio. The $I_D/I_G$ ratio of SiO$_x$@C particles is estimated to be 1.08, which indicates a low degree of graphitization and the presence of disordered carbon [27]. The $I_D/I_G$ ratio will decrease as the carbonization temperature increases. This suggests that increasing the carbonization temperature promotes graphitization [50]. Furthermore, the specific surface area will increase by increasing the carbonization temperature [43]. The structure with more efficient void spaces could provide more efficient ionic transportation pathways and facilitate the diffusion of lithium ion between the electrolyte and SiO$_x$, which would result in the accelerated lithiation process of SiO$_x$ [51]. Therefore, we chose 1200 $^o$C as the temperature for the carbonization process.

**Figure 2.7(g)** shows the nitrogen adsorption-desorption isotherms of SiO$_x$@C particles. The volume of nitrogen adsorbed increases at a relative pressures close to one, which is characteristic for type II isotherms. This observation was indicative of the nonporous material, according to the IUPAC classification [52]. On the basis of the aforementioned adsorption isotherms, it can be obtained a high specific surface area of 139 m$^2$ g$^{-1}$ and the total pore volume of 0.11 cm$^3$ g$^{-1}$.
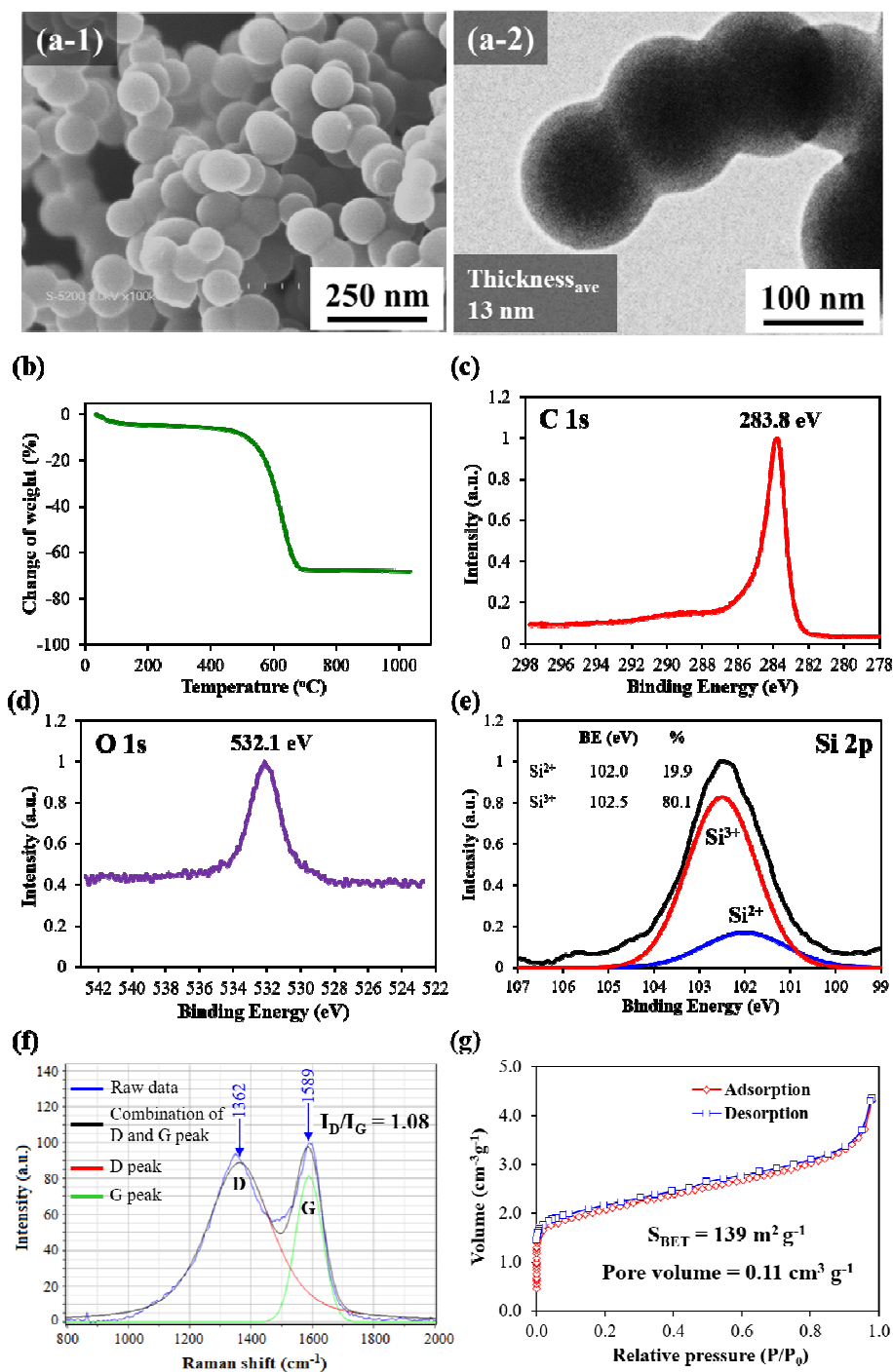
**Figure 2.7.** (a) SEM and TEM images of SiO$_x$@C particles (**C3**); (b) TGA curve for SiO$_x$@C particles in air; (c), (d) and (e) XPS spectra of C 1s, O 1s and Si 2p, respectively; (f) Raman spectrum of SiO$_x$@C particles; and (g) nitrogen adsorption–desorption isotherms of SiO$_x$@C particles.

### *2.3.3. Electrochemical analysis*

The electrochemical activity of $SiO_x@C$ particles in lithium storage was investigated using sample **C3** as the anode material for LIBs.
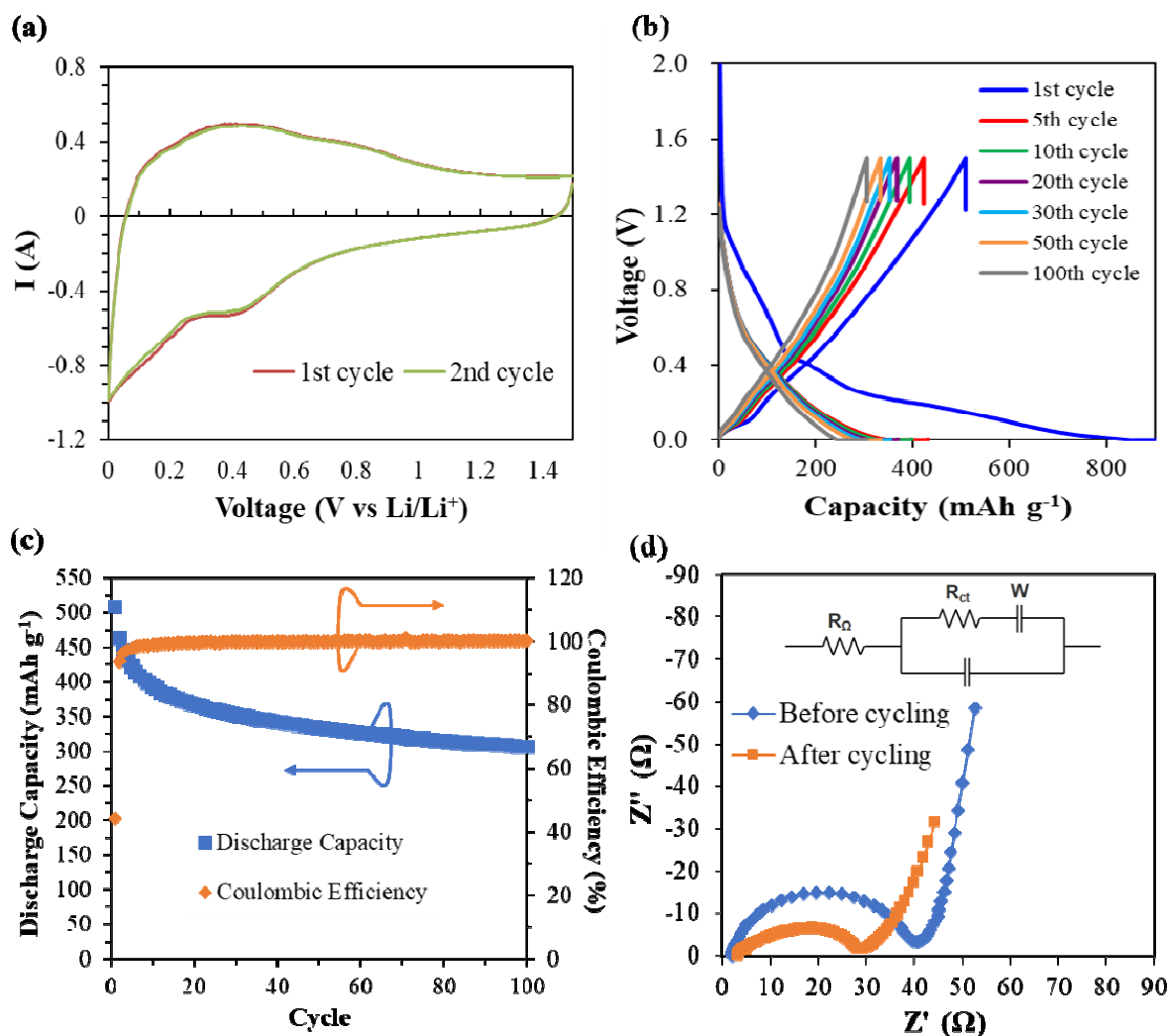


**Figure 2.8.** (a) Cyclic voltammogram of $SiO_x@C$ particles; (b) galvanostatic charge–discharge profile of $SiO_x@C$ particles electrode at 1st, 5th, 10th, 20th, 30th, 50th, and 100th cycles, (c) cyclic performance of $SiO_x@C$ particles as a lithium battery anode, and (d) Nyquist plots of $SiO_x@C$ particles with the equivalent circuit for fitting.

CV was performed in the voltage window from 0.01 to 1.4 V at a scan rate of 0.1 mV s$^{-1}$ to evaluate the reactions that occur during Li-ion insertion–extraction processes. The results are

shown in **Figure 2.8(a)**. The first cycle shows a clear cathodic peak at 0.48 V, which can be attributed to the electrolyte decomposition to form a solid electrolyte interface (SEI) layer and alloying reactions (reactions 1 and 2) [53,54].

$$SiO_x + 2xLi^+ + 2xe^- \rightarrow xLi_2O + Si \quad (1)$$

$$Si + xLi^+ + xe^- \leftrightarrow Li_xSi \qquad (2)$$
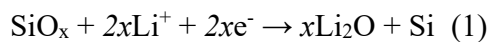
The first cycle shows a broad anodic peak between 0.1 and 1.0 V, which indicates dealloying reaction of Li$_x$Si back to Si. The position of this broad peak is consistent with our previous finding that the dealloying reaction is indicated by an anodic peak at around 0.32 and 0.53 V [28]. The broad anodic peak impeded the identification of the exact peaks position. Therefore, the reversibility of the reactions could not be determined from the ratio of the anodic and cathodic peak current densities. However, the different shapes of the anodic and cathodic curves suggest an irreversible reaction was taking place, which referred to the formation of SEI. The CV curve of the second cycle superimposes that of the first cycle, which indicates that the same irreversible SEI with the same degree of irreversibility also occurred in the second cycle.

**Figure 2.8(b)** displays the galvanostatic discharge (Li extraction)–charge (Li insertion) measurements for the SiO$_x$@C electrode at different cycles at a current density of 100 mA g$^{-1}$ within the voltage range of 0.01 – 2.0 V versus Li/Li$^+$. It can be found that the discharge−charge curves are remarkably consistent with the above CV profiles shown in **Figure 2.8(a)**. The discharge curve for the first cycle shows a steep slope between 0.4 and 1.0 V and a gentle slope at the voltages below 0.4 V. The discharge curves for the fifth and subsequent cycles show a different trend, which indicates that the reversible alloying–dealloying dominates the cycles after the fifth cycle.

In the first cycle, the SiO$_x$@C particles show an initial specific discharge capacity of 509.2 mAh g$^{-1}$ with a low CE of approximately 44.3%. The initial irreversible capacity loss and low CE are mainly caused by the formation of a SEI on the electrode surface and decomposition of the electrolyte during the charge–discharge process [55]. Furthermore, it has been reported that a reversible interplay between SiOC glasses and lithium ions occurs in electrochemical operations [56]. At higher temperature (approximately more than 900 °C), a carbothermic reduction leads to the formation of SiOC glasses, which may contribute to the capacity loss during the first cycle of lithium insertion. Obviously, the discharge capacities in the subsequent

cycles are much smaller than that in the first cycle because the SEI layer formation in the first cycle consumes a large amount of lithium ions, which results in a higher irreversible capacity. The I$_D$/I$_G$ ratio in the Raman spectrum in **Figure 2.7(f)** is 1.08, which indicates the existence of disordered *sp³* carbon structure. The functional groups on the surface of the *sp³* carbon (*e.g.* phenol, carboxyl, and carboxylic anhydride groups) possibly resulted in the lowered capacity by performing irreversible reactions during the SEI formation [57].

As an important properties of LIBs, the long-term cycling stability and the corresponding CE of the SiO$_x$ anode were tested for 100 cycles. As presented in **Figure 2.8(c)**, SiO$_x$ had a discharge capacity of 509.2 mAh g$^{-1}$ in the first cycle, but only 393.9 mAh g$^{-1}$ remained after the tenth cycle with the CE reached 99.1%. Additionally, it is worth mentioning that the CE increased rapidly from 44.3% to 93.5% in the second cycle and still maintained at about 99% in the following cycles. This indicates that a stable SEI layer was formed on the electrode surface as the cycle number increased. The capacity retention was approximately 80% after 100 cycles. The morphological and structural change of SiO$_x$@C electrodes before and after 100 cycles were observed by SEM (**Figure 2.9**). As seen in **Figure 2.9(b-1)**, after cycling, a uniform SEI layer was formed on the surface of the SiO$_x$@C electrode and the surface morphology changed compared with the sample before cycling test as shown in **Figure 2.9(a-1)**. Some consecutive long cracks presence on the surface of SiO$_x$@C electrode were observed from the SEM results (**Figure 2.9(b-2)**), which might have been caused by the volume expansion of SiO$_x$ particles. In this study, the core–shell structure should enable an optimum contact with the carbon matrix to decrease the volume expansion but the carbon layer was insufficiently coated SiO$_x$. However, the electrochemical performance of SiO$_x$@C particles was significantly better than that achieved in our previous research (SiO$_x$ on carbon) [28]. This result indicated the effect of core−shell structure on the performance of LIBs. Therefore, a future optimization is necessary to improve the capacity retention.

The carbon coating layer not only alleviates volume expansion during the charge–discharge process but also provides a backbone for electron transfer and channels for ionic diffusion, while protecting the electrode active material from direct contact with the electrolyte [58]. Therefore, the electronic conductivity and ionic diffusion are two parameters to be clarified using EIS [59]. The resulting Nyquist plots for the electrode materials were recorded at room

temperature before cycling and after 100 cycles (in the delithiated state) and compared. The impedance spectra represent a combination of a semicircle in the moderate-frequency region and a straight line in the low-frequency region. The depressed semicircle in the moderate-frequency region is attributed to the charge transfer process. The charge transfer resistance (R$_{ct}$) of an electrode material can be approximately determined from the diameter of the semicircle on the Z$_{re}$ axis of a Nyquist plot. The straight line in the low-frequency region implies a typical Warburg behavior, which corresponds to solid-state diffusion of lithium ions into the bulk of the electrode material. The high-frequency region represents electronic conductivity, where the film resistance (R$_\Omega$) is indicated by the impedance at the beginning of the first semicircle. **Figure 2.8(d)** shows the Nyquist plot and the equivalent circuit model used, from which the key kinetic parameters are obtained by simulation. The fitted impedance parameters, that is, the equivalent series resistance of electrons within the electrode structure (R$_\Omega$) and charge transfer resistance between the electrolyte interface and electrode (R$_{ct}$), are listed in **Table 2.2**.

For the SiO$_x$@C particles, the value of R$_\Omega$ increased after 100 cycles because of the changes in the carbon structure as a result of Li$^+$ insertion–extraction. However, after 100 cycles, the diameters of the semicircles for SiO$_x$@C particles became remarkably smaller than those before cycling. This indicates that the value of R$_{ct}$ between the electrolyte and active materials in the former is far less than that in the latter, which contributes to a smaller barrier to perform alloying–dealloying reactions of SiO$_x$@C. The fitted data in **Table 2.2** shown that the R$_{ct}$ of SiO$_x$@C particles was 39.5 Ω before cycling, and as the cycle number was increased, dropped down to 22.2 Ω after 100 cycles.

The overall electrochemical results illustrate that the electrode materials were fully accelerated by the lithiation process in the charge–discharge cycles, which led to enhanced lithium ions diffusion kinetics contributed by the formed Li$_2$O during the electrochemical reaction between SiO$_x$ and lithium ions, as well as the slow permeation of the electrolyte into the core−shell structure. Furthermore, the significantly improved electrochemical performance achieved in this work compared with that reported in our previous paper [28] can be explained by the structure of the material. The SiO$_x$@C particles with core−shell structure guarantee an optimum contact with the carbon matrix and the round shape of the carbon shell is highly resilient toward stress. These will contribute to improving the conductivity of SiO$_x$ and exerting

the function of carbon. Therefore, the SiO$_x$@C electrode has a spherical morphology and good electrochemical properties in the cycling process and is a promising anode material for LIBs.
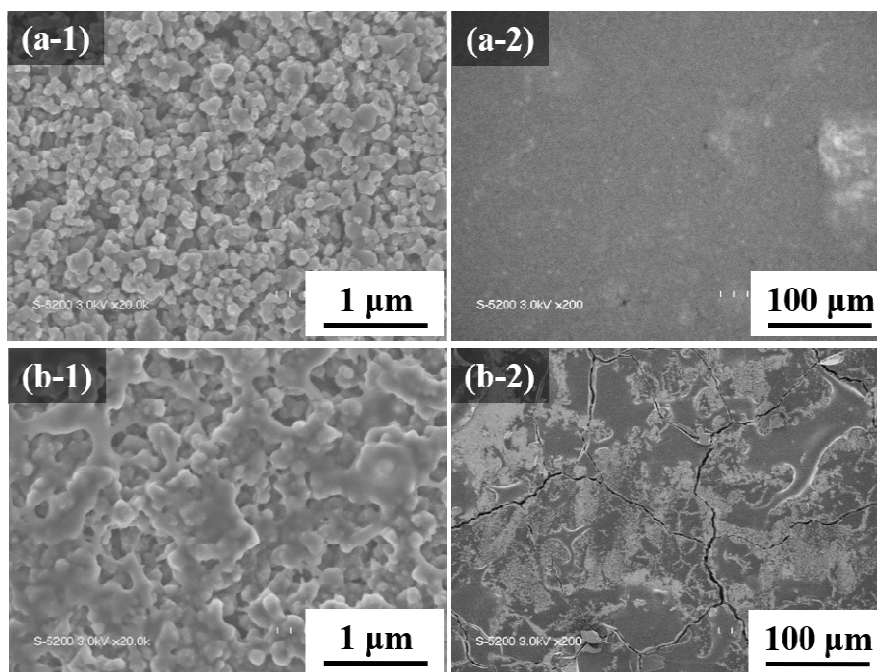


**Figure 2.9.** SEM images of SiO$_x$@C electrodes (a) before cycling and (b) after 100 cycles.

**Table 2.2.** Equivalent circuit parameters for SiO$_x$@C obtained from fitting experimental impedance spectra.

| Sample | | R$_\Omega$ ($\Omega$) | R$_{ct}$ ($\Omega$) |
|---|---|---|---|
| **SiO$_x$@C** | 0$^{th}$ cycle | 2.51 | 39.5 |
| | 100$^{th}$ cycle | 6.80 | 22.2 |

## 2.4. Conclusions

In summary, we have successfully synthesized SiO$_x$@C core−shell particles through a sol-gel method followed by a carbonization process, using TMOS instead of the traditionally used TEOS. The obtained core−shell particles had structural integrity and spherical morphology, which makes TMOS as an excellent silica precursor and renders this approach attractive for future applications. In addition, the developed synthetic route has many prominent advantages: mild condition, easy to control, low cost, and high production. When used as the anode material for LIBs, the obtained SiO$_x$@C particles delivered a reversible capacity of 509.2 mAh g$^{-1}$ at 100 mA g$^{-1}$ and the capacity retention was approximately 80% after 100 cycles. The electrochemical performance of SiO$_x$@C particles was significantly better than those achieved in our previously reported studies due to the morphology and structure of the material. These results suggest that the use of TMOS and our developed synthetic strategy will open up new opportunities for the development of functional SiO$_x$@C particles with core−shell structure for diverse applications.

## 2.5. References

[1]   J.F. Li, Y.J. Zhang, S.Y. Ding, R. Panneerselvam, Z.Q. Tian, Core−shell nanoparticle-enhanced Raman spectroscopy, Chem. Rev. 117 (2017) 5002–5069.

[2]   T. Ogi, A.B.D. Nandiyanto, K. Okuyama, Nanostructuring strategies in functional fine-particle synthesis towards resource and energy saving applications, Adv. Powder Technol. 25 (2014) 3–17.

[3]   A.M. Rahmatika, Y. Goi, T. Kitamura, W. Widiyastuti, T. Ogi, TEMPO-oxidized cellulose nanofiber (TOCN) decorated macroporous silica particles: Synthesis, characterization, and their application in protein adsorption, Mater. Sci. Eng. C 105 (2019) 110033.

[4]   A.M. Rahmatika, W. Yuan, A.F. Arif, R. Balgis, K. Miyajima, G.M. Anilkumar, K. Okuyama, T. Ogi, Energy-efficient templating method for the industrial production of porous carbon particles by a spray pyrolysis process using poly(methyl methacrylate), Ind. Eng. Chem. Res. 57 (2018) 11335–11341.

[5]     R.G. Chaudhuri, S. Paria, Core/shell nanoparticles: Classes, properties, synthesis mechanisms, characterization, and applications, Chem. Rev. 112 (2012) 2373–2433.

[6]     M.B. Gawande, A. Goswami, T. Asefa, H. Guo, A. V. Biradar, D.L. Peng, R. Zboril, R.S. Varma, Core-shell nanoparticles: synthesis and applications in catalysis and electrocatalysis, Chem. Soc. Rev. 44 (2015) 7540–7590.

[7]     R. Balgis, W. Widiyastuti, T. Ogi, K. Okuyama, Enhanced electrocatalytic activity of Pt/3D hierarchical bimodal macroporous carbon nanospheres, ACS Appl. Mater. Interfaces 9 (2017) 23792–23799.

[8]     A.F. Arif, R. Balgis, T. Ogi, T. Mori, K. Okuyama, Experimental and theoretical approach to evaluation of nanostructured carbon particles derived from phenolic resin via spray pyrolysis, Chem. Eng. J. 271 (2015) 79–86.

[9]     C. Homann, L. Krukewitt, F. Frenzel, B. Grauel, C. Würth, U. Resch-Genger, M. Haase, NaYF$_4$:Yb,Er/NaYF$_4$ core/shell nanocrystals with high upconversion luminescence quantum yield, Angew. Chemie - Int. Ed. 57 (2018) 8765–8769.

[10]    K.J. Robinson, G.T. Huynh, B.P. Kouskousis, N.L. Fletcher, Z.H. Houston, K.J. Thurecht, S.R. Corrie, Modified organosilica core-shell nanoparticles for stable pH sensing in biological solutions, ACS Sensors 3 (2018) 967–975.

[11]    H. Matsushita, S. Mizukami, F. Sugihara, Y. Nakanishi, Y. Yoshioka, K. Kikuchi, Multifunctional core-shell silica nanoparticles for highly sensitive $^{19}$F magnetic resonance imaging, Angew. Chemie - Int. Ed. 53 (2014) 1008–1011.

[12]    S.H. Joo, J.Y. Park, C.K. Tsung, Y. Yamada, P. Yang, G.A. Somorjai, Thermally stable Pt/mesoporous silica core-shell nanocatalysts for high-temperature reactions, Nat. Mater. 8 (2009) 126–131.

[13]    H. Zhu, J. Zhang, R. Yanzhang, M. Du, Q. Wang, G. Gao, J. Wu, G. Wu, M. Zhang, B. Liu, J. Yao, X. Zhang, When cubic cobalt sulfide meets layered molybdenum disulfide: A core-shell system toward synergetic electrocatalytic water splitting, Adv. Mater. 27 (2015) 4752–4759.

[14]  Y. Fang, G. Zheng, J. Yang, H. Tang, Y. Zhang, B. Kong, Y. Lv, C. Xu, A.M. Asiri, J. Zi, F. Zhang, D. Zhao, Dual-pore mesoporous carbon@silica composite core-shell nanospheres for multidrug delivery, Angew. Chemie - Int. Ed. 53 (2014) 5366–5370.

[15]  G.F. Chen, Y.Z. Su, P.Y. Kuang, Z.Q. Liu, D.Y. Chen, X. Wu, N. Li, S.Z. Qiao, Polypyrrole shell@3D-Ni metal core structured electrodes for high-performance supercapacitors, Chem. Eur. J. 21 (2015) 4614–4621.

[16]  H. Jiang, J. Ma, C. Li, Mesoporous carbon incorporated metal oxide nanomaterials as supercapacitor electrodes, Adv. Mater. 24 (2012) 4197–4202.

[17]  J. Wang, H. Zhao, J. He, C. Wang, J. Wang, Nano-sized SiO$_x$/C composite anode for lithium ion batteries, J. Power Sources 196 (2011) 4811–4815.

[18]  J.B. Goodenough, K.S. Park, The Li-ion rechargeable battery: A perspective, J. Am. Chem. Soc. 135 (2013) 1167–1176.

[19]  J. Xu, H.R. Thomas, R.W. Francis, K.R. Lum, J. Wang, B. Liang, A review of processes and technologies for the recycling of lithium-ion secondary batteries, J. Power Sources 177 (2008) 512–527.

[20]  Y. Tang, Y. Zhang, X. Rui, D. Qi, Y. Luo, W.R. Leow, S. Chen, J. Guo, J. Wei, W. Li, J. Deng, Y. Lai, B. Ma, X. Chen, Conductive inks based on a lithium titanate nanotube gel for high-rate lithium-ion batteries with customized configuration, Adv. Mater. 28 (2016) 1567–1576.

[21]  Q. Xu, J.K. Sun, Y.X. Yin, Y.G. Guo, Facile synthesis of blocky SiO$_x$/C with graphite-like structure for high-performance lithium-ion battery anodes, Adv. Funct. Mater. 28 (2018) 1705235.

[22]  Q. Yu, P. Ge, Z. Liu, M. Xu, W. Yang, L. Zhou, D. Zhao, L. Mai, Ultrafine SiO$_x$/C nanospheres and their pomegranate-like assemblies for high-performance lithium storage, J. Mater. Chem. A 6 (2018) 14903–14909.

[23]  Y. Ren, M. Li, Facile synthesis of SiO$_x$@C composite nanorods as anodes for lithium ion

batteries with excellent electrochemical performance, J. Power Sources 306 (2016) 459–466.

[24] M. Han, J. Yu, Subnanoscopically and homogeneously dispersed SiO$_x$/C composite spheres for high-performance lithium ion battery anodes, J. Power Sources 414 (2019) 435–443.

[25] L. Sun, T. Su, L. Xu, M. Liu, H. Bin Du, Two-dimensional ultra-thin SiO$_x$ (0 < x < 2) nanosheets with long-term cycling stability as lithium ion battery anodes, Chem. Commun. 52 (2016) 4341–4344.

[26] J. Yang, Y. Takeda, N. Imanishi, C. Capiglia, J.Y. Xie, O. Yamamoto, SiO$_x$-based anodes for secondary lithium batteries, Solid State Ionics 152–153 (2002) 125–129.

[27] J. Cui, Y. Cui, S. Li, H. Sun, Z. Wen, J. Sun, Microsized porous SiO$_x$@C composites synthesized through aluminothermic reduction from rice husks and used as anode for lithium-ion batteries, ACS Appl. Mater. Interfaces 8 (2016) 30239–30247.

[28] T. Izawa, A.F. Arif, S. Taniguchi, K. Kamikubo, H. Iwasaki, T. Ogi, Improving the performance of Li-ion battery carbon anodes by *in-situ* immobilization of SiO$_x$ nanoparticles, Mater. Res. Bull. 112 (2019) 16–21.

[29] M. Li, Y. Zeng, Y. Ren, C. Zeng, J. Gu, X. Feng, H. He, Fabrication and lithium storage performance of sugar apple-shaped SiO$_x$@C nanocomposite spheres, J. Power Sources 288 (2015) 53–61.

[30] C.J. Brinker, Hydrolysis and condensation of silicates, J. Non-Crystalline Solid 100 (1988) 31–50.

[31] L. Ernawati, T. Ogi, R. Balgis, K. Okuyama, M. Stucki, S.C. Hess, W.J. Stark, Hollow silica as an optically transparent and thermally insulating polymer additive, Langmuir 32 (2016) 338–345.

[32] J. Zhao, W. Niu, L. Zhang, H. Cai, M. Han, Y. Yuan, S. Majeed, S. Anjum, G. Xu, A template-free and surfactant-free method for high-yield synthesis of highly monodisperse

3-aminophenol-formaldehyde resin and carbon nano/microspheres, Macromolecules 46 (2013) 140–145.

[33]  L. Ernawati, R. Balgis, T. Ogi, K. Okuyama, Tunable synthesis of mesoporous silica particles with unique radially oriented pore structures from tetramethyl orthosilicate via oil-water emulsion process, Langmuir 33 (2017) 783–790.

[34]  A.F. Arif, Y. Kobayashi, E.M. Schneider, S.C. Hess, R. Balgis, T. Izawa, H. Iwasaki, S. Taniguchi, T. Ogi, K. Okuyama, W.J. Stark, Selective low-energy carbon dioxide adsorption using monodisperse nitrogen-rich hollow carbon submicron spheres, Langmuir 34 (2018) 30–35.

[35]  A.F. Arif, S. Taniguchi, T. Izawa, K. Kamikubo, H. Iwasaki, T. Ogi, Microwave-assisted synthesis of C/SiO$_2$ composite with controllable silica nanoparticle size, ACS Omega 3 (2018) 4063–4069.

[36]  B. Xi, Y.C. Tan, H.C. Zeng, A general synthetic approach for integrated nanocatalysts of metal-silica@ZIFs, Chem. Mater. 28 (2016) 326–336.

[37]  R. Kar, S. Pal, Effect of solvents having different dielectric constants on reactivity: A conceptual DFT approach, Int. J. Quantum Chem. 110 (2010) 1642–1647.

[38]  Y. Bao, T. Wang, Q. Kang, C. Shi, J. Ma, Micelle-template synthesis of hollow silica spheres for improving water vapor permeability of waterborne polyurethane membrane, Sci. Rep. 7 (2017) 46638.

[39]  F.A. Permatasari, H. Fukazawa, T. Ogi, F. Iskandar, K. Okuyama, Design of pyrrolic-N-rich carbon dots with absorption in the first near-infrared window for photothermal therapy, ACS Appl. Nano Mater. 1 (2018) 2368–2375.

[40]  J.C. Song, Z.Y. Lu, Z.Y. Sun, A facile method of synthesizing uniform resin colloidal and microporous carbon spheres with high nitrogen content, J. Colloid Interface Sci. 431 (2014) 132–138.

[41]  H. Li, Y. Hou, L. Li, Synthesis of the SiO$_2$@C composites with high-performance

electromagnetic wave absorption, Powder Technol. 343 (2019) 129–136.

[42]    J.M. Berouier, L. Teyssedre, C. Jacouiod, Synthesis of transparent mesoporous and mesostructured thin silica films, J. Sol-Gel Sci. Technol. 13 (1998) 739–742.

[43]    A.F. Arif, Y. Kobayashi, R. Balgis, T. Ogi, H. Iwasaki, K. Okuyama, Rapid microwave-assisted synthesis of nitrogen-functionalized hollow carbon spheres with high monodispersity, Carbon 107 (2016) 11–19.

[44]    D. Jia, K. Wang, J. Huang, Filter paper derived nanofibrous silica–carbon composite as anodic material with enhanced lithium storage performance, Chem. Eng. J. 317 (2017) 673–686.

[45]    L. Shi, C. Pang, S. Chen, M. Wang, K. Wang, Z. Tan, P. Gao, J. Ren, Y. Huang, H. Peng, Z. Liu, Vertical graphene growth on SiO microparticles for stable lithium ion battery anodes, Nano Lett. 17 (2017) 3681–3687.

[46]    H. Nara, T. Yokoshima, T. Momma, T. Osaka, Highly durable SiOC composite anode prepared by electrodeposition for lithium secondary batteries, Energy Environ. Sci. 5 (2012) 6500–6505.

[47]    P. Lv, H. Zhao, C. Gao, T. Zhang, X. Liu, Highly efficient and scalable synthesis of $SiO_x/C$ composite with core-shell nanostructure as high-performance anode material for lithium ion batteries, Electrochim. Acta. 152 (2015) 345–351.

[48]    Y. Hwa, C.M. Park, H.J. Sohn, Modified SiO as a high performance anode for Li-ion batteries, J. Power Sources 222 (2013) 129–134.

[49]    J. Cui, F. Cheng, J. Lin, J. Yang, K. Jiang, Z. Wen, J. Sun, High surface area $C/SiO_2$ composites from rice husks as a high-performance anode for lithium ion batteries, Powder Technol. 311 (2017) 1–8.

[50]    P. Lv, H. Zhao, C. Gao, Z. Du, J. Wang, X. Liu, $SiO_x$-C dual-phase glass for lithium ion battery anode with high capacity and stable cycling performance, J. Power Sources 274 (2015) 542–550.

[51]   Z. Gu, X. Xia, C. Liu, X. Hu, Y. Chen, Z. Wang, H. Liu, Yolk structure of porous $C/SiO_2/C$ composites as anode for lithium-ion batteries with quickly activated $SiO_2$, J. Alloys Compd. 757 (2018) 265–272.

[52]   K.S.W. Sing, D.H. Everett, R.A.W. Haul, L. Moscou, R.A. Pierotti, J. Rouquerol, T. Siemieniewska, Reporting physisorption data for gas/solid systems with special reference to the determination of surface area and porosity, Pure Appl. Chem. 57 (1985) 603–619.

[53]   C.K. Back, T.J. Kim, N.S. Choi, Activated natural porous silicate for a highly promising $SiO_x$ nanostructure finely impregnated with carbon nanofibers as a high performance anode material for lithium-ion batteries, J. Mater. Chem. A 2 (2014) 13648–13654.

[54]   B. Guo, J. Shu, Z. Wang, H. Yang, L. Shi, Y. Liu, L. Chen, Electrochemical reduction of nano-$SiO_2$ in hard carbon as anode material for lithium ion batteries, Electrochem. Commun. 10 (2008) 1876–1878.

[55]   F. Zheng, M. He, Y. Yang, Q. Chen, Nano electrochemical reactors of $Fe_2O_3$ nanoparticles embedded in shells of nitrogen-doped hollow carbon spheres as high-performance anodes for lithium-ion batteries, Nanoscale 7 (2015) 3410–3417.

[56]   H. Fukui, H. Ohsuka, T. Hino, K. Kanamura, A Si-O-C composite anode: High capability and proposed mechanism of lithium storage associated with microstructural characteristics, ACS Appl. Mater. Interfaces 2 (2010) 999–1008.

[57]   N. Li, X. Ma, Q. Zha, K. Kim, Y. Chen, C. Song, Maximizing the number of oxygen-containing functional groups on activated carbon by using ammonium persulfate and improving the temperature-programmed desorption characterization of carbon surface chemistry, Carbon 49 (2011) 5002–5013.

[58]   H. Li, H. Zhou, Enhancing the performances of Li-ion batteries by carbon-coating: Present and future, Chem. Commun. 48 (2012) 1201–1217.

[59]   C.J. Wen, C. Ho, B.A. Boukamp, I.D. Raistrick, W. Weppner, R.A. Huggins, Use of electrochemical methods to determine chemical-diffusion coefficients in alloys: application to 'LiAl,' Int. Met. Rev. 26 (1981) 253–268.

# Chapter 3

# Controllable Synthesis of Spherical Carbon Particles Transition from Dense to Hollow Structure Derived from Kraft Lignin

## 3.1. Introduction

In recent years, the rational design and synthesis of nanostructured particulate materials in favorable morphologies have attracted tremendous interests. Such syntheses represent fundamental challenges in the fields of colloids and surface science and could also provide a means to progress towards renewable energy solutions for the construction of sustainable societies [1–6]. From an engineering point of view, the spherical particles offer greater advantages over than that of other shapes because (i) they have no sharp edges and so are less prone to breaking or damaging other materials during processing; (ii) the regular shape and size of them allows the efficient ordering of objects in closely packed states, especially in the case that necks and pores are present; and (iii) they have the best fluidity [7,8]. In particular, spherical carbon particles have received a great deal of interest due to their outstanding physical properties, such as good fluidity, smooth surfaces, superior packing, and harmless [9,10]. These properties make carbon spheres good candidates for a wide range of potential applications, including catalyst supports [11], adsorbents [12], chemical protective clothing [13], blood purification [14], and energy storage [15,16]. Therefore, numerous research efforts have been devoted to developing advanced strategies for the preparation of spherical carbon, both with regard to the selection of synthesis methods and carbon sources. However, from the long-term perspective of sustainable development, the simple, easy fabrication of spherical carbon particles with uniform particle sizes and good dispersity remains a grand challenge.

Lignocellulosic biomass, primarily consists of three components (*e.g.* cellulose, hemicellulose, and lignin), has emerged as an ideal precursor for the production of spherical carbon materials because of its favorable renewability, reproducible, readily availability, cost-

effective, and environmentally benign [17,18]. In particular, lignin is of interest because it is a byproduct of the conversion of biomass to biofuel and also of paper making, such that several million pounds are generated annually [19]. Furthermore, as the second most abundant phenolic polymer in nature (surpassed only by cellulose) and the first most abundant aromatic polymer, lignin can be considered as a potential sustainable source for the preparation of spherical carbon. This material offers numerous unique properties, such as a high carbon content (above 60 wt%), good thermal stability, abundant aromatic rings, extensively crosslinked polyphenolic structure, and low feedstock cost [20,21]. There are several methods for preparing colloidal carbon particles based on lignin or lignin derivatives, including hydrothermal/solvothermal [22], self-assembly [23], precipitation [24], hard-template/soft-template [25], as well as the direct pyrolysis of spherical precursors [26]. However, all these approaches still suffer from several drawbacks, such as the destruction of the spherical structure during the carbonization process, the necessity for high-pressure equipment, high energy consumption, costly templates and low yields, as well as time-consuming and complicated manufacturing processes. These factors therefore limit the development of environmentally friendly, economically sustainable and large-scale practical applications. Addressing these issues will require either reducing the associated costs or simplifying the preparation procedures by decreasing the time- and energy-consuming steps in accordance with green chemistry principles. Compared with the above-mentioned strategies, spray drying technique is the most promising method to control particle morphology and represents a versatile, continuous and rapid process [27,28]. The particles/colloids can be prepared by spray drying on a large scale and tend to show narrow particle size distribution and highly spherical shape, which can be tailored by adjusting the spray parameters [29].

Although lignin has been used as a raw material for the preparation of carbon materials, there have been few reports of the successful production of carbon spheres from lignin-based materials using spray drying [30]. To date, no studies have investigated the formation of well-controlled morphologies or the associated particle formation mechanism. Chen et al. [31] reported the preparation of porous carbon using spray drying and carbonization process, employing lignosulfonate as the carbonaceous precursor and potassium hydroxide (KOH) as the activator. However, following the carbonization process, the resulting particles had wrinkled surfaces, meaning that perfectly spherical structures of the carbon were not obtained. For this

reason, precise design the spherical carbon particles derived from lignin are urgently needed to develop novel strategies. As noted, spray drying has become an established method in several research fields, however, to date, the capabilities of this technique have not been fully exploited and reported yet, especially in examining the formation mechanism of lignin and lignin composites (*e.g.* lignin/KOH composites) and controlling the structure of the finally obtained carbon by adjusting the KOH concentration.

Aiming at the problems mentioned above and using previously reported work as inspiration, the objectives of the present study were (i) to synthesize spherical carbon particles derived from Kraft lignin, (ii) to demonstrate the effects of the KOH concentration on particle morphology and structure, and (iii) to obtain an in-depth understanding of the formation mechanism of lignin/KOH composites during the spray drying from colloids and surface science points of view. In this work, spherical carbon particles were attempted to fabricate using Kraft lignin as the carbon source and solid KOH as the activation agent in the water solution. Compared with lignosulfonate, Kraft lignin has a high purity because it contains lower amounts of sulfur, carbohydrate residues, and inorganic impurities [32]. In addition, from the other reported processes, lignin is first carbonized and then mixed with high amounts of KOH for activation at high temperatures [33,34]. However, in our work, Kraft lignin was initially well dissolved in distilled water together with varying amounts of solid KOH, which is considered beneficial to the activation process, and the spherical shapes were obtained by spray drying this solution. These materials can be readily converted to carbon through a simple carbonization process in a nitrogen atmosphere while maintaining their structural integrity and spherical morphology, which cannot be possessed in the previously reported literature. Furthermore, the distinct advantage of this process is a self-stable system without any addition of template materials or the use of prefabricated spherical precursors, and this efficient technique is suitable for large scale applications. In addition, the well-controlled morphology of carbon transition from dense sphere to hollow sphere structure can be achieved by adjusting the KOH concentration. The use of a cheap, renewable byproduct as the carbon precursor, water as the solvent could lower the production costs of carbon materials and would also render this approach as an environmentally friendly process. The results of this work provide helpful information with

regard to the utilization of biomass materials in commercial applications and in the fields of colloidal and interface science.

## 3.2. Experimental

### 3.2.1. Synthesis of carbon particles derived from Kraft lignin

All chemicals used in this work were of analytical grade and were used as received without further purification. The Kraft lignin serving as the carbon source was obtained from Kuraray Co., Ltd., Japan. In a typical procedure, the preparation of carbon particles involves three steps as shown in **Figure 3.1**. Kraft lignin was initially dissolved in distilled water together with varying amounts of solid KOH (Kanto Chemical Co., Inc., Tokyo, Japan) to form a homogeneous solution that was stirred at room temperature for 30 min. This solution was subsequently transferred into a mini spray-dryer (BÜCHI B-290, Switzerland) and spray-dried through a two-fluid nozzle system at an inlet temperature of 200 $^{\circ}$C. Hot air was used as the carrier gas at a flow rate of 10 L/min and a precursor feed rate of 2.5 mL/min was employed to obtain the spherical lignin/KOH composite particles. These composite particles were then carbonized in a horizontal tube furnace by heating from room temperature to 700 – 900 $^{\circ}$C at 5 $^{\circ}$C/min and then holding at the final temperature for 2 h, all under a continuous flow of nitrogen atmosphere at 1.0 L/min. The carbonized material was naturally cooled down to room temperature and subsequently washed with 10 wt% aqueous hydrochloric acid (HCl) solution (Kanto Chemical Co., Inc., Tokyo, Japan) to completely remove residual KOH as well as any other impurities. The resulting black powder was washed with distilled water and centrifuged several times until the pH of the wash water was neutral. The resulting carbon particles were dried at 105 $^{\circ}$C for 12 h in a vacuum oven. The products were marked as **KLC-X-Y**, where X represents the mass ratio of KOH to lignin (X = 0.17, 0.33, 0.67, 1.00, and 1.33), and Y indicates the carbonization temperature (Y = 700, 800, and 900 $^{\circ}$C). For comparison study, the carbon sample without the addition of KOH denoted as **LC-700** was also prepared through the same procedure as described above at a carbonization temperature of 700 $^{\circ}$C. Details of the sample preparation conditions are summarized in **Table 3.1**.
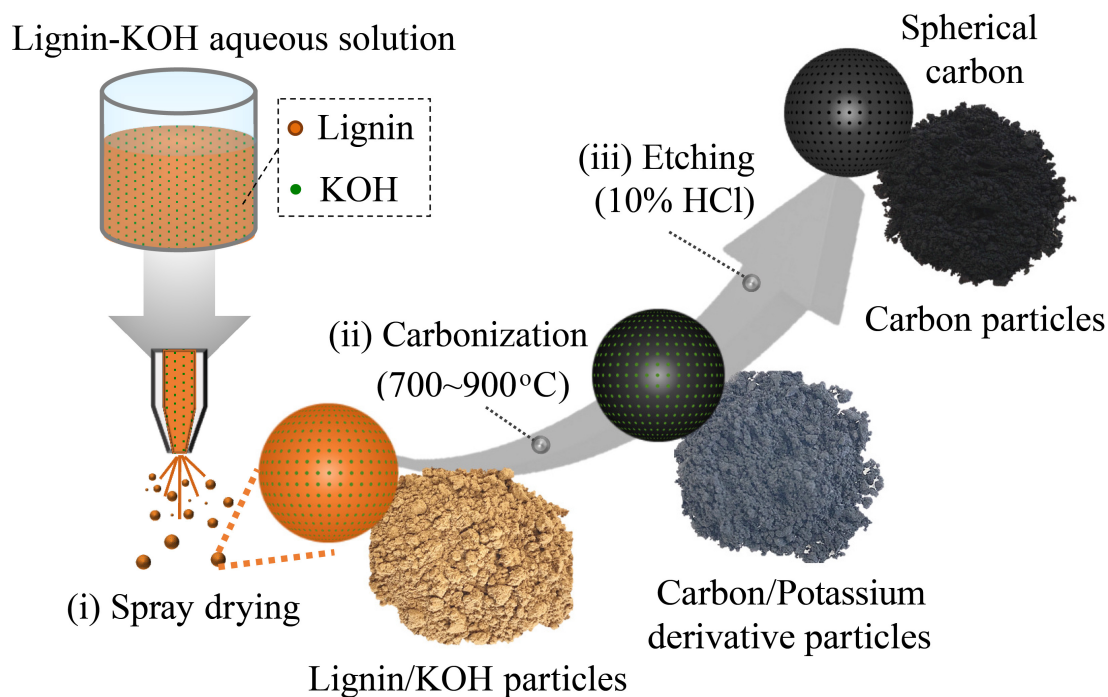
**Figure 3.1.** Schematic of experimental steps for producing spherical and dense carbon particles.

**Table 3.1.** Formulations for the specimens derived from Kraft lignin in this work.

| Sample name | Lignin (g) | KOH (g) | Water (g) | KOH/lignin (-) |
|---|---|---|---|---|
| LC-700 | 1.2 | - | 64 | - |
| KLC-0.17-700 | 1.2 | 0.2 | 64 | 0.17 |
| KLC-0.33-700 | 1.2 | 0.4 | 64 | 0.33 |
| KLC-0.33-800 | 1.2 | 0.4 | 64 | 0.33 |
| KLC-0.33-900 | 1.2 | 0.4 | 64 | 0.33 |
| KLC-0.67-700 | 1.2 | 0.8 | 64 | 0.67 |
| KLC-1.00-700 | 1.2 | 1.2 | 64 | 1.00 |
| KLC-1.33-700 | 1.2 | 1.6 | 64 | 1.33 |

*3.2.2. Characterization*

The morphological and structural features of the resulting carbon particles were examined using field emission scanning electron microscopy (FE-SEM; S-5200, 20 kV, Hitachi High Technologies. Corp., Tokyo, Japan) and transmission electron microscopy (TEM; JEM-2010, 200 kV, JEOL Ltd., Tokyo, Japan). The particle sizes were determined by measuring the diameters of more than 350 randomly selected particles totally from SEM and TEM images. The surface tensions of all solutions were measured at room temperature using a Wilhelmy-type CBVP-Z surface balance with a platinum plate (Kyowa Interface Science Co., Ltd., Japan). The viscosity of each solution was determined at room temperature using an Ostwald viscometer (As One Co., Ltd., Japan). In capillary viscometer, viscosity is measured by noting the time required for a known volume of solution to flow through a small capillary between two marked lines. The liquid densities of all samples were calculated based on masses obtained using a laboratory balance (Mettler Toledo AG204, Japan). All measurements were carried out three times to assess precision. Thermogravimetric analysis (TGA) was performed using a TGA instrument (TGA-50/51 Shimadzu Corp., Kyoto, Japan) under a 10 mL/min flow of nitrogen, applying a heating rate of 5 $^{\circ}$C/min. The crystallographic structures of the prepared particles were investigated using powder X-ray diffraction (XRD; D2 Phaser, 40 kV and 30 mA, Bruker Corp., USA). The disorder and graphitization degree of carbon particles were examined by Raman spectroscopy with a micro-Raman spectrometer employing an excitation laser wavelength of 514.5 nm (Renishaw). The nitrogen adsorption/desorption tests of the carbon particles were carried out using gas adsorption measurement equipment at 77 K (BELSORP-max, MicrotracBEL Corp., Osaka, Japan). All samples were degassed at 300 $^{\circ}$C under high vacuum for 8 h prior to each measurement. The specific surface areas of the specimens were determined using the Brunauer-Emmett-Teller (BET) method, whereas the pore size distributions were calculated according to the Density Functional Theory (DFT) method. The tap density of the carbon particles was measured using the following method. A certain amount of the carbon powder was added into a dry 5 mL cylinder, and then, the measuring cylinder was continuously tapped until the volume of the powder no longer changed. The ratio between the mass and the volume determined the tap density of the carbon particles.

## 3.3. Results and Discussion

### *3.3.1. Synthesis of spherical carbon particles derived from Kraft lignin*

In the initial experiment, comparative experiments were carried out to understand the function of KOH for spherical particle formation. In the absence of KOH, spherical structures were not obtained after carbonization process as confirmed by SEM observations (**Figure 3.2(a-1)**). This image demonstrates that the majority of the particles exhibited a non-spherical morphology with wrinkled surfaces. In contrast, when KOH was present in this reaction system, the particles with highly uniform spherical shapes and smooth outer surfaces were successfully formed as shown in **Figure 3.2(b-1)**. This result indicates that the shape of the particles could be adjusted through controlling the presence of KOH. For confirmation of the particle inner structure, the TEM images are depicted in **Figure 3.2(a-2)** and **3.2(b-2)**. **Figure 3.2(a-2)** shows that the hollow structures were produced in the absence of KOH. On the other hand, the dense particles can clearly be seen in case of using KOH in **Figure 3.2(b-2)**. On the basis of these observations, it is apparent that KOH played a crucial role in the formation of particles with good sphericity and dense structure.
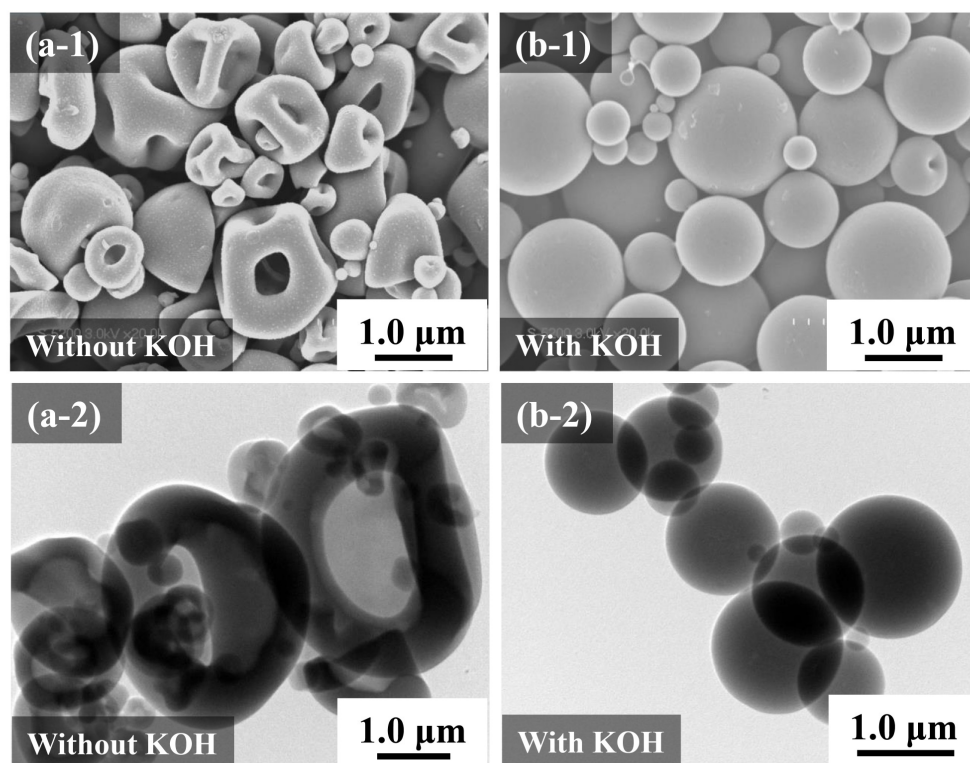
**Figure 3.2.** SEM (up) and TEM (down) images of carbon particles derived from (a) lignin (**LC-700**) and (b) lignin/KOH composites (**KLC-0.33-700**).

We further evaluated the effect of KOH concentration on the overall reaction system by varying the KOH/lignin mass ratio and observing the surface morphologies of the resulting particles as shown in **Figure 3.3**. **Figure 3.3(a-e)** displays the SEM and TEM images along with the corresponding particle size distributions of carbon particles obtained after carbonization with varying proportions of KOH. Overall, the carbon particles derived from spray drying show uniform morphologies with spherical structures in the SEM images (**Figure 3.3(a-1–e-1)**). In addition, the average carbon particle size increased from 0.85 to 1.92 μm as the KOH/lignin mass ratio increased from 0.17 to 1.33. All the spherical carbon particles generated by spray drying also exhibited relatively narrow particle size distributions as presented in **Figure 3.3(a-3–e-3)**. The TEM images indicate an interesting effect in which varying the KOH/lignin mass ratio in the synthesis solution modified the structure of the carbon particles. Specifically, as the KOH/lignin mass ratio increased, the structure of the carbon particles changed from dense to hollow. The dense structure was formed at low KOH/lignin mass ratios of 0.17 and 0.33 as

76

shown in **Figure 3.3(a-2)** and **3.3(b-2)**, respectively. In contrast, the continued addition of more KOH to the reaction system up to a ratio of 1.33 generated hollow spherical structures (**Figure 3.3(c-2–e-2)**). Therefore, the structure of the carbon particles could be easily controlled from dense to hollow structure by adjusting the KOH concentration.
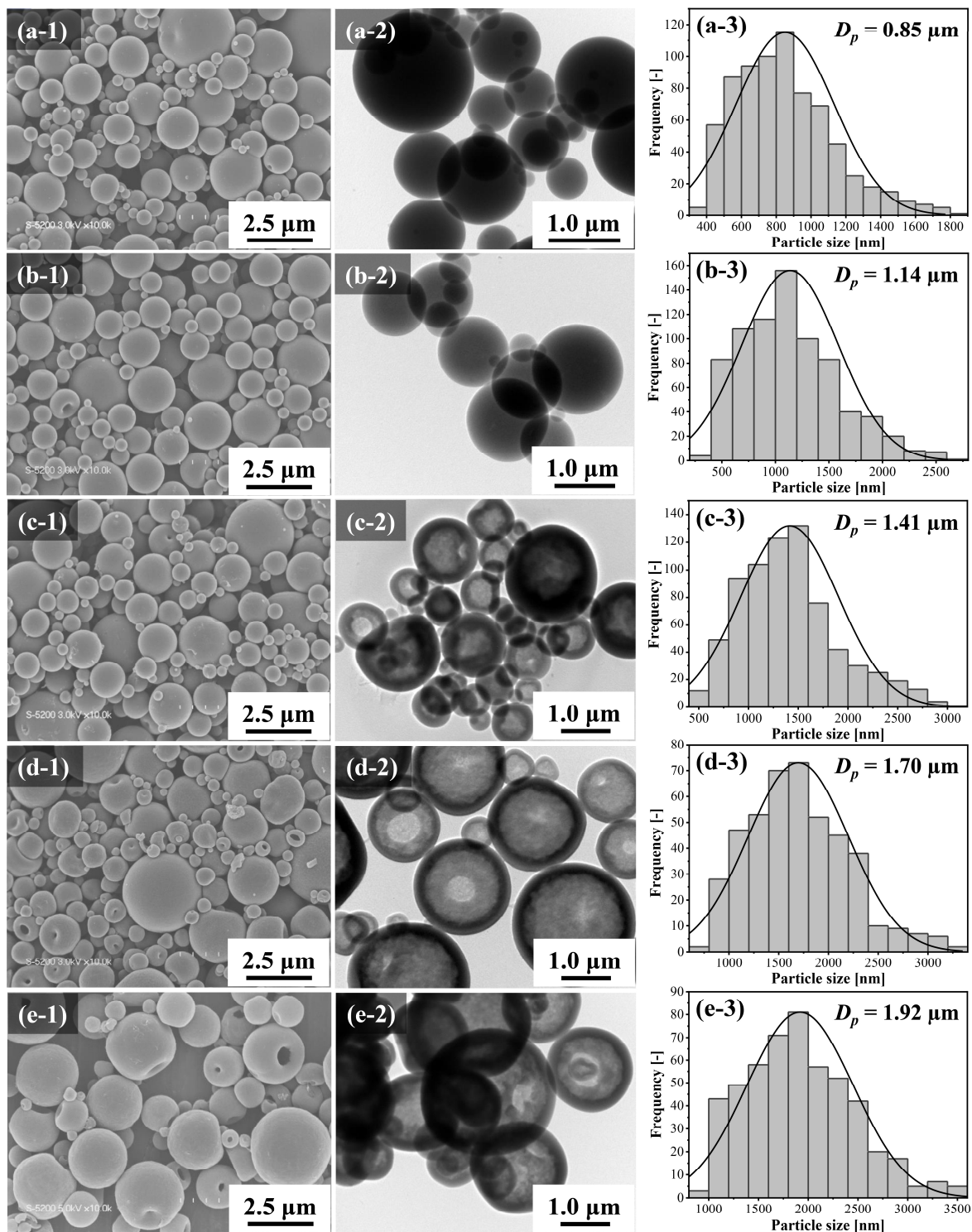
**Figure 3.3.** SEM and TEM images, and corresponding particle size distributions of carbon particles derived from Kraft lignin using different KOH/lignin mass ratios of (a) 0.17 (**KLC-0.17-700**), (b) 0.33 (**KLC-0.33-700**), (c) 0.67 (**KLC-0.67-700**), (d) 1.00 (**KLC-1.00-700**), and (e) 1.33 (**KLC-1.33-700**). $D_p$ indicates the geometric mean particle diameter.

*3.3.2. Proposed mechanism for particle formation*

On the basic of these results achieved from SEM and TEM analyses, a possible particle formation mechanism in spray drying can be discussed as follows. During the spray drying process, the morphology and structure of the particles were primarily determined by the physical properties of the precursor solution and the parameters of the drying operation (*e.g.* the drying temperature, gas flow rate, nozzle configuration, etc.) [35,36]. In this study, we focused on the effects of the precursor solution by varying the KOH concentration while keeping the other conditions of spray drying parameters constant. The addition of KOH changed the physical properties of the precursor (*e.g.* the total solute concentration, density, surface tension, and viscosity), and these changes in turn affected the size and the drying time of the sprayed droplets. Therefore, in the present work, the physical properties (the density, surface tension, and viscosity) of precursor solutions having different KOH concentrations were evaluated. In addition, the droplet diameters $D_d$ were calculated using an estimation formula [37]:

$$D_{droplet} = \frac{0.585}{V_a}\left(\frac{\sigma}{\rho_L}\right)^{0.5} + 53\left(\frac{\eta_L^2}{\sigma\rho_L}\right)^{0.225}\left(\frac{Q_L}{Q_A}\right)^{1.5} \quad (1)$$

where $D_{droplet}$ is the average droplet size (μm), $V_a$ is the liquid jet velocity (m/s), σ is the liquid surface tension (kg/s²), $\rho_L$ is the liquid density (kg/m³), $\eta_L$ is the liquid viscosity (kg/m s), $Q_L$ is the liquid flow rate (m³/s), and $Q_A$ is the carrier gas flow rate (m³/s).

As presented in **Table 3.2**. In the absence of KOH, the $D_d$ value was 7.4 μm and this decreased to 5.7 μm at a KOH/lignin ratio of 0.17. The $D_d$ value was also found to increase with further increases in the KOH concentration.

**Table 3.2.** Parameters used to calculate droplet sizes and the resulting values.

| Sample | KOH/Lignin ratio | $\eta_L$ (kg/m s) | $\sigma$ (kg/s$^2$) | $\rho_L$ (kg/m$^3$) | $Q_L$ (m$^3$/s) | $Q_A$ (m$^3$/s) | $D_{droplet}$ ($\mu$m) |
|---|---|---|---|---|---|---|---|
| **KLC-0.17-700** | 0.17 | $0.866 \times 10^{-3}$ | $42.8 \times 10^{-3}$ | 999.72 | | | 5.7 |
| **KLC-0.33-700** | 0.33 | $0.888 \times 10^{-3}$ | $45.8 \times 10^{-3}$ | 1005.98 | | | 6.1 |
| **KLC-0.67-700** | 0.67 | $0.915 \times 10^{-3}$ | $47.4 \times 10^{-3}$ | 1008.83 | $4.17 \times 10^{-8}$ | $1.67 \times 10^{-4}$ | 6.3 |
| **KLC-1.00-700** | 1.00 | $0.927 \times 10^{-3}$ | $50.4 \times 10^{-3}$ | 1010.58 | | | 6.7 |
| **KLC-1.33-700** | 1.33 | $0.946 \times 10^{-3}$ | $57.7 \times 10^{-3}$ | 1015.74 | | | 7.6 |
| **LC** | - | $0.908 \times 10^{-3}$ | $56.0 \times 10^{-3}$ | 1000.05 | | | 7.4 |

The effect of KOH concentration on the drying times of three samples including lignin without using KOH, lignin with low KOH concentration (KOH/lignin = 0.33) and lignin with high KOH concentration (KOH/lignin = 1.33) was evaluated using TGA and by drying samples in a vacuum oven as shown in **Figure 3.4**. The results of both experiments clearly showed that the sample without using KOH had a shorter drying time and that the sample with a low KOH concentration required longer to dry relative to the specimen with a high KOH concentration. These data indicate that increasing the KOH concentration reduced the drying time. These results are in good agreement with previous reports that a high solute concentration can reduce the drying time [38–40].
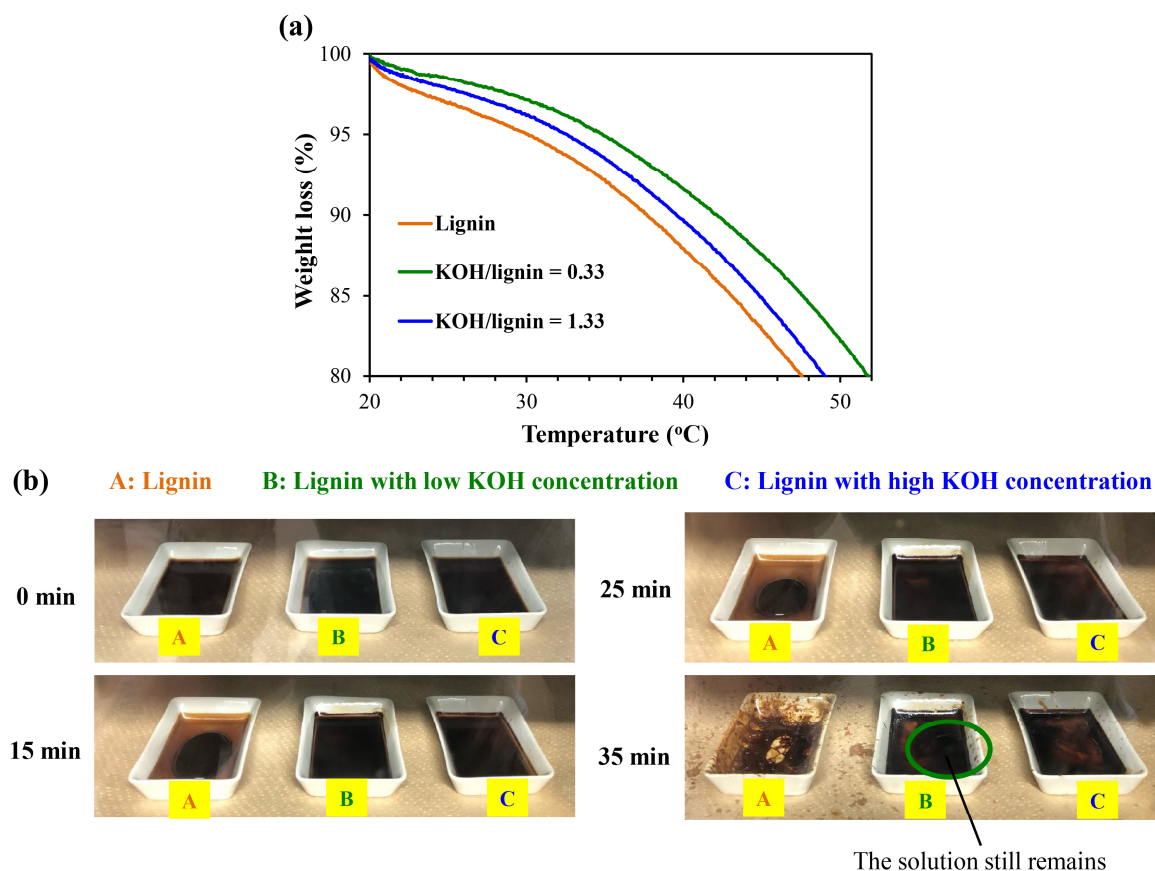
**Figure 3.4.** Effect of KOH concentration on the drying times of three samples including lignin without using KOH, lignin with low KOH concentration (KOH/lignin = 0.33), and lignin with high KOH concentration (KOH/lignin = 1.33), as evaluated by (a) TGA and (b) drying in a vacuum oven.

Based on the above analyses, we proposed the plausible mechanism for the formation of particles at varying KOH concentrations (**Figure 3.5**).

In the absence of KOH (**Figure 3.5(i)**), after the lignin mixture is atomized, droplets of the lignin aqueous solution come into contact with hot air causing the solvent evaporation. Along with solvent evaporation, the droplets shrink and the concentration of lignin in these droplets increases such that a saturated state is generated at the droplet surfaces. As a result, an outer shell of lignin is produced on each particle as the lignin precipitates out of solution, although this shell is thin due to the low amount of lignin relative to the large droplet size. Following this, because

of the external pressure (*e.g.* carrier gas) to the droplet, the droplet becomes unstable and transform from spherical to a convex-concave deformation. Furthermore, as the water inside the droplet diffuses into the shell and additional water from the interior evaporates, the internal pressure of the droplet is decreased, so that the hollow non-spherical (buckled) particles are generated as shown in **Figure 3.5(i)**.

It is interesting to note that the characteristics of the precursor solution were significantly changed by the addition of KOH even at low concentrations (**Table 3.2**). It indicates that there is an interaction between the KOH and lignin in the water medium because the good dissolvability of lignin in aqueous KOH solutions. As a result, the precursor solution with a low level of KOH generated smaller droplets but higher solute concentration during the atomization process compared with the solution not containing KOH. Therefore, the rate of solvent evaporation was sufficiently slower than the rate at which the solutes (that is, the lignin and KOH) diffused throughout the droplets, so that the solutes had adequate time to redistribute within the droplets during the evaporation process. Consequently, a shell of densely packed particles was formed at the droplet surface when the surface concentration of the solute became saturated. As the water completely evaporated, the shell shrank but did not collapse or fragment because the core of the particle was structurally stronger as a result of the presence of more solutes. In this manner, a dense spherical particle was produced as shown in **Figure 3.5(ii)**. This result shows that the presence of KOH successfully maintained the spherical shape due to the higher precipitation throughout the shell formation process, which is correlated with the droplet size.

In the case of a high KOH concentration, a greater quantity of the solutes was present on the droplet surfaces. As discussed above, the drying time also affected the final particle morphology. In comparison with a low KOH concentration, the solute concentration at the droplet interface was significantly higher at the beginning of the evaporation, and the rate of evaporation was much faster than the rate of solute diffusion. Therefore, during the first stage of the spray drying process, water rapidly evaporated from the droplet surface such that the solutes did not have sufficient time to diffuse from the surface to the center of the droplet, and instead accumulated near the droplet drying front. This process increased the concentration of the solute at the surface, which in turn raised the surface viscosity and promoted the formation of a thick

shell. After obtaining a specific minimum thickness, the shell was no longer able to shrink to compensate for the volume reduction associated with evaporation, and so the shape of the particle was maintained due to the higher solvent partial pressure inside the droplet [41]. This led to the formation of a hollow spherical particle (**Figure 3.5(iii)**). The mechanisms summarized in **Figure 3.5** suggest the intriguing possibility that the addition of KOH could be used to produce either dense or hollow spherical particles. Depending on the requirements of different applications, using our strategy will in turn guide the synthesis of spherical carbon materials with desirable architectures and compositions.
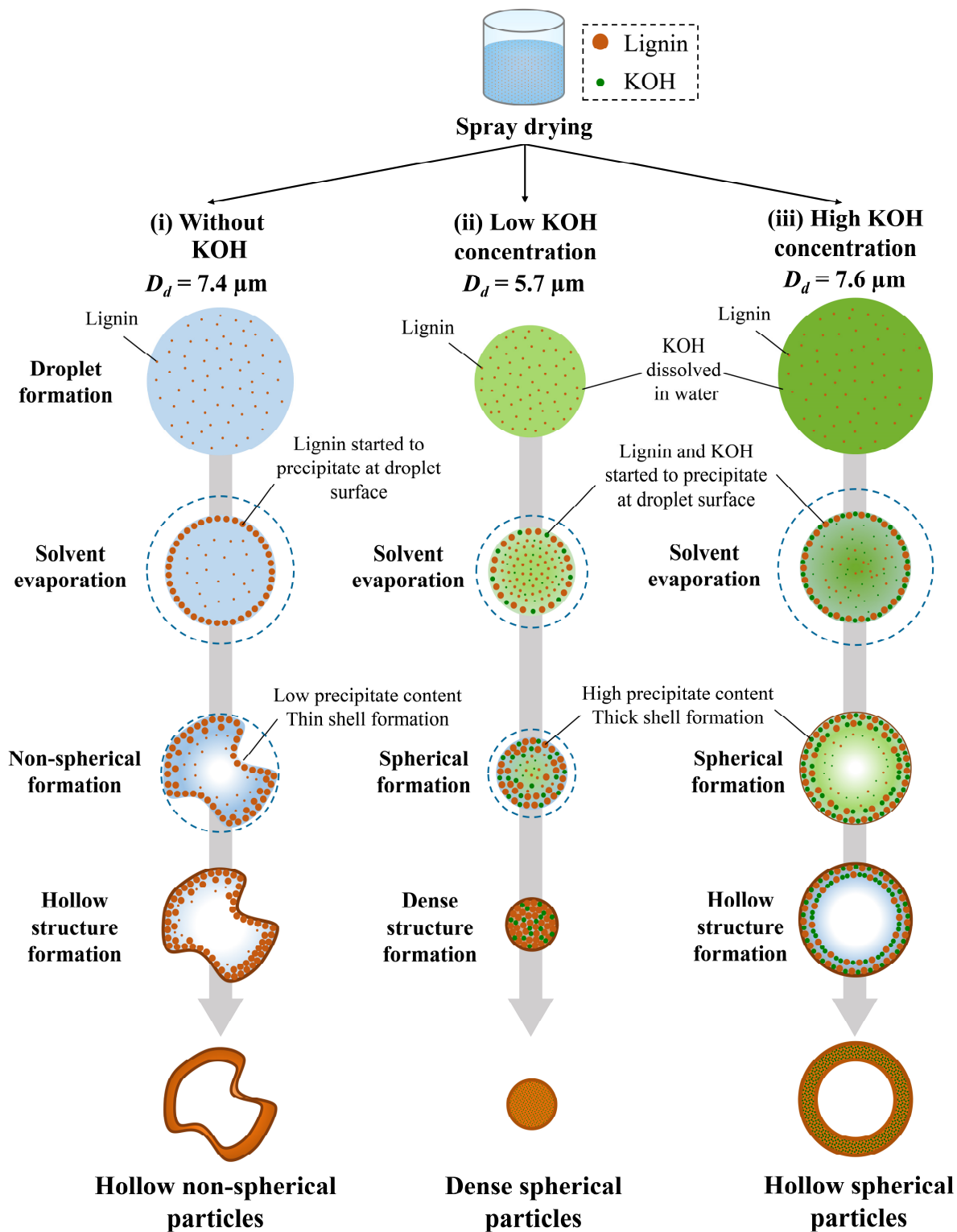
**Figure 3.5.** Schematic diagram for the particle formation mechanisms associated with the spray drying of (i) lignin without KOH, (ii) lignin with a low KOH concentration, and (iii) lignin with a high KOH concentration. $D_d$ indicates the droplet size, as calculated from the solution properties using an empirical equation (1).

### 3.3.3. Material characterizations of carbon particles derived from Kraft lignin

The effect of the carbonization temperature on the final structure of the carbon particles **KLC-0.33** was examined by applying temperatures from 700 to 900 ᵒC. As can be observed in the SEM and TEM images in **Figure 3.6(a-1–c-1)** and **3.6(a-2–c-2)**, respectively, the resulting carbon particles retained their structural integrity and spherical morphology with dense structure, indicating the high quality of our synthesis method. In addition, as the carbonization temperature was increased from 700 to 900 ᵒC, the average carbon particle size decreased from 1.14 to 0.72 μm (**Figure 3.6(a-3–c-3)**) due to the shrinkage during the carbonization process.
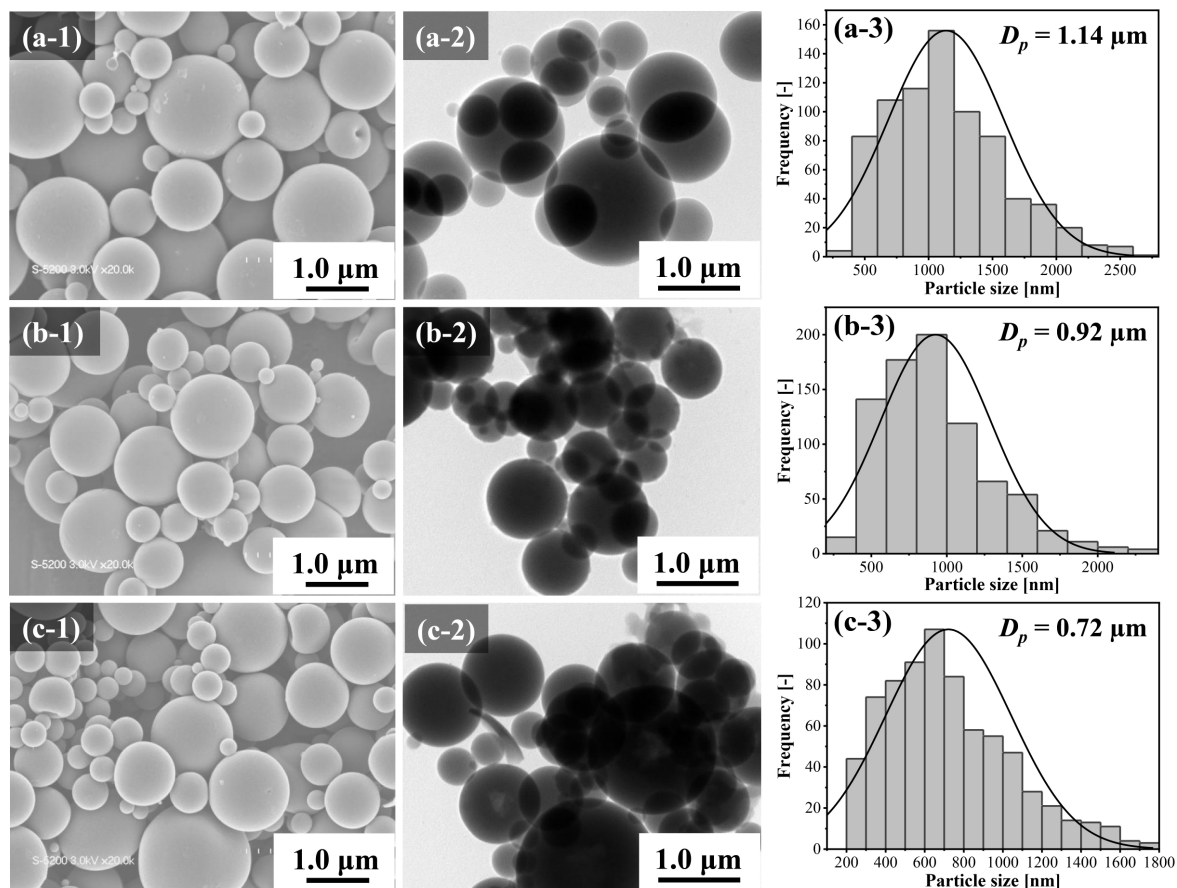
**Figure 3.6.** SEM and TEM images, and corresponding particle size distributions of carbon particles derived from Kraft lignin at carbonization temperatures of (a) 700 °C (**KLC-0.33-700**), (b) 800 °C (**KLC-0.33-800**), and (c) 900 °C (**KLC-0.33-900**). $D_p$ indicates the geometric mean particle diameter.

Various characterization techniques were carried out to obtain a better understanding of the characteristics of carbon particles derived from lignin in this work, using sample **KLC-0.33-700** (having a dense structure) as a typical specimen. Sample **LC-700**, which was obtained under the same conditions except without the addition of KOH, was also assessed for comparison purposes.

**Figure 3.7(a)** presents the XRD diffraction patterns obtained from the **LC-700** and **KLC-0.33-700** samples. Both materials generated two broad diffraction peaks that imply

amorphous structures. The broad peaks centered at approximately $2\theta = 23^{\circ}$ and $44^{\circ}$ can be assigned to the (002) plane of graphitic carbon and the (100) reflection originating from the in-plane structure of amorphous graphitic carbon, respectively [42]. The average interlayer spacing $d_{002}$ value for the **LC-700** and **KLC-0.33-700** calculated using the Bragg equation were about 0.376 and 0.365 nm, respectively, which were apparently larger than the $d_{002}$ value for graphite crystals (0.335 nm) [43]. Generally, amorphous carbon can be divided into soft carbon (graphitic carbon) and hard carbon (non-graphitic carbon) according to the degree of difficulty in graphitization. Based on the above results, the materials produced in this study were typical non-graphitic carbon with highly disordered crystalline structures, which were the proof of hard carbon. In addition, it can be clearly observed that the diffraction intensity of the **KLC-0.33-700** in the low-angle region of its XRD pattern was higher than that in the **LC-700** pattern, indicating the presence of abundant micropores as a result of the activation process [44]. Furthermore, the crystallinity of the prepared carbon particles was also elucidated using Raman spectroscopy, and the results presented in **Figure 3.7(b)**. The spectra data of both the **LC-700** and **KLC-0.33-700** revealed two typical broad bands at around 1356 and 1594 cm$^{-1}$, which are indexed to the D and G bands of carbon, respectively. The vibrational mode of the D band represents the disordered carbon or defective graphitic structures, whereas the G band corresponds to the ordered graphitic crystallites of carbon [15]. The relative intensity ratio between these two bands ($I_D/I_G$) is also calculated since the $I_D/I_G$ could exactly reflect the graphitic degree of a carbonaceous material. The calculated $I_D/I_G$ values for the **LC-700** and **KLC-0.33-700** were determined to be 1.10 and 1.17, respectively, indicating that the latter had a lower degree of graphitization and more defects in its carbon structure. This result can be attributed to the highly porous and disordered structure caused by the activation process, which is in good agreement with the aforementioned results of XRD analyses.

The physical parameters of these as-prepared carbon samples (that is, the **LC-700**, **KLC-0.33-700**, **KLC-0.33-800**, and **KLC-0.33-900**), including specific surface area, total pore volume and pore size were obtained from the nitrogen adsorption/desorption isotherms acquired at 77 K. This technique is routinely used to analyze the porous nature of activated carbon samples. **Figure 3.7(c)** provides the nitrogen adsorption/desorption isotherms while the textural properties of the carbon particles are summarized in **Table 3.3**. The isothermals for all the

carbon samples demonstrated typical type I isotherms with a sharp increment at low relative pressures in the range of $P/P_o$ < 0.01. This behavior is attributed to the predominantly microporous structure of the carbon specimens, based on the International Union of Pure and Applied Chemistry (IUPAC) definition [45]. In addition, there are small amounts of mesopores in these carbon samples **KLC-0.33-700**, **KLC-0.33-800**, and **KLC-0.33-900** because the nitrogen uptake slightly increased at higher relative pressures after the micropores were filled and the occurrence of a fairly flat plateau with a well-defined curve. The **LC-700** sample exhibited a low amount of nitrogen adsorption/desorption and its curve remained nearly horizontal throughout the entire range of relative pressure, indicating a lower specific surface area and less pores than the other samples. The specific surface area and total pore volume of the **LC-700** were determined to be 472 $m^2$ $g^{-1}$ and 0.233 $cm^3$ $g^{-1}$, respectively. These values are larger than those previously reported for carbon particles derived from other biomass materials (**Figure 3.7(e)** and **Table 3.4**). Furthermore, the specific surface area and total pore volume of the **LC-700** were significantly increased after the addition of KOH, demonstrating the importance of KOH activation with regard to obtaining well-developed porosity. The specific surface area and total pore volume of the **KLC-0.33-700** (936 $m^2$ $g^{-1}$ and 0.310 $cm^3$ $g^{-1}$) were larger than those of the **LC-700** (472 $m^2$ $g^{-1}$ and 0.233 $cm^3$ $g^{-1}$) obtained at the same carbonization temperature of 700 °C and it is evident that the **LC-700** sample was a moderately porous carbon. This outcome can be explained by the presence of considerable amounts of heteroatom such as oxygen in the Kraft lignin that was at least partly removed during the carbonization process [46]. Moreover, as expected, increasing the carbonization temperature from 700 to 900 °C resulted in higher specific surface area and greater total pore volume in the **KLC-0.33-700**, **KLC-0.33-800**, and **KLC-0.33-900**. The **KLC-0.33-900** sample was found to have the highest specific surface area of 1233 $m^2$ $g^{-1}$ together with a total pore volume of 0.436 $cm^3$ $g^{-1}$. These elevated values can be ascribed to the fact that the increase of carbonization temperature raises the reaction rate between carbon and KOH, leading to the development of a porous structure due to the formation and opening of the pores [47]. It can be expressed by the initial redox reaction between KOH and carbon at high temperature ($6KOH + 2C \rightarrow 2K + 2K_2CO_3 + 3H_2\uparrow$), which can generate the formation of potassium carbonate, the reduction of potassium cation into metallic potassium, and the reduction of hydroxyl anion into hydrogen gas.

Micropores are obtained as a result of the release of gaseous products such as $CO$, $CO_2$, and $H_2$, which are occurred through the decomposition of potassium carbonate at high temperature and hydroxyl reduction, respectively or by the intercalation of metallic potassium in the carbon matrix [48]. Their subsequent removal using hydrochloric acid results in a highly porous carbon structure as well as a high specific surface area. The pore size distributions were calculated using the DFT model depicted in **Figure 3.7(d)**. The pore size distribution curves for all samples confirmed that each had a microporous texture with a narrow micropore size distribution (< 2 nm) and the size distributions were all centered at approximately 0.7 nm. These results are in accordance with the nitrogen adsorption/desorption isotherms as shown in **Figure 3.7(c)**. It can be concluded that the shapes of these isothermals for all the **KLC-0.33** samples were similar, however, increasing the carbonization temperature also increased the amount of nitrogen that was adsorbed. These data indicate that the pore size remained constant but the number of pores was increased. In addition, the observed increase in pore volume with no change in the overall pore size distribution for each sample demonstrated that the application of different carbonization temperatures in conjunction with the use of KOH as an activation agent did not degrade the structure of these materials. This result is consistent with the SEM and TEM images in **Figure 3.6(a-1–c-1)** and **3.6(a-2–c-2)**, respectively.
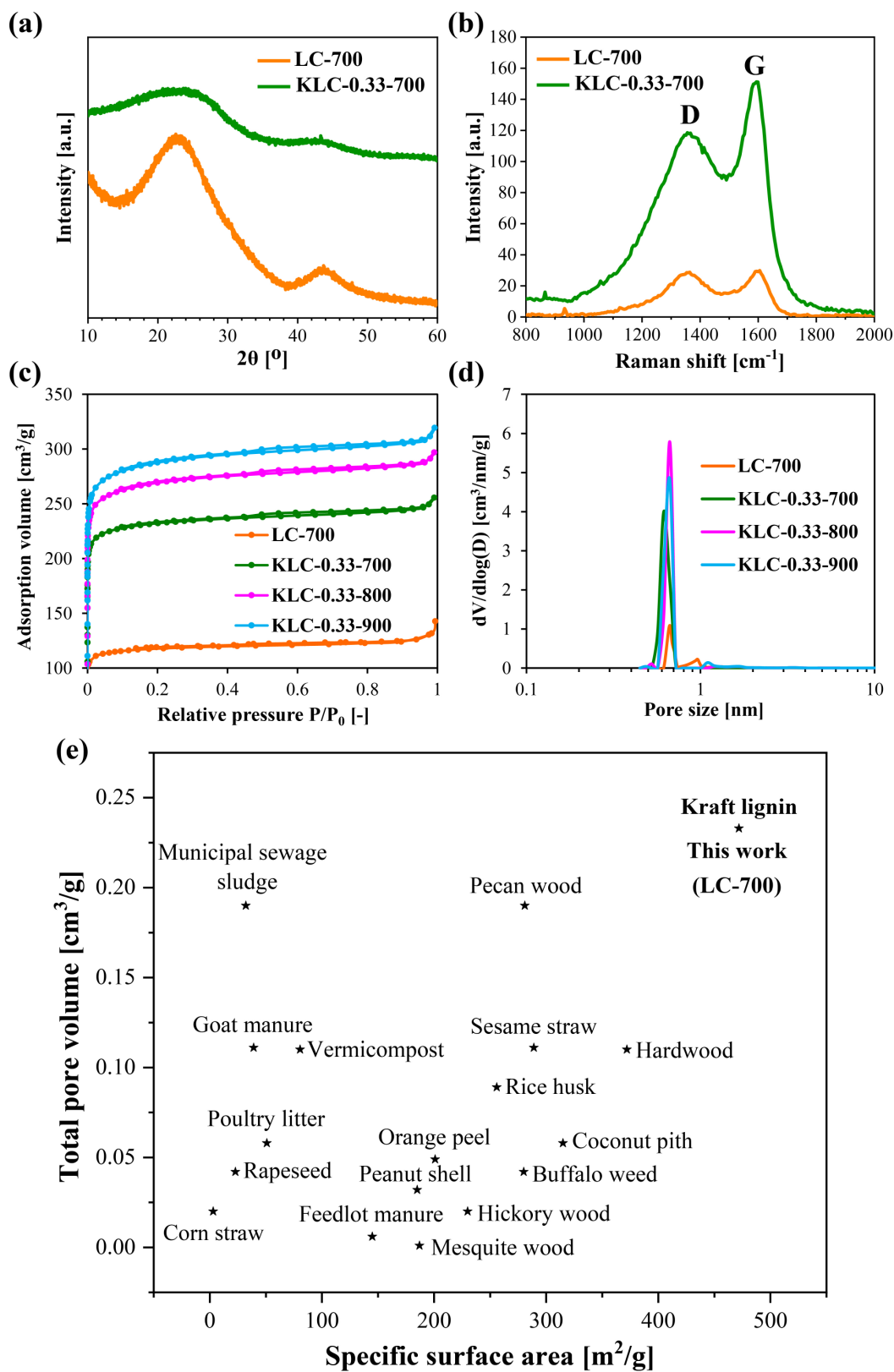
**Figure 3.7.** (a) XRD patterns and (b) Raman spectra of the **LC-700** and **KLC-0.33-700**, (c) nitrogen adsorption/desorption isotherms and (d) pore size distributions of the **LC-700**, **KLC-0.33-700**, **KLC-0.33-800**, and **KLC-0.33-900**, and (e) a comparison of the textural properties of previously reported carbon particles derived from different kinds of biomass.

**Table 3.3.** Textural properties of the **LC-700**, **KLC-0.33-700**, **KLC-0.33-800**, and **KLC-0.33-900**.

| Sample | Specific surface area | Total pore volume | Average pore size |
|---|---|---|---|
| | $[\text{m}^2\,\text{g}^{-1}]$ | $[\text{cm}^3\,\text{g}^{-1}]$ | [nm] |
| **LC-700** | 472 | 0.233 | 0.66 |
| **KLC-0.33-700** | 936 | 0.310 | 0.65 |
| **KLC-0.33-800** | 1160 | 0.407 | 0.70 |
| **KLC-0.33-900** | 1233 | 0.436 | 0.70 |

**Table 3.4.** Comparison of the textural properties of carbon particles derived from different kinds of biomass in the literature and in this study.

| Feedstock | Specific surface area $(\text{m}^2/\text{g})$ | Total pore volume $(\text{cm}^3/\text{g})$ | Reference |
|---|---|---|---|
| **Carbonization temperature (700 ºC)** | | | |
| **Kraft lignin** | **472** | **0.233** | **This work** |
| Hardwood | 372 | 0.110 | [49] |
| Coconut pith | 315 | 0.058 | [50] |
| Sesame straw | 289 | 0.111 | [51] |
| Pecan wood | 281 | 0.190 | [52] |
| Buffalo weed | 280 | 0.042 | [53] |

| | | | |
|---|---|---|---|
| Oak wood | 269 | 0.042 | [52] |
| Wheat straw | 256 | 0.200 | [54] |
| Rice husk | 256 | 0.089 | [55] |
| Alder wood | 250 | 0.033 | [52] |
| Hickory wood | 230 | 0.020 | [52] |
| Orange peel | 201 | 0.035 | [56] |
| Dairy manure | 187 | 0.044 | [57] |
| Mesquite wood | 187 | 0.001 | [52] |
| Peanut shell | 185 | 0.033 | [58] |
| Feedlot manure | 145 | 0.006 | [57] |
| Vermicompost | 80.8 | 0.111 | [59] |
| Poultry litter | 50.9 | 0.058 | [57] |
| Goat manure | 39.1 | 0.111 | [60] |
| Municipal sewage sludge | 32.2 | 0.190 | [61] |
| Sewage sludge | 29.9 | 0.049 | [62] |
| Rapeseed | 22.9 | 0.044 | [63] |
| Sewage sludge | 18.3 | 0.100 | [64] |
| Separated swine | 4.11 | 0.033 | [57] |
| Corn straw | 3.00 | 0.020 | [58] |

It is noteworthy that the particle morphology is an important factor affecting the tap density of a material, and the majority of synthetic carbon materials based on lignin suffer an issue of low tap density that severely hinders their practical applications. Therefore, the designed synthesis of spherical carbon particles with high tap density values is highly desirable. **Figure 3.8** shows the tap densities and provides the corresponding TEM images of the carbon particles derived from Kraft lignin with different structures. The tap density of the spherical carbon

particles with a dense structure (**KLC-0.33-700**) was measured to be approximately 1.46 g cm$^{-3}$, which is remarkably higher than the values for the **KLC-1.33-700** (having the spherical shape with a hollow structure, 0.61 g cm$^{-3}$) and **LC-700** (having the irregular shape with a hollow structure, 0.43 g cm$^{-3}$). In addition, the tap density of the **KLC-0.33-700** is also higher than those reported for commercially available activated carbons (0.4 – 0.8 g cm$^{-3}$), as well as those of carbon nanotubes and graphene (< 0.5 g cm$^{-3}$) [65]. Generally, the dense-packed architecture of carbon particles provides a higher tap density than that of non-spherical structures. Because the spherical particles have less contacting interface among each other, therefore, the aggregation of the particles within the powders comprised of spherical particles is much less than the other shape, resulting in less vacancy among the particles and the excellent fluidity of the powders [66].



| **(a) Dense spherical particle** | **(b) Hollow spherical particle** | **(c) Hollow non-spherical particle** |
|---|---|---|
| Volume = 1.00 cm$^3$ | Volume = 2.40 cm$^3$ | Volume = 3.40 cm$^3$ |
| **Tap density = 1.46 g cm$^{-3}$** | **Tap density = 0.61 g cm$^{-3}$** | **Tap density = 0.43 g cm$^{-3}$** |
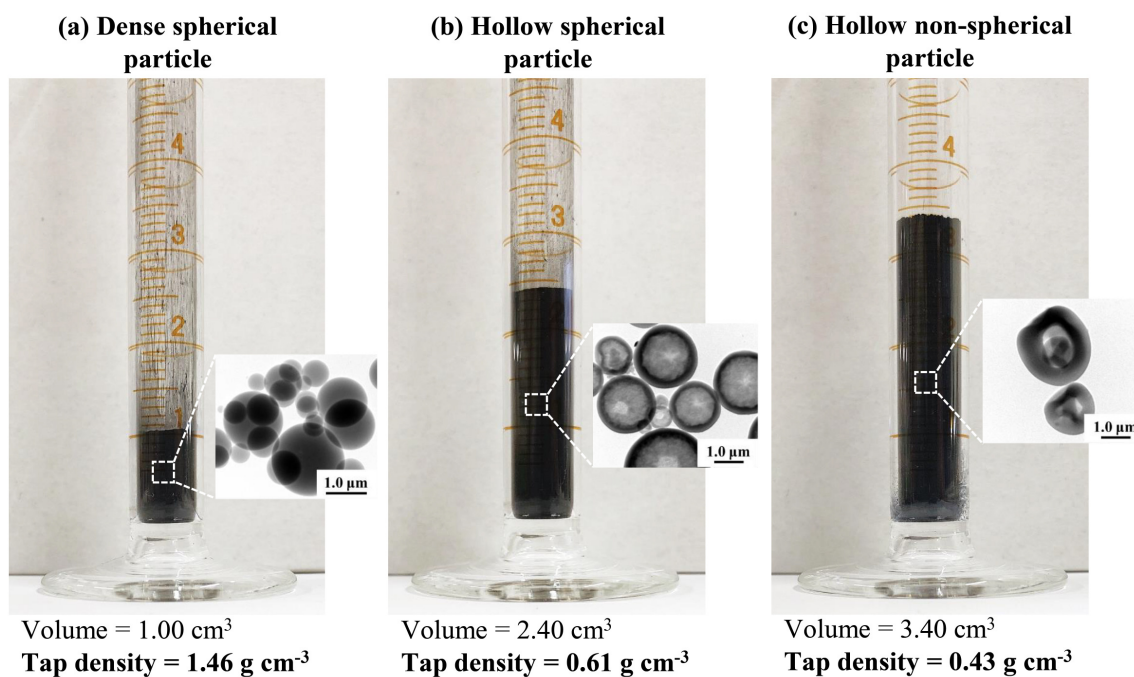
**Figure 3.8.** Tap densities and corresponding TEM images of carbon particles derived from Kraft lignin with (a) a dense spherical structure (**KLC-0.33-700**), (b) a hollow spherical structure (**KLC-1.33-700**), and (c) a hollow non-spherical structure (**LC-700**). The same type of the measuring cylinder with the same amount of 1.46 g for each sample **KLC-0.33-700**, **KLC-1.33-700**, and **LC-700** were added and repeatedly tapped until the volume of the powder no longer changed.

With regard to the synthesis and practical applications of nanostructured materials, the fabrication of dense carbon particles with perfectly spherical shapes using a simple procedure would be highly beneficial for our research directions in the future. In the case of batteries, a common drawback of hollow particle structures or the other shapes is the low packing density of the material in comparison with dense structure, which originated from the large amount of empty space within the particles. As a result, electrodes fabricated with these structures typically suffer from relatively low volumetric energy and power density, which are undesirable for practical applications [67]. The particles with spherical shapes can reduce this unnecessary void space, thus ensuring the maximum packing density of more active materials compared to the other shapes at the same volume. Moreover, dense-packed particles can be enhanced charge transport as well as improved structural robustness of the electrode [68]. As a result of these effects, the volumetric capacity of fabricated electrodes will be substantially increased. In addition, among the anode materials for batteries, hard carbon shows the best storage performance, and the carbon particles derived from Kraft lignin using our technique were found to be typical hard carbon materials. As shown in the XRD results, the average interlayer spacing $d_{002}$ value in our carbon sample was 0.365 nm, which is wider than that of graphite (0.335 nm) [43]. This increased $d$-spacing is likely to promote the diffusion and storage of ion (*e.g.* $Li^+$, $Na^+$, $K^+$) in such hard carbon materials, resulting in good electrochemical performance in batteries [69]. Besides, numerous studies have experimentally demonstrated that carbon materials with high micropore volumes are beneficial for improvement carbon dioxide and hydrogen uptake [48]. The carbon particles **KLC-0.33-900** had a relatively high specific surface area (1233 $m^2$ $g^{-1}$) as well as highly microporous with the size of the micropores 0.7 nm would be considered as a promising candidate. These extremely small micropores would be expected to provide extensive space for the movement of carbon dioxide and hydrogen molecules inside the carbon structure, leading to enhanced gas storage. To date, many studies have demonstrated the advantages of spherical carbon particles with dense structure in various fields. However, apart from the significant progress in fundamental aspects, the high cost and complex synthesis routes associated with these materials still restrict their practical uses. In terms of both sustainability and economic points of view, the synthetic protocols should be simplified as much as possible to reduce process complexity and production cost. With the great achievements and continuous

efforts on this important field, it is believed that the preparation of spherical structures will contribute to the development of new materials, which renders this approach attractive for diverse applications.

## 3.4. Conclusions

In summary, the spherical carbon particles derived from Kraft lignin has been successfully synthesized through a spray drying method followed by the carbonization process. The developed synthetic strategy is highly significant because it allows the utilization of lignin as an abundant and sustainable carbon precursor. This process could also be readily scaled up for mass production as a result of the cost-effectiveness and simplicity of the method. The carbon particles generated in this study could be obtained with spherical morphologies and it could be precisely controlled from dense to hollow sphere by varying the KOH concentration for the first time. In addition, to get a better understanding of the particle formation of carbon particles, a plausible mechanism has been discussed in this study, which provides insights with regard to the exploration of lignin-derived carbon materials. The specific surface area and tap density of spherical carbon particles having a dense structure were determined to be 1233 $m^2$ $g^{-1}$ and 1.46 g $cm^{-3}$, respectively, both of which are significantly higher than values reported for irregularly shaped carbon particles. The carbon sphere particles having a high tap density as advanced materials presented in this study can endow them for a broad prospect of applications in the areas of colloids and interface science as well as sustainable development.

## 3.5. References

[1]    Z. Yang, J. Ren, Z. Zhang, X. Chen, G. Guan, L. Qiu, Y. Zhang, H. Peng, Recent advancement of nanostructured carbon for energy applications, Chem. Rev. 115 (2015) 5159–5223.

[2]    T. Ogi, A.B.D. Nandiyanto, K. Okuyama, Nanostructuring strategies in functional fine-particle synthesis towards resource and energy saving applications, Adv. Powder Technol. 25 (2014) 3–17.

[3]     J. Lee, Y. Wu, Z. Peng, Hetero-nanostructured materials for high-power lithium ion batteries, J. Colloid Interface Sci. 529 (2018) 505–519.

[4]     T. Ogi, H. Fukazawa, A.M. Rahmatika, T. Hirano, K.L.A. Cao, F. Iskandar, Improving the crystallinity and purity of monodisperse Ag fine particles by heating colloidal sprays in-flight, Ind. Eng. Chem. Res. 59 (2020) 5745–5751.

[5]     K.L.A. Cao, S. Taniguchi, T.T. Nguyen, A.F. Arif, F. Iskandar, T. Ogi, Precisely tailored synthesis of hexagonal hollow silica plate particles and their polymer nanocomposite films with low refractive index, J. Colloid Interface Sci. 571 (2020) 378–386.

[6]     H.L. Wang, C.Y. Hsu, K.C.W. Wu, Y.F. Lin, D.H. Tsai, Functional nanostructured materials: Aerosol, aerogel, and de novo synthesis to emerging energy and environmental applications, Adv. Powder Technol. 31 (2020) 104–120.

[7]     T. Ogi, A.B.D. Nandiyanto, W.N. Wang, F. Iskandar, K. Okuyama, Direct synthesis of spherical YAG:Ce phosphor from precursor solution containing polymer and urea, Chem. Eng. J. 210 (2012) 461–466.

[8]     M. Österberg, M.H. Sipponen, B.D. Mattos, O.J. Rojas, Spherical lignin particles: A review on their sustainability and applications, Green Chem. 22 (2020) 2712–2733.

[9]     M.M. Titirici, R.J. White, N. Brun, V.L. Budarin, D.S. Su, F. Del Monte, J.H. Clark, M.J. MacLachlan, Sustainable carbon materials, Chem. Soc. Rev. 44 (2015) 250–290.

[10]    A.J. Romero-Anaya, M. Ouzzine, M.A. Lillo-Ródenas, A. Linares-Solano, Spherical carbons: Synthesis, characterization and activation processes, Carbon 68 (2014) 296–307.

[11]    R. Balgis, W. Widiyastuti, T. Ogi, K. Okuyama, Enhanced electrocatalytic activity of Pt/3D hierarchical bimodal macroporous carbon nanospheres, ACS Appl. Mater. Interfaces 9 (2017) 23792–23799.

[12]    L. Liu, Z.H. Xie, Q.F. Deng, X.X. Hou, Z.Y. Yuan, One-pot carbonization enrichment of nitrogen in microporous carbon spheres for efficient $CO_2$ capture, J. Mater. Chem. A 5 (2017) 418–425.

[13]   P.K. Sharma, V. V. Singh, N.K. Tripathi, M. Sathe, V. Verma, S.P. Sharma, L.N.S. Tomar, A. Chaturvedi, S.S. Yadav, V.B. Thakare, J. Acharya, A.K. Gupta, K. Ganesan, Chemical protection studies of activated carbon spheres based permeable protective clothing against sulfur mustard, a chemical warfare agent, Def. Sci. J. 69 (2019) 577–584.

[14]   L. Guo, J. Zhang, Q. He, L. Zhang, J. Zhao, Z. Zhu, W. Wu, J. Zhang, J. Shi, Preparation of millimetre-sized mesoporous carbon spheres as an effective bilirubin adsorbent and their blood compatibility, Chem. Commun. 46 (2010) 7127–7129.

[15]   K.L.A. Cao, A.F. Arif, K. Kamikubo, T. Izawa, H. Iwasaki, T. Ogi, Controllable synthesis of carbon-coated $SiO_x$ particles through a simultaneous reaction between the hydrolysis-condensation of tetramethyl orthosilicate and the polymerization of 3-aminophenol, Langmuir 35 (2019) 13681–13692.

[16]   J. Du, S. Zong, Y. Zhang, S. Hou, A. Chen, Co-assembly strategy for uniform and tunable hollow carbon spheres with supercapacitor application, J. Colloid Interface Sci. 565 (2020) 245–253.

[17]   R.S. Varma, Biomass-derived renewable carbonaceous materials for sustainable chemical and environmental applications, ACS Sustain. Chem. Eng. 7 (2019) 6458–6470.

[18]   F. Shen, X. Xiong, J. Fu, J. Yang, M. Qiu, X. Qi, D.C.W. Tsang, Recent advances in mechanochemical production of chemicals and carbon materials from sustainable biomass resources, Renew. Sustain. Energy Rev. 130 (2020) 109944.

[19]   J.L. Espinoza-Acosta, P.I. Torres-Chávez, J.L. Olmedo-Martínez, A. Vega-Rios, S. Flores-Gallardo, E.A. Zaragoza-Contreras, Lignin in storage and renewable energy applications: A review, J. Energy Chem. 27 (2018) 1422–1438.

[20]   W.J. Liu, H. Jiang, H.Q. Yu, Thermochemical conversion of lignin to functional materials: a review and future directions, Green Chem. 17 (2015) 4888–4907.

[21]   M. Kwiatkowski, V. Fierro, A. Celzard, Numerical studies of the effects of process conditions on the development of the porous structure of adsorbents prepared by chemical activation of lignin with alkali hydroxides, J. Colloid Interface Sci. 486 (2017) 277–286.

[22]    H.C. Ho, P. V. Bonnesen, N.A. Nguyen, D.A. Cullen, D. Uhrig, M. Goswami, J.K. Keum, A.K. Naskar, Method to synthesize micronized spherical carbon particles from lignin, Ind. Eng. Chem. Res. 59 (2020) 9–17.

[23]    S. Chaleawlert-Umpon, N. Pimpha, Sustainable lignin-derived hierarchically porous carbon for capacitive deionization applications, New J. Chem. 44 (2020) 12058–12067.

[24]    T. Shimada, T. Hata, M. Kijima, Thermal conversion of lignin-cellulose composite particles into aggregates of fine carbon grains holding micro- and mesoporous spaces, ACS Sustain. Chem. Eng. 3 (2015) 1690–1695.

[25]    H. Qin, R. Jian, J. Bai, J. Tang, Y. Zhou, B. Zhu, D. Zhao, Z. Ni, L. Wang, W. Liu, Q. Zhou, X. Li, Influence of molecular weight on structure and catalytic characteristics of ordered mesoporous carbon derived from lignin, ACS Omega 3 (2018) 1350–1356.

[26]    Z.W. He, J. Yang, Q.F. Lü, Q. Lin, Effect of structure on the electrochemical performance of nitrogenand oxygen-containing carbon micro/nanospheres prepared from lignin-based composites, ACS Sustain. Chem. Eng. 1 (2013) 334–340.

[27]    R. Mondal, A. Das, D. Sen, D.K. Satapathy, M.G. Basavaraj, Spray drying of colloidal dispersions containing ellipsoids, J. Colloid Interface Sci. 551 (2019) 242–250.

[28]    A.B.D. Nandiyanto, T. Ogi, W.N. Wang, L. Gradon, K. Okuyama, Template-assisted spray-drying method for the fabrication of porous particles with tunable structures, Adv. Powder Technol. 30 (2019) 2908–2924.

[29]    A.M. Rahmatika, Y. Goi, T. Kitamura, W. Widiyastuti, T. Ogi, TEMPO-oxidized cellulose nanofiber (TOCN) decorated macroporous silica particles: Synthesis, characterization, and their application in protein adsorption, Mater. Sci. Eng. C 105 (2019) 110033.

[30]    J. Pang, W.F. Zhang, J.L. Zhang, H.M. Zhang, G.P. Cao, M.F. Han, Y.S. Yang, Oxygen and nitrogen co-enriched sustainable porous carbon hollow microspheres from sodium lignosulfonate for supercapacitors with high volumetric energy densities, ChemElectroChem 5 (2018) 1306–1320.

[31]    Y. Chen, G. Zhang, J. Zhang, H. Guo, X. Feng, Y. Chen, Synthesis of porous carbon spheres derived from lignin through a facile method for high performance supercapacitors, J. Mater. Sci. Technol. 34 (2018) 2189–2196.

[32]    S. Iravani, R.S. Varma, Greener synthesis of lignin nanoparticles and their applications, Green Chem. 22 (2020) 612–636.

[33]    W. Zhang, M. Zhao, R. Liu, X. Wang, H. Lin, Hierarchical porous carbon derived from lignin for high performance supercapacitor, Colloids Surfaces A Physicochem. Eng. Asp. 484 (2015) 518–527.

[34]    A.M. Navarro-Suárez, D. Saurel, P. Sánchez-Fontecoba, E. Castillo-Martínez, J. Carretero-González, T. Rojo, Temperature effect on the synthesis of lignin-derived carbons for electrochemical energy storage applications, J. Power Sources 397 (2018) 296–306.

[35]    F. Iskandar, L. Gradon, K. Okuyama, Control of the morphology of nanostructured particles prepared by the spray drying of a nanoparticle sol, J. Colloid Interface Sci. 265 (2003) 296–303.

[36]    E. Lintingre, F. Lequeux, L. Talini, N. Tsapis, Control of particle morphology in the spray drying of colloidal suspensions, Soft Matter. 12 (2016) 7435–7444.

[37]    A.H. Lefebvre, V.G. Mcdonell, Atomization and sprays, Second Edition., 2017.

[38]    A. Osman, L. Goehring, A. Patti, H. Stitt, N. Shokri, Fundamental investigation of the drying of solid suspensions, Ind. Eng. Chem. Res. 56 (2017) 10506–10513.

[39]    W. Zhang, R. Shen, K. Lu, A. Ji, Z. Cao, Nanoparticle enhanced evaporation of liquids: A case study of silicone oil and water, AIP Adv. 2 (2012) 042119.

[40]    A. Zhang, X.Y. Li, S. Zhang, Z. Yu, X. Gao, X. Wei, Z. Wu, W.D. Wu, X.D. Chen, Spray-drying-assisted reassembly of uniform and large micro-sized MIL-101 microparticles with controllable morphologies for benzene adsorption, J. Colloid Interface Sci. 506 (2017) 1–9.

[41]   R. Vehring, W.R. Foss, D. Lechuga-Ballesteros, Particle formation in spray drying, J. Aerosol Sci. 38 (2007) 728–746.

[42]   F. Fu, D. Yang, W. Zhang, H. Wang, X. Qiu, Green self-assembly synthesis of porous lignin-derived carbon quasi-nanosheets for high-performance supercapacitors, Chem. Eng. J. 392 (2020) 123721.

[43]   Z. Yuan, L. Si, X. Zhu, Three-dimensional hard carbon matrix for sodium-ion battery anode with superior-rate performance and ultralong cycle life, J. Mater. Chem. A 3 (2015) 23403–23411.

[44]   H. Feng, H. Hu, H. Dong, Y. Xiao, Y. Cai, B. Lei, Y. Liu, M. Zheng, Hierarchical structured carbon derived from bagasse wastes: A simple and efficient synthesis route and its improved electrochemical properties for high-performance supercapacitors, J. Power Sources 302 (2016) 164–173.

[45]   K.S.W. Sing, D.H. Everett, R.A.W. Haul, L. Moscou, R.A. Pierotti, J. Rouquerol, T. Siemieniewska, Reporting physisorption data for gas/solid systems with special reference to the determination of surface area and porosity, Pure Appl. Chem. 57 (1985) 603–619.

[46]   M. Klose, R. Reinhold, F. Logsch, F. Wolke, J. Linnemann, U. Stoeck, S. Oswald, M. Uhlemann, J. Balach, J. Markowski, P. Ay, L. Giebeler, Softwood lignin as a sustainable feedstock for porous carbons as active material for supercapacitors using an ionic liquid electrolyte, ACS Sustain. Chem. Eng. 5 (2017) 4094–4102.

[47]   J. Liu, N. Sun, C. Sun, H. Liu, C. Snape, K. Li, W. Wei, Y. Sun, Spherical potassium intercalated activated carbon beads for pulverised fuel $CO_2$ post-combustion capture, Carbon 94 (2015) 243–255.

[48]   G. Singh, I.Y. Kim, K.S. Lakhi, P. Srivastava, R. Naidu, A. Vinu, Single step synthesis of activated bio-carbons with a high surface area and their excellent $CO_2$ adsorption capacity, Carbon 116 (2017) 448–455.

[49]   Y. Han, A.A. Boateng, P.X. Qi, I.M. Lima, J. Chang, Heavy metal and phenol adsorptive properties of biochars from pyrolyzed switchgrass and woody biomass in correlation with

surface properties, J. Environ. Manage. 118 (2013) 196–204.

[50] K. Johari, N. Saman, S.T. Song, S.C. Cheu, H. Kong, H. Mat, Development of coconut pith chars towards high elemental mercury adsorption performance - Effect of pyrolysis temperatures, Chemosphere 156 (2016) 56–68.

[51] J.H. Park, Y.S. Ok, S.H. Kim, J.S. Cho, J.S. Heo, R.D. Delaune, D.C. Seo, Competitive adsorption of heavy metals onto sesame straw biochar in aqueous solutions, Chemosphere 142 (2016) 77–83.

[52] C. Trigo, L. Cox, K. Spokas, Influence of pyrolysis temperature and hardwood species on resulting biochar properties and their effect on azimsulfuron sorption as compared to other sorbents, Sci. Total Environ. 566–567 (2016) 1454–1464.

[53] K. Yakkala, M.R. Yu, H. Roh, J.K. Yang, Y.Y. Chang, Buffalo weed (*Ambrosia trifida L. var. trifida*) biochar for cadmium (II) and lead (II) adsorption in single and mixed system, Desalin. Water Treat. 51 (2013) 7732–7745.

[54] J. Chi, H. Liu, Effects of biochars derived from different pyrolysis temperatures on growth of *Vallisneria spiralis* and dissipation of polycyclic aromatic hydrocarbons in sediments, Ecol. Eng. 93 (2016) 199–206.

[55] K. Jindo, H. Mizumoto, Y. Sawada, M.A. Sanchez-Monedero, T. Sonoki, Physical and chemical characterization of biochars derived from different agricultural residues, Biogeosciences 11 (2014) 6613–6621.

[56] B. Chen, Z. Chen, Sorption of naphthalene and 1-naphthol by biochars of orange peels with different pyrolytic temperatures, Chemosphere 76 (2009) 127–133.

[57] K.B. Cantrell, P.G. Hunt, M. Uchimiya, J.M. Novak, K.S. Ro, Impact of pyrolysis temperature and manure source on physicochemical characteristics of biochar, Bioresour. Technol. 107 (2012) 419–428.

[58] X. Gai, H. Wang, J. Liu, L. Zhai, S. Liu, T. Ren, H. Liu, Effects of feedstock and pyrolysis temperature on biochar adsorption of ammonium and nitrate, PLoS One 9

(2014) 1–19.

[59]  G. Yang, Z. Wang, Q. Xian, F. Shen, C. Sun, Y. Zhang, J. Wu, Effects of pyrolysis temperature on the physicochemical properties of biochar derived from vermicompost and its potential use as an environmental amendment, RSC Adv. 5 (2015) 40117–40125.

[60]  N. Touray, W.T. Tsai, H.R. Chen, S.C. Liu, Thermochemical and pore properties of goat-manure-derived biochars prepared from different pyrolysis temperatures, J. Anal. Appl. Pyrolysis 109 (2014) 116–122.

[61]  T. Chen, Y. Zhang, H. Wang, W. Lu, Z. Zhou, Y. Zhang, L. Ren, Influence of pyrolysis temperature on characteristics and heavy metal adsorptive performance of biochar derived from municipal sewage sludge, Bioresour. Technol. 164 (2014) 47–54.

[62]  A. Zielińska, P. Oleszczuk, Effect of pyrolysis temperatures on freely dissolved polycyclic aromatic hydrocarbon (PAH) concentrations in sewage sludge-derived biochars, Chemosphere 153 (2016) 68–74.

[63]  D. Angin, S. Şensöz, Effect of pyrolysis temperature on chemical and surface properties of biochar of rapeseed (*Brassica napus* L.), Int. J. Phytoremediation 16 (2014) 684–693.

[64]  J. Zhang, F. Lü, H. Zhang, L. Shao, D. Chen, P. He, Multiscale visualization of the structural and characteristic changes of sewage sludge biochar oriented towards potential agronomic and environmental implication, Sci. Rep. 5 (2015) 9406.

[65]  J. Pang, W. Zhang, J. Zhang, G. Cao, M. Han, Y. Yang, Facile and sustainable synthesis of sodium lignosulfonate derived hierarchical porous carbons for supercapacitors with high volumetric energy densities, Green Chem. 19 (2017) 3916–3926.

[66]  J. Ying, C. Jiang, C. Wan, Preparation and characterization of high-density spherical LiCoO2 cathode material for lithium ion batteries, J. Power Sources 129 (2004) 264–269.

[67]  J. Liang, X.Y. Yu, H. Zhou, H. Bin Wu, S. Ding, X.W. Lou, Bowl-like SnO$_2$@carbon hollow particles as an advanced anode material for lithium-ion batteries, Angew. Chemie - Int. Ed. 53 (2014) 12803–12807.

[68]   Y. Lee, S. Noh, M.S. Kim, H.J. Kong, K. Im, O.S. Kwon, S. Kim, H. Yoon, The effect of nanoparticle packing on capacitive electrode performance, Nanoscale 8 (2016) 11940–11948.

[69]   F. Wu, L. Liu, Y. Yuan, Y. Li, Y. Bai, T. Li, J. Lu, C. Wu, Expanding interlayer spacing of hard carbon by natural $K^+$ doping to boost Na-ion storage, ACS Appl. Mater. Interfaces 10 (2018) 27030–27038.

## Chapter 4

# Sustainable Porous Hollow Carbon Spheres with High Specific Surface Area Derived from Kraft Lignin

### 4.1. Introduction

Hollow structures, defined as architectures comprising outer shells and internal voids, represent a special class of functional nanomaterials. The rational design and fabrication of these materials have become an important research topic during the last two decades [1–5]. In comparison to the solid counterparts, hollow structures (especially those with permeable porous shells) exhibit many attractive intrinsic properties such as extraordinarily high specific surface areas, large internal void spaces, low densities, and high loading capacities [5–7]. These unique characteristics promote hollow structural materials as good candidates for use across a wide range of potential applications in various fields, including catalyst supports [8], biomedical engineering [9], drug storage and delivery [10], optical devices [5], and energy storage [11,12]. Particularly, among the various structures of carbon-based materials, hollow carbon spheres (HCSs) have attracted much attention due to their intriguing structure-induced properties and numerous applications [13–15]. Although many methods for the preparation of hollow carbon materials have already been developed, the synthesis of HCSs with well-controlled morphologies still remains a significant challenge.

The production of carbon-based materials from green, renewable, and cost-effective resources in accordance with sustainable development goals is highly important. In this regard, lignocellulosic biomass (such as cellulose, hemicellulose, and lignin) represents an especially useful raw material for the synthesis of porous carbon [16,17]. From the perspective of sustainability, lignin as the second most abundant renewable natural biopolymer after cellulose and the most common aromatic polymer on earth has been drawing an increasing attention for numerous applications [18]. However, the majority of technical lignin is not effectively recycled or utilized at the moment, and some is directly combusted as a low-value fuel, leading to

environmental pollution and a waste of natural resources [19]. Only a small portion (less than 2 wt%) of technical lignin can be applied as an alternative material. Therefore, based on the high underutilization of lignin, it is important to transform lignin wastes into higher value-added products to decrease the environmental impact of this resource, and to ensure a more sustainable future. Due to its low manufacturing cost, significant carbon content (about 60 wt%), and high aromaticity, lignin has recently been considered as a potential sustainable source for the preparation of advanced porous carbonaceous materials [20]. In particular, porous carbon particles based on lignin or lignin derivatives can be prepared through a hard-template/soft-template method [21,22] or a combination of template and activation methods [23], as well as the direct pyrolysis of spherical precursors [24]. However, there are various problems associated with each of these fabrication techniques. Firstly, it is difficult to obtain uniform dispersions due to the poor compatibility between lignin and the various templates [25]. Secondly, hazardous reagents are required to remove the templates after the particles are formed. These reagents can not only cause collapse or deformation of the geometric structures (*e.g.* morphology, shell thickness) but also difficult to recycle, and so are a potential cause of environmental pollution [22]. Finally, the combination methods tend to provide low yields and require prolonged reaction times, multiple process steps, rigorous synthesis conditions, complicated equipment, high processing temperatures, and high energy consumption, all of which limit practical mass production in an environmentally friendly and economically sustainable manner [26]. Therefore, the ideal manufacturing methods for the fabrication of HCSs without the addition of templating agents are imperative.

Spray drying is the most promising technology for producing particles from precursor solutions via a simple one-step process. It is well-known as a scalable and effective method to synthesize homogeneous composites and various nanostructured functional materials [27–29]. The widespread utilization of spray drying can be attributed to its advantages over the other methods described above, especially with regard to practical applications. These advantages include (i) the efficient preparation of homogeneous multicomponent materials and composites with precisely controlled stoichiometric ratios, (ii) simple particle collection equipment, (iii) single-step processing, (iv) continuous operation, and (v) easy scale-up to provide high productivity [30–34]. Therefore, template-free spray drying is able to produce HCSs by simply

using the appropriate precursors, and so provides a very simple and convenient method for obtaining these materials that also avoids the introduction of impurities.

Lignosulfonate is a useful raw material for the preparation of carbon particles because it is highly soluble in water, renewable, thermally stable, and environmentally friendly [35]. However, the utilization of lignosulfonate is not always advantageous. Kraft lignin has unique properties and its composition makes it a promising candidate for the synthesis of carbon-based materials as a replacement for lignosulfonate. Specifically, Kraft lignin can be obtained more easily than lignosulfonate worldwide because the sulfite pulping process is less common than the Kraft pulping process [36]. In addition, Kraft lignin is generally more pure with low sulfur concentrations, fewer carbohydrate residues, and inorganic impurities [37]. Furthermore, the complete removal of sulfur from lignosulfonate is more difficult because the sulfur is chemically bonded to the lignin, such that the products tend to be impure [36]. To the best of our knowledge, there has been only one article from our group reported the successful synthesis of porous carbon particles with well-defined spherical morphologies through spray drying approach using Kraft lignin as the carbon precursor and potassium hydroxide (KOH) as the activator [30]. Therefore, the utilization of Kraft lignin as an alternative carbon precursor rather than the more common raw material lignosulfonate still presents a challenge, with regard to the development of a highly efficient synthetic process. Furthermore, our previous work focused only on the mechanism by which carbon particles were generated and the characterization of dense spherical carbon products with high tap density values. However, the characterization of the prepared HCSs with their structural, pore texture, surface morphology, and electrochemical performance for supercapacitors has not been explored in our prior research. Therefore, it is highly important to investigate the feasibility of obtaining HCSs derived from Kraft lignin, which represents a promising sustainable material for potential applications in the research areas of advanced powder technology.

Based on the above and building on our previously reported work, the objective of the present study was to employ a spray drying technique followed by a simple carbonization process for the precise design of HCSs with high specific surface area from Kraft lignin using an appropriate amount of KOH. This process was selected because KOH still appears to be the

simplest and most economical reagent for this purpose, as it readily dissolves lignin, which is considered to promote activation of the biomass. The advantages of this process include stability without any requirement for copolymers, surfactants or catalysts, and suitability for large scale applications. Furthermore, the present method does not involve any functionalization, additional reagents, or complicated chemical reactions, meaning that it can improve the efficiency and reduce both the amount of time required to obtain products and the initial capital expenditures for equipment. Therefore, this process has significant potential for practical applications. In addition, the porosity of the as-prepared HCSs can be easily tuned in a relatively wide range by simply adjusting the KOH concentration or the carbonization temperature. Finally, to explore the applications in electrochemistry, these HCSs could be used as active electrode materials in supercapacitors for energy storage devices. The extremely simple synthetic route proposed herein is not only cost-effective and environmentally benign but also suitable for the large-scale production of HCSs. The results of this work are therefore expected to contribute to the development of new strategies for the manufacture of HCSs derived from Kraft lignin with novel structures and advanced functions.

## 4.2. Experimental

### 4.2.1. Synthesis of HCSs from Kraft lignin

All the chemical reagents used in this work were of analytical grade and were directly used as received without further purification. Cross-linked Kraft lignin for use as the carbon source was supplied by the Kuraray Co., Ltd., Japan. As illustrated in **Figure 4.1**, the hollow carbon particles were prepared through a three-step process. In each trial, a portion of Kraft lignin was dissolved in distilled water together with varying amounts of solid KOH (Kanto Chemical Co., Inc., Tokyo, Japan) to form a homogeneous dispersion, after which the reaction mixture was stirred for 30 min at room temperature. This solution was subsequently transferred to a mini spray-dryer (BÜCHI B-290, Switzerland) and spray-dried at an inlet temperature of 200 °C through a two-fluid nozzle system. The precursor solution was pumped into the nozzle at a flow rate of 2.5 mL/min, using hot air as the carrier gas at a flow rate of 10 L/min to obtain the

spherical lignin/KOH composite particles. These composite particles were then carbonized in a horizontal tube furnace under a constant 1.0 L/min flow of nitrogen by heating from room temperature to the desired temperature (700 – 900 °C) at 5 °C/min and then maintaining this temperature for 2 h. After allowing the carbonized material to naturally cool to room temperature, the sample was washed with 10 wt% aqueous hydrochloric acid (HCl) solution (Kanto Chemical Co., Inc., Tokyo, Japan) to eliminate residual KOH and other impurities. The resulting black powder was washed with distilled water and then recovered by centrifugation, and this process was repeated until the wash water showed a pH of approximately 7. The resulting carbon particles were subsequently dried at 105 °C for 12 h in a vacuum oven. The final products are denoted herein as **KLC-X-Y**, where X corresponds to the mass ratio of KOH to lignin (X = 0.67, 0.83, 1.00, 1.33, and 1.50), and Y represents the carbonization temperature (Y = 700, 800, and 900 °C). Details of the sample preparation conditions are summarized in **Table 4.1**.
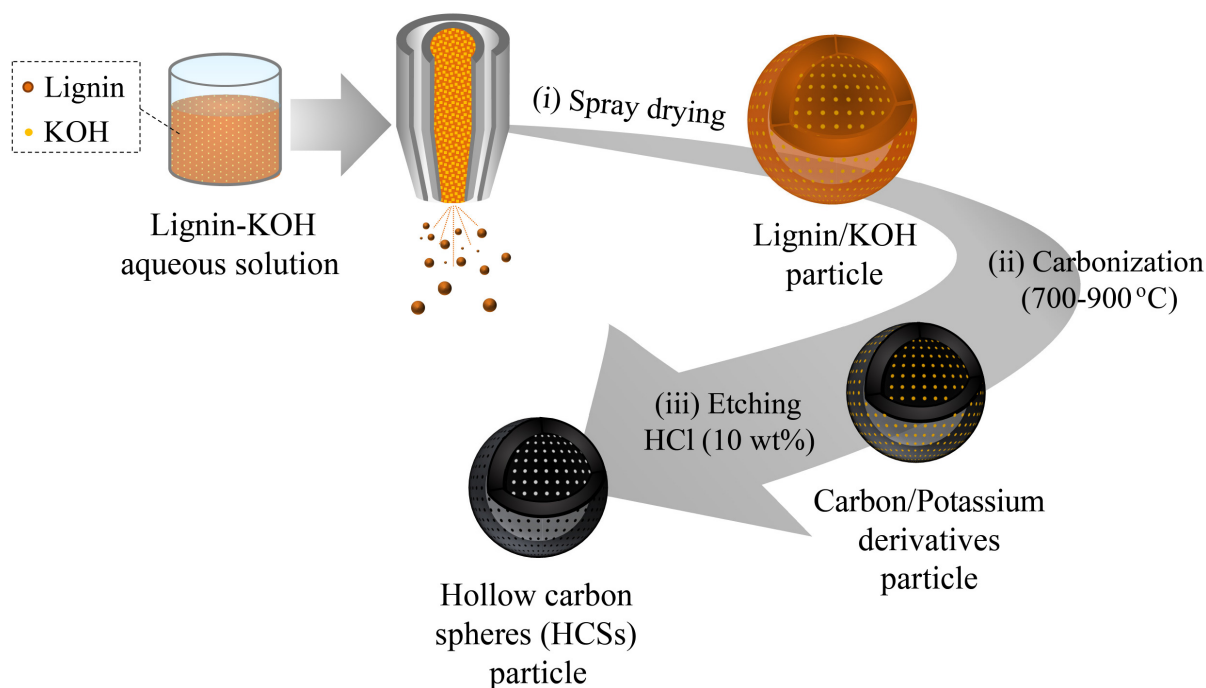


**Figure 4.1.** Schematic representation for the preparation of hollow carbon spheres (HCSs) particle derived from Kraft lignin.

**Table 4.1.** Formulations for the specimens synthesized from Kraft lignin in this work.

| Sample name | Lignin (g) | KOH (g) | Water (g) | KOH/lignin (-) | Carbonization temperature (ºC) |
|---|---|---|---|---|---|
| KLC-0.67-700 | 1.2 | 0.8 | 64 | 0.67 | 700 |
| KLC-0.83-700 | 1.2 | 1.0 | 64 | 0.83 | 700 |
| KLC-1.00-700 | 1.2 | 1.2 | 64 | 1.00 | 700 |
| KLC-1.33-700 | 1.2 | 1.6 | 64 | 1.33 | 700 |
| KLC-1.50-700 | 1.2 | 1.8 | 64 | 1.50 | 700 |
| KLC-1.33-800 | 1.2 | 1.6 | 64 | 1.33 | 800 |
| KLC-1.33-900 | 1.2 | 1.6 | 64 | 1.33 | 900 |

*4.2.2. Materials characterization*

The surface morphologies and structures of the as-synthesized carbon samples were observed using field emission scanning electron microscopy (FE-SEM; S-5200, 20 kV, Hitachi High Technologies. Corp., Tokyo, Japan) and transmission electron microscopy (TEM; JEM-2010, 200 kV, JEOL Ltd., Tokyo, Japan). The particle sizes were determined by measuring the diameters of more than 350 randomly selected particles identified in the SEM and TEM images. The crystalline structures of the prepared particles were evaluated by powder X-ray diffraction (XRD; D2 Phaser, 40 kV and 30 mA, Bruker Corp., USA). The porous textures of all the carbon samples were determined from nitrogen adsorption/desorption isotherms acquired at 77 K (BELSORP-max, MicrotracBEL Corp., Osaka, Japan). Prior to these analyses, all samples were outgassed under a high vacuum at 300 ºC for 8 h to ensure that all moisture and other volatiles had been eliminated. Specific surface areas were calculated from the resulting isotherms using the Brunauer-Emmett-Teller (BET) method, while the existence of micropores and mesopores in the carbon shell was determined by the Horvath-Kawazoe (HK) and Barrett-Joyner-Halenda (BJH) methods, respectively. The total pore volumes were obtained from the amounts of nitrogen adsorbed at a relative pressure of 0.995. The shell density of all HCS samples was

109

determined by the helium gas replacement method using a true density measuring apparatus (BELSORP-max, MicrotracBEL Corp., Osaka, Japan). The measurement system was typically controlled by a computer. The density measurement was performed by filling the cavity with helium gas to measure the volume of the carbon material. The true density value was obtained by the quantity of carbon powder dividing effective volumetric capacity. The pores existed in the inner and outer surfaces of carbon shell; therefore, it was assumed that the shell density of HCSs can be equal to the true density of HCSs.

### 4.2.3. Electrochemical characterization

The electrochemical properties of all HCS samples were assessed in a standard two-electrode system (representing a supercapacitor device) with an aqueous 6 M KOH solution as the electrolyte. The working electrodes were fabricated by mixing the HCSs (85 wt%) as the active material, acetylene black (10 wt%) as the conductive additive, and polytetrafluoroethylene (PTFE) (5 wt%) as the binder in ethanol. The resulting slurry was rolled into sheets and dried in a vacuum oven at 100 °C overnight to remove the solvent before pressing. The material was subsequently cut into electrode sheets with geometric surface areas of $1 \times 1$ cm$^2$. Each electrode sheet was pressed onto nickel foam under a pressure of 10 MPa to fabricate a supercapacitor electrode. These HCS electrodes were subsequently assembled into symmetric supercapacitors with equivalent mass loadings in the positive and negative electrodes. The capacitive performances of the HCSs were investigated using a symmetric supercapacitor apparatus in conjunction with galvanostatic charge–discharge (GCD) measurements at a current density of 0.2 A g$^{-1}$ within the potential window from 0 to 2.5 V in an aqueous 6 M KOH solution. Alternating current electrochemical impedance spectroscopy (EIS) was conducted at an open circuit voltage with an amplitude of 10 mV in the frequency range from 0.01 Hz to 100 kHz.

The specific capacitance, $C$ (F g$^{-1}$), of each electrode material was calculated from the discharge part of its GCD curve according to the equation:

$$C = \frac{2 \times I \times \Delta t}{m \times \Delta V}$$

where $I$ is the response discharge current (A), $\Delta t$ is the discharge time (s), $m$ is the mass of the active material (g), and $\Delta V$ is the working potential window (V). Active material here refers to HCSs, which do not include acetylene black and PTFE.

The electrode density values, $\rho$ (g cm$^{-3}$), were determined from the equation:

$$\rho = \frac{m}{V}$$

where $m$ is the total mass of the electrode material (g) and $V$ is the total volume of the electrode material (cm$^3$), including the active material, acetylene black, and binder. This volume was calculated by measuring the length ($l$), width ($w$), and thickness ($h$) of the electrode material under a pressure of 10 MPa ($V = l \times w \times h$).

## 4.3. Results and Discussion

### 4.3.1. Synthesis of HCSs from Kraft lignin

The morphologies and interior structures of carbon particles derived from lignin/KOH composites (**KLC-X-700**, where X represents the mass ratio of KOH to lignin) were assessed using SEM and TEM, and typical images are presented in **Figure 4.2**. Carbon particles with a relatively uniform spherical morphology were evidently formed when the KOH concentration in the reaction system was sufficiently high (**Figure 4.2(a-1–d-1)**), indicating the viability of this synthetic system. However, it should be noted that the sample in **Figure 4.2(e-1)** was an exception. In comparison with the previously reported results [38,39], the acquired carbon particles derived from lignin usually possessed an irregular shape. Therefore, the present method appears to be an effective approach for creating spherical carbon particles from lignin and KOH, which are highly desirable for use in a broad range of potential applications. In addition, the SEM images in **Figure 4.2(a-1–e-1)** show that the KOH concentration affected the particle sizes. Specifically, the average carbon particle size increased from 1.41 to 2.42 μm as the KOH/lignin mass ratio was increased from 0.67 to 1.50. Interestingly, increasing the KOH/lignin mass ratio from 0.67 to 1.33 produced no noticeable changes in the uniform spherical morphology and structural integrity of the particles. However, after the proportion of KOH added and reached a KOH/lignin mass ratio of 1.50, the morphology of **KLC-1.50-700** changed slightly, such that the

surfaces of this material became uneven with many holes (**Figure 4.2(e-1)**). At this high KOH/lignin mass ratio, the KOH was more likely to accumulate in the composite and form holes on both the interior and exterior surfaces of the spheres. More specifically, the high KOH concentration decomposed the carbon walls connecting the continuously oriented porous structure of the material through oxidation at a high carbonization temperature. In addition, the numerous potassium atoms that were generated during the activation process completely changed the surface morphology of the **KLC-1.50-700** [40]. The TEM images provided in **Figure 4.2(a-2–e-2)** show the internal structures of the carbon particles. It is apparent that the hollow structures were formed in all cases for these carbon particles. The observation in TEM images showed that the shell thickness of the carbon samples becomes thinner (decreased from 235 to 131 nm) as the amount of KOH increases. Therefore, the ratio of particle size/shell thickness increased from 6 to 18 with increasing the KOH/lignin mass ratio from 0.67 to 1.50. In addition, the shell density of all HCS samples can be determined by the helium gas replacement method. At different KOH/lignin mass ratios of 0.67, 0.83, 1.00, and 1.33, the shell density was obtained to be 2.14, 1.86, 1.54, and 1.45 g cm$^{-3}$, respectively. The mechanism by which HCSs are formed during spray drying has been explained in detail in a previous publication by our group [30]. These observation results reveal that controlling the appropriate amount of KOH is a key to obtain the hollow carbon particles with regular morphologies from Kraft lignin.
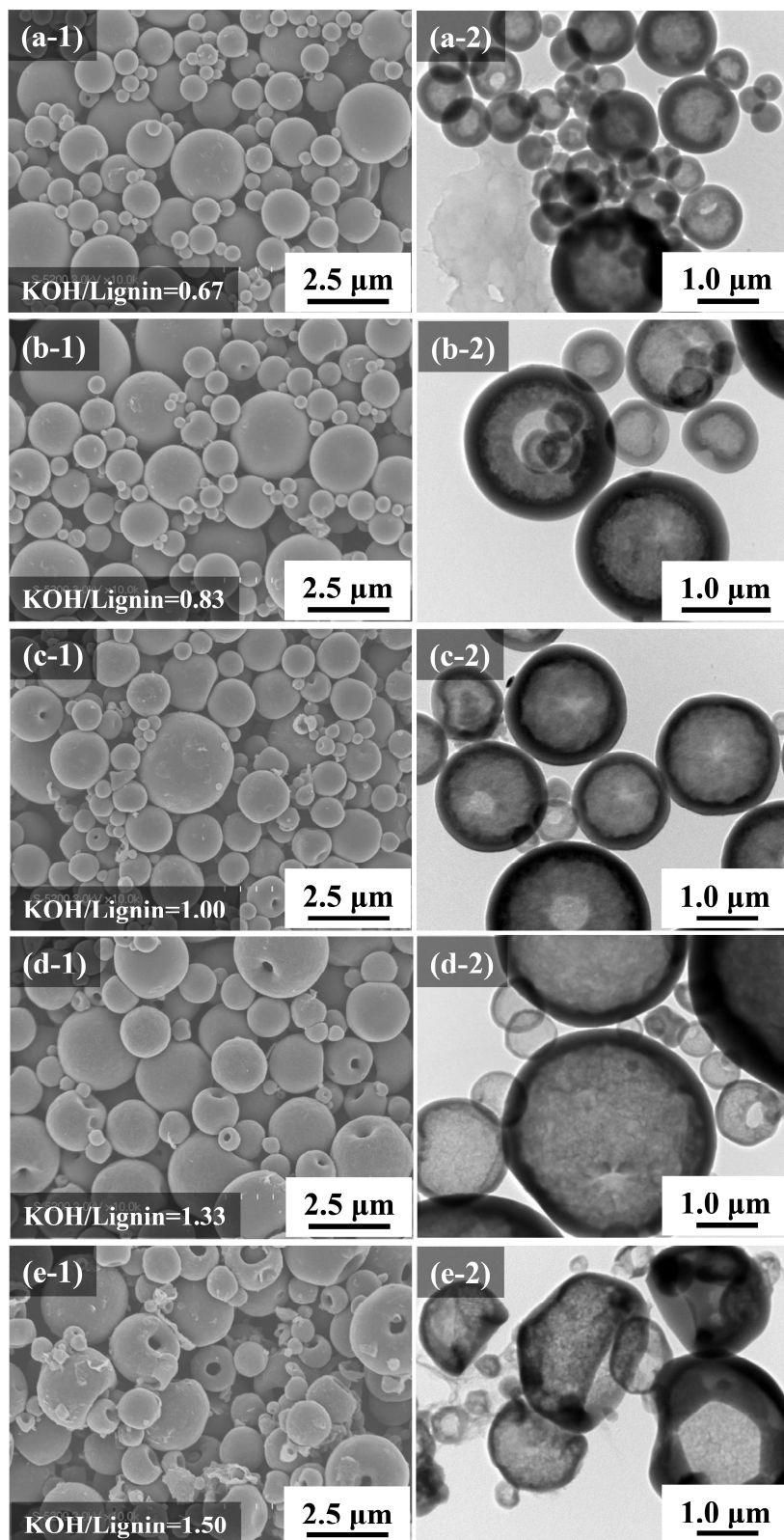
**Figure 4.2.** SEM (left) and TEM (right) images of carbon particles derived from lignin/KOH composites at KOH/lignin mass ratios of (a) 0.67 (**KLC-0.67-700**), (b) 0.83 (**KLC-0.83-700**), (c) 1.00 (**KLC-1.00-700**), (d) 1.33 (**KLC-1.33-700**), and (e) 1.50 (**KLC-1.50-700**).

For a better understanding of the characteristics of these carbon particles, the various characterization techniques were investigated as summarized in **Figure 4.3**. The amorphous nature of the carbon materials obtained at different KOH/lignin mass ratios was determined by XRD analysis, and the results are shown in **Figure 4.3(a)**. Obviously, two relatively broad diffraction peaks centered at $2\theta$ values of approximately 23 and 43° appear in the pattern of each sample, which are attributed to diffractions from the (002) planes of graphitic carbon and (100) planes of the graphite lattice, respectively [30]. These results imply that all the carbon particles had amorphous porous structures and were partially graphitized through the simple carbonization process, although the complete graphitization requires much higher temperatures (2600 – 3300 °C) [41]. The textural properties of these carbon particles obtained using different mass ratios of KOH/lignin were also assessed by nitrogen adsorption/desorption analysis as depicted in **Figure 4.3(b–d)**. The corresponding structural parameters including specific surface areas and pore characteristics are summarized in **Table 4.2**. The isothermals for all carbon samples in **Figure 4.3(b)** reveal typical type IV adsorption/desorption isotherms, which correspond to micro-mesoporous structures according to the International Union of Pure and Applied Chemistry (IUPAC) classification system [42]. The increased nitrogen uptake capacity in the section of low relative pressures ($P/P_0 < 0.01$) as well as the horizontal plateaus in the section of medium and high relative pressures demonstrate typical microporous structures for these carbon materials. The nitrogen adsorption volumes continually increased over the $P/P_0$ range from 0.1 to 0.5, and the slopes also increased with the increasing KOH/lignin mass ratio, indicating progressive widening of the pores. At higher relative pressures, hysteresis loops between the adsorption and desorption branches are observed, which clearly imply the existence of mesopores in the porous carbons. These results are consistent with the pore size distribution curves for the samples in **Figure 4.3(c)** and **4.3(d)**. As an activating agent, KOH creates micropores and mesopores in the inner and outer surfaces of carbon shell. After washing, these pores are exposed, leading to a change in the specific surface area and pore size distribution considerably. As shown in Figure **4.3(c)** and **4.3(d)**, each specimen possessed a similar porous structure with a uniform micropore

size distribution (0.5 – 1 nm) and a broad mesopore size distribution (2 – 50 nm). As expected, with an increasing amount of KOH, the resulting carbon particles in the samples from **KLC-0.67-700** to **KLC-1.33-700** exhibited both an increase in specific surface area as well as total pore volume. The **KLC-1.33-700** sample showed a large specific surface area of 1996.2 $m^2$ $g^{-1}$ and a high total pore volume of 1.206 $cm^3$ $g^{-1}$, both of which were higher than those of the other samples. This result indicates that the textural characteristics of these HCSs could be optimized by adjusting the KOH/lignin mass ratio. In addition, the specific surface area and total pore volume decreased slightly to 1854.6 $m^2$ $g^{-1}$ and 1.116 $cm^3$ $g^{-1}$, respectively, at the highest KOH/lignin mass ratio of 1.50. This phenomenon could be attributed to the overoxidation of carbon such that $CO_2$ or CO gases were generated from the activating agent. A greater amount of KOH addition would also be expected to cause pore blockage based on the deposition of potassium species, thereby decreasing the specific surface area and pore volume. Similar findings, such as damaged pores resulting from excessive KOH activation, have also been reported in other literatures [43,44]. Therefore, in the present study, the optimal KOH/lignin mass ratio of 1.33 was the most effective for achieving the best specific surface area and pore texture.

**(a)**

**(b)**

**(c)**

**(d)**
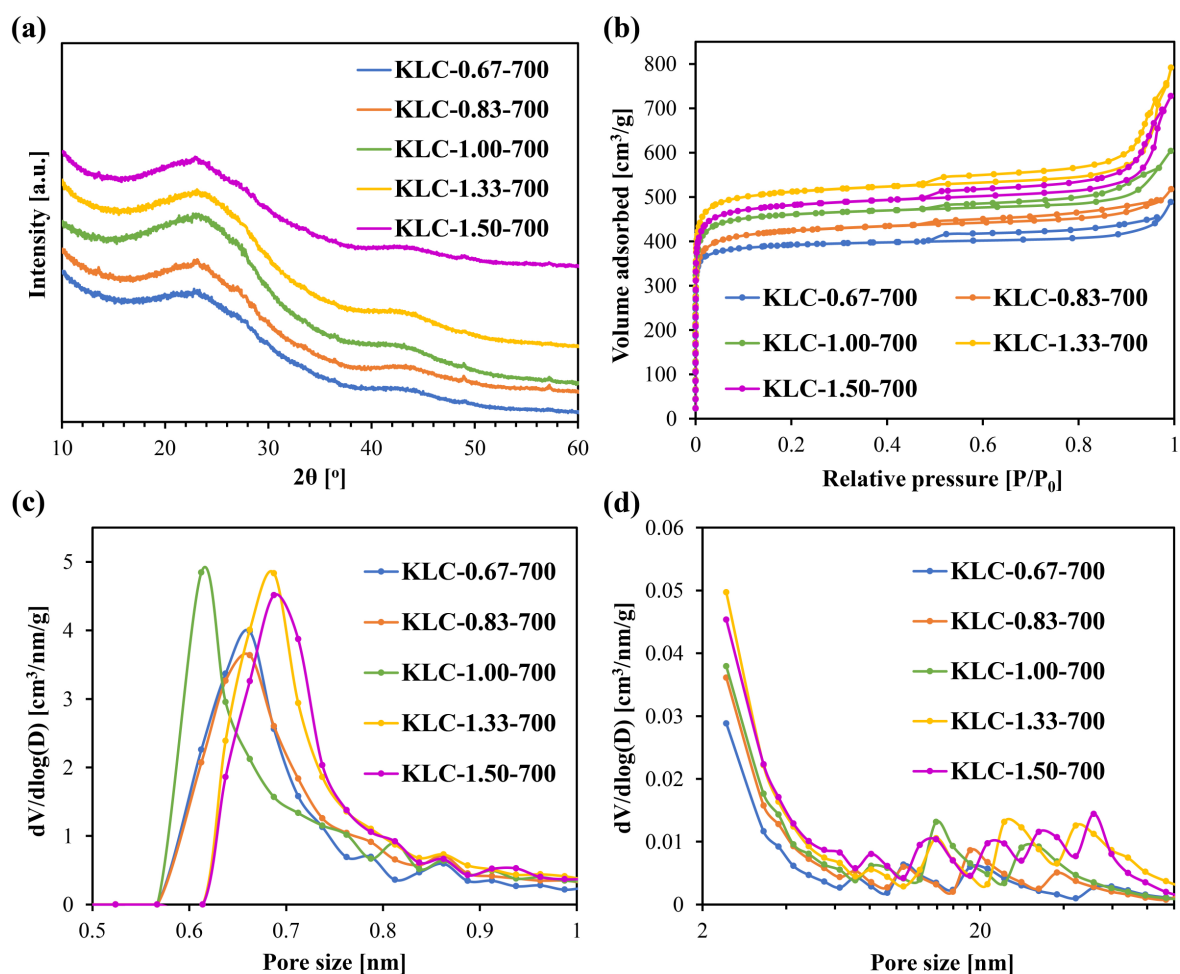


**Figure 4.3.** (a) XRD patterns, (b) nitrogen adsorption/desorption isotherms, and pore size distributions as determined by the (c) HK and (d) BJH methods for the **KLC-X-700** series (where X represents the mass ratio of KOH to lignin, X = 0.67, 0.83, 1.00, 1.33, 1.50).

**Table 4.2.** Textural properties of the **KLC-X-700** (X = 0.67, 0.83, 1.00, 1.33, 1.50) samples.

| Sample name | Specific surface area | Total pore volume | Micropore volume | Mesopore volume |
|---|---|---|---|---|
| | $[m^2\,g^{-1}]$ | $[cm^3\,g^{-1}]$ | $[cm^3\,g^{-1}]$ | $[cm^3\,g^{-1}]$ |
| **KLC-0.67-700** | 1536.5 | 0.750 | 0.596 | 0.091 |
| **KLC-0.83-700** | 1633.1 | 0.795 | 0.640 | 0.130 |
| **KLC-1.00-700** | 1779.4 | 0.929 | 0.699 | 0.177 |
| **KLC-1.33-700** | 1996.2 | 1.206 | 0.774 | 0.253 |
| **KLC-1.50-700** | 1854.6 | 1.116 | 0.728 | 0.227 |

The effect of the carbonization temperature on the final structure of the **KLC-1.33** particles was examined by applying temperatures from 700 to 900 °C. The SEM and TEM images in **Figure 4.4(a-1–c-1)** and **4.4(a-2–c-2)**, respectively, demonstrate that the resulting carbon particles retained their structural integrity and spherical morphology with hollow structure, indicating the high quality of our synthesis method. The nitrogen adsorption/desorption isotherms and pore size distributions of the carbon particles prepared using a KOH/lignin mass ratio of 1.33 with different carbonization temperatures are shown in **Figure 4.4(d–f)**, while details of the surface textural characteristics including specific surface areas and pore structure parameters for all samples are provided in **Table 4.3**. As illustrated in **Figure 4.4(d)**, all isotherm curves of the **KLC-1.33-700**, **KLC-1.33-800**, and **KLC-1.33-900** belong to type IV with clear hysteresis loops, indicating that each one had a porous structure composed of micropores and mesopores [42]. As the carbonization temperature was increased from 700 to 900 °C, the specific surface areas and total pore volumes were gradually increased. From the results, the **KLC-1.33-900** was found to have the highest specific surface area and total pore volume in comparison with the other two samples, with values of 2424.8 $m^2\,g^{-1}$ and 1.566 $cm^3\,g^{-1}$, respectively. These results demonstrate that increasing the carbonization temperature greatly enhanced pore development during the activation process. This effect is also evident in the pore size distribution

curves presented in **Figure 4.4(e)** and **4.4(f)**. The pore size distributions of all the carbon samples are mainly centered at 0.7 and 2.4 nm, indicating that both micropores and mesopores were generated. The formation of this porous structure can be ascribed to the initial redox reaction between carbon and KOH, which is a well-studied chemical activation method for producing activated carbon in previously reported literature [45,46]. Furthermore, the increased pore volumes that occurred with no changes in the overall pore size distributions indicate that the application of different carbonization temperatures as well as the use of KOH as an activator in this study did not restructure these materials, which was in good accordance with the result of SEM and TEM images in **Figure 4.4(a-1–c-1)** and **4.4(a-2–c-2)**, respectively. In addition, the specific surface areas and total pore volumes of the HCSs in this study were larger than those previously reported for porous carbon particles made using KOH as an activation agent in conjunction with various kinds of biomass (**Figure 4.4(g)** and **Table 4.4**). In comparison with some previous literatures, high specific surface areas and pore volumes typically required a mass ratio between KOH and precursor higher than 3:1. This requirement was mainly due to the migration of the activation process from the exterior to the interior of the materials, meaning that a larger amount of KOH was needed to maintain the reaction for preparing suitable activated carbon. Nevertheless, based on life cycle assessment, using a high amount of KOH is not eco-friendly and high corrosive behavior, which is not in accordance with the principles of green chemistry. From an industrial point of view, in our work, using a suitable amount of KOH (KOH/lignin mass ratio below 1.5) will decrease energy consumption and thus have an impact on the overall sustainability of the process.
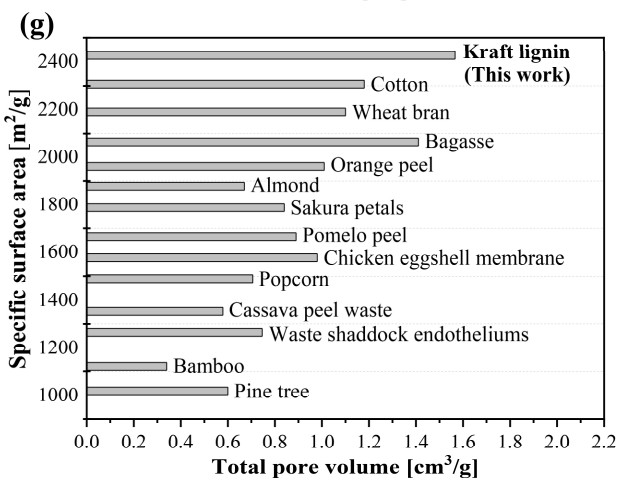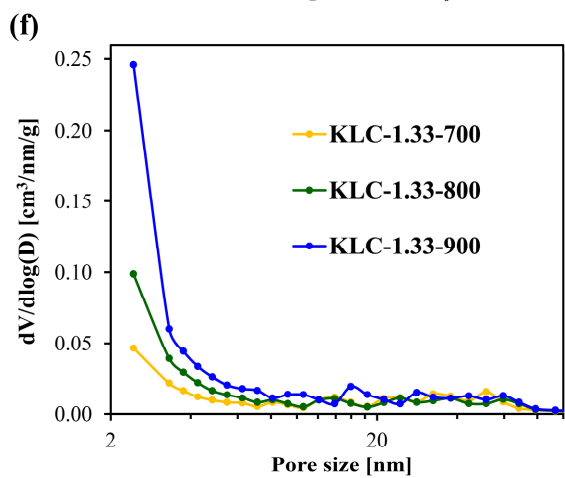
**Figure 4.4.** SEM (up) and TEM (down) images of carbon particles derived from Kraft lignin at carbonization temperatures of (a) 700 °C (**KLC-1.33-700**), (b) 800 °C (**KLC-1.33-800**), and (c) 900 °C (**KLC-1.33-900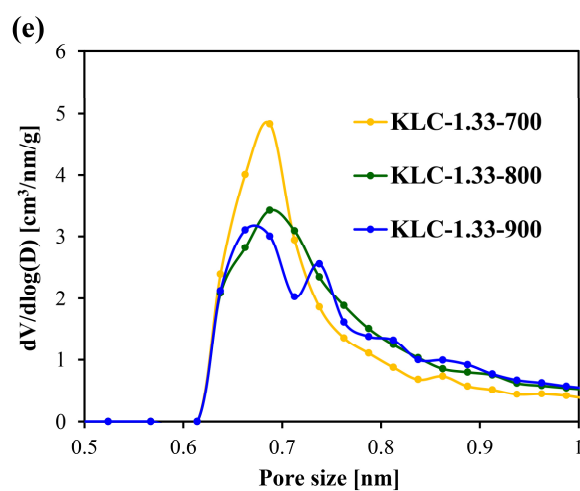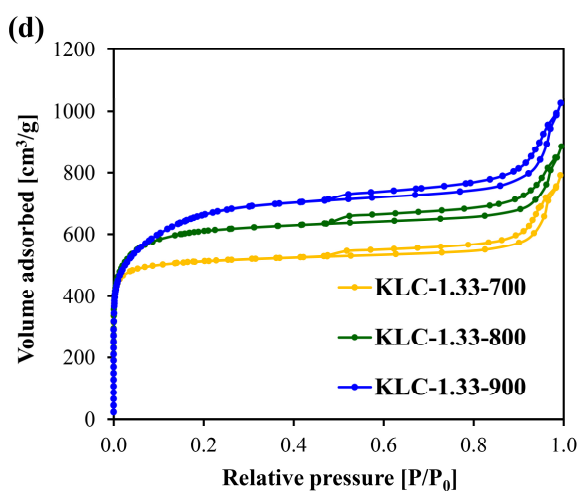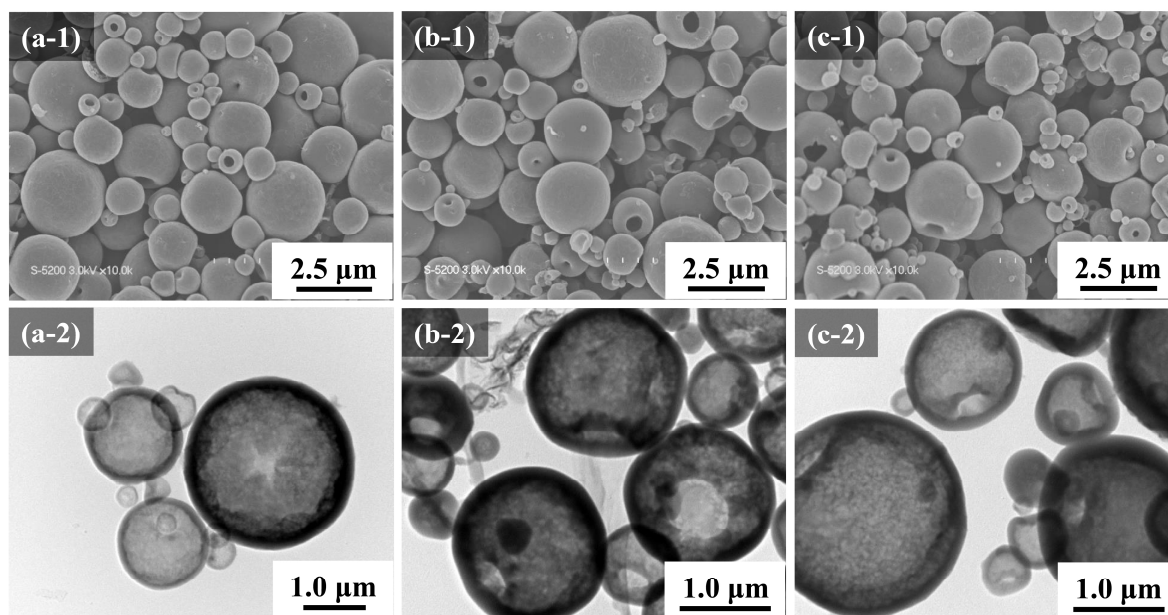**); (d) nitrogen adsorption/desorption isotherms, and pore size distributions as determined by the (e) HK and (f) BJH methods for the **KLC-1.33-Y** series (where Y indicates the carbonization temperature, Y = 700, 800, 900 °C); (g) a comparison of the surface characteristics of previously reported porous carbon particles made using KOH as an activation agent with various types of biomass.

**Table 4.3.** Textural properties of the **KLC-1.33-Y** (Y = 700, 800, 900 °C) samples.

| Sample name | Specific surface area | Total pore volume | Micropore volume | Mesopore volume |
|---|---|---|---|---|
| | $[m^2\,g^{-1}]$ | $[cm^3\,g^{-1}]$ | $[cm^3\,g^{-1}]$ | $[cm^3\,g^{-1}]$ |
| **KLC-1.33-700** | 1996.2 | 1.206 | 0.774 | 0.253 |
| **KLC-1.33-800** | 2207.3 | 1.341 | 0.904 | 0.276 |
| **KLC-1.33-900** | 2424.8 | 1.566 | 0.934 | 0.467 |

**Table 4.4.** Comparison of the textural properties of porous carbon particles made using KOH as an activation agent from various kinds of biomass in the literature and in this study.

| | Precursor (P) | Ratio (KOH/P) | Temp. [°C] [a] | SSA [m²/g] [b] | TPV [cm³/g] [c] | Type of pores | Ref. |
|---|---|---|---|---|---|---|---|
| 1 | **Kraft lignin (This work)** | 1.33 | **700** | **1996.2** | **1.206** | **Micro and mesopores** | |
| | | | **800** | **2207.3** | **1.341** | | |
| | | | **900** | **2424.8** | **1.566** | | |
| 2 | Aloe vera | 3 | 700 | 1890 | 0.167 | Mesopores | [47] |
| 3 | Cotton | 4 | 800 | 1536 | 0.77 | Micropores | [48] |
| | | 5 | | 1898 | 0.98 | | |

| | | 6 | | 2307 | 1.18 | | |
|---|---|---|---|---|---|---|---|
| 4 | Pine tree | 4 | 850 | 1018 | 0.60 | Micro and mesopores | [49] |
| 5 | Orange peel | 0.5 | 800 | 1004 | 0.52 | Micro and mesopores | [50] |
| | | 1 | | 1391 | 0.72 | | |
| | | 2 | | 1960 | 1.01 | | |
| 6 | Pine cone | 1 | 700 | 1210 | 0.29 | Micro, meso and macropores | [51] |
| | | | 800 | 1515 | 0.38 | | |
| | | | 900 | 1128 | 0.36 | | |
| 7 | Human hair | 2 | 700 | 1054 | 0.38 | Micro and mesopores | [52] |
| | | | 800 | 1306 | 0.90 | | |
| | | | 900 | 669 | 0.45 | | |
| 8 | Tobacco rods | 3 | 800 | 1761 – 2115 | 1.00 – 1.22 | Micro, meso and macropores | [53] |
| 9 | Argan seed shells | 4 | 800 | 2132 | 0.96 | Micro and mesopores | [54] |
| 10 | Pistachio nutshell | 3 | 750 | 1069 | 0.51 | Micropores | [55] |
| 11 | Cattail wool | 4 | 800 | 1815 | 1.077 | Micro, meso and macropores | [56] |
| 12 | Sakura petals | 3 | 750 | 1137.7 | 0.69 | Micro, meso and macropores | [57] |
| | | 4 | | 1433.8 | 0.78 | | |
| | | 5 | | 1785.4 | 0.84 | | |
| 13 | Bamboo | 1 | 800 | 1120 | 0.34 | Large micropores with some mesopores | [58] |
| 14 | Pomelo peels | 1 | 750 | 1665 | 0.89 | Micro and | [59] |

| | | | | | | mesopores | |
|---|---|---|---|---|---|---|---|
| 15 | Soybean residue | 2 | 700 | 1950 | 0.82 | Micropores | [60] |
| | | | 800 | 2130 | 0.92 | | |
| 16 | Torreya grandis shell | 1 | 800 | 1974.5 | 0.18 | Micro and mesopores | [61] |
| | | 2 | | 1943.1 | 1.30 | | |
| | | 3 | | 2100.8 | 1.02 | | |
| 17 | Sunflower seed shell | 1 | 700 | 936 | 0.50 | Micro and mesopores | [62] |
| | | 2 | | 1309 | 0.68 | | |
| 18 | Cheery stones | 3 | 800 | 1167 | 0.56 | Micropores | [63] |
| | | | 900 | 1624 | 0.67 | | |
| 19 | Cassava peel waste | 2.5 | 750 | 1352 | 0.579 | Micro and mesopores | [64] |
| 20 | Waste shaddock endotheliums | 1 | 750 | 863 | 0.481 | Micro, meso and macropores | [65] |
| | | 2 | | 1265 | 0.746 | | |
| | | 3 | | 901 | 0.512 | | |
| 21 | Wheat bran | 2 | 800 | 2189.2 | 1.1 | Micro and mesopores | [66] |
| 22 | Acacia gum | 3 | 700 | 1179 | 0.72 | Micropores | [67] |
| | | | 800 | 1832 | 1.04 | | |
| | | | 900 | 1764 | 1.06 | | |
| 23 | Fir wood | 0.5 | 780 | 891 | 0.61 | Micro and mesopores | [68] |
| | | 1 | | 1371 | 0.81 | | |
| | | 4 | | 2179 | 1.24 | | |
| 24 | Poplar catkin | 4 | 800 | 1893 | 1.495 | Micro, meso and macropores | [69] |

| No. | Material | | | | | | Ref. |
|-----|----------|---|-----|--------|------|---------------------------------|------|
| 25 | Bagasse | 3 | 700 | 1892.4 | 0.86 | Micro, meso and macropores | [70] |
| | | | 800 | 1641.6 | 0.80 | | |
| | | | 900 | 2064.8 | 1.41 | | |
| 26 | Shrimp shell | 4 | 700 | 1113 | 0.68 | Micro, meso and macropores | [71] |
| | | | 800 | 1343 | 0.73 | | |
| 27 | Willow catkin | 0.5 | 850 | 1026 | 0.63 | Micro and mesopores | [72] |
| | | 1 | | 1589 | 0.89 | | |
| | | 2 | | 1431 | 0.96 | | |
| 28 | Eucalyptus sawdust | 2 | 700 | 1390 | 0.69 | Micro and mesopores | [73] |
| | | | 800 | 1940 | 0.97 | | |
| 29 | Bean dreg | 0.5 | 700 | 1060 | 0.52 | Micro and mesopores | [74] |
| | | | 800 | 1134 | 0.68 | | |
| | | | 900 | 1193 | 0.71 | | |
| | | 1 | | 1316 | 0.63 | | |
| | | 2 | 700 | 1395 | 0.86 | | |
| | | 3 | | 2040 | 0.89 | | |
| 30 | Rice husk | 4 | 700 | 1759 | 0.79 | Micro and mesopores | [75] |
| | | | 750 | 1930 | 0.97 | | |
| 31 | Artemia cyst shell | 2 | 700 | 1758 | 0.76 | Micro, meso and macropores | [76] |
| 32 | Chicken eggshell membrane | 4 | 700 | 1575 | 0.98 | Micropores | [77] |
| 33 | Soybean milk powder | 4 | 700 | 965 | 0.5 | Micro, meso and macropores | [78] |
| 34 | Bamboo shoot shells | 1 | 700 | 1351 | 0.533 | Micro and | [79] |

| | | | | | | | Micro and mesopores | |
|---|---|---|---|---|---|---|---|---|
| 35 | Cotton seed husk | 1 | 700 | 1694 | 0.87 | Micro and mesopores | [80] |
| | | | 800 | 2063 | 1.07 | | |
| 36 | Redwood cone | 3 | 700 | 1831 | 0.92 | Micro and mesopores | [81] |
| | | | 800 | 1625 | 0.81 | | |
| 37 | Rose multiflora | 3 | 800 | 1646.7 | 0.84 | Micro and mesopores | [82] |
| 38 | Walnut shell | 3 | 800 | 1436.1 | 0.624 | Micro and mesopores | [83] |
| | | 4 | | 1723.9 | 0.852 | | |
| 39 | Almond | 2.4 | 700 | 1677.5 | 0.60 | Micro and mesopores | [84] |
| | | | 800 | 1877.8 | 0.67 | | |
| | | | 900 | 1769.2 | 0.61 | | |
| 40 | Nettle leaves | 1.33 | 800 | 1507 | 1.152 | Micro, meso and macropores | [85] |
| | | 2 | 700 | 1373 | 0.868 | | |
| | | | 800 | 1951 | 1.374 | | |
| | | | 900 | 1351 | 1.216 | | |
| | | 4 | 800 | 1055 | 0.986 | | |
| 41 | Soybean root | 3 | 800 | 1708 | 0.62 | Micro and mesopores | [86] |
| | | 4 | | 2143 | 0.94 | | |
| | | 4.5 | | 1937 | 0.72 | | |
| 42 | Peach gum | 3 | 700 | 1535 | 0.71 | Micro and mesopores | [87] |
| 43 | Enteromorpha prolifera (EP) | 2 | 700 | 1528 | 0.66 | Micro and mesopores | [88] |
| | | | 800 | 1979 | 0.85 | | |
| 44 | Bacillus subtilis | 4 | 800 | 1578 | 1.092 | Micro and mesopores | [89] |

| | | | | | | |
|----|---|---|---|---|---|---|
| 45 | Agaricus | 0.5 | 700 | 1479 | 0.71 | Micropores | [90] |
| | | 2 | | 1742 | 0.82 | | |
| | | 4 | | 2264 | 1.02 | | |
| | | 5 | | 1778 | 1.02 | | |
| 46 | Bamboo fungus | 1 | 800 | 1708 | 0.71 | Micro and mesopores | [91] |
| 47 | Cashmere | 3 | 800 | 1358 | 1.23 | Micro and mesopores | [92] |
| 48 | Mussel nacre | 2 | 800 | 2141.3 | 0.3038 | Micro, meso and macropores | [93] |
| | | 3 | | 2329.1 | 0.2239 | | |
| | | 4 | | 2331.0 | 0.1342 | | |
| | | 5 | | 2205.6 | 0.2209 | | |
| 49 | Porcine bladders | 1 | 700 | 1568.4 | 0.68 | Micro and mesopores | [94] |
| | | 2 | | 1881.7 | 0.83 | | |
| | | 3 | | 2079.3 | 0.98 | | |
| 50 | Squid gladius | 1 | 750 | 1129 | 0.141 | Micro and mesopores | [95] |
| 51 | Bristlegrass seeds | 6 | 700 | 1135 | 0.60 | Micro, meso and macropores | [96] |
| | | | 800 | 1484 | 0.84 | | |
| | | | 900 | 1435 | 0.83 | | |
| 52 | Eleocharis dulcis | 1 | 800 | 1063 | 0.352 | Micro and mesopores | [97] |
| | | 2 | | 1708 | 0.729 | | |
| 53 | Green algae Chlorella zofingiensis | 2 | 700 | 1337.9 | 0.597 | Micro and mesopores | [98] |
| 54 | Popcorn | 0.5 | 800 | 867 | 0.406 | Abundant micropores with little | [99] |
| | | 1 | | 1248 | 0.588 | | |

| | | | | | | |
|---|---|---|---|---|---|---|
| | | 2 | | 1489 | 0.706 | amount of mesopores |
| 55 | Hemp stem | 1 | 800 | 1276 | 0.73 | Micro and mesopores |
| | | 2 | | 1397 | 0.80 | |
| | | 3 | | 1764 | 1.05 | [100] |
| 56 | Metaplexis japonica | 4 | 750 | 1394 | 0.79 | Micro and mesopores |
| | | | | | | [101] |
| 57 | Loofah sponge | 2 | 700 | 1177 | 0.55 | Micro and mesopores |
| | | | 800 | 1733 | 0.86 | |
| | | | 900 | 1841 | 1.05 | [102] |
| 58 | Cicada slough | 0.5 | 800 | 1243 | 0.568 | Abundant micropores and a small quantity of mesopores |
| | | 1 | | 1483 | 0.673 | |
| | | 2 | | 1745 | 0.730 | [103] |

[a] Activation temperature [$^{o}$C]

[b] Specific surface area [m$^2$/g]

[c] Total pore volume [cm$^3$/g]

### 4.3.2. Electrochemical evaluation of HCSs derived from Kraft lignin

To evaluate the electrochemical performance of the HSC samples in their intended use as electrode materials for supercapacitors, electrochemical measurements are conducted in a two-electrode system with an aqueous 6 M KOH solution as the electrolyte. The GCD curves obtained from the **KLC-1.33-Y** (Y = 700, 800, 900 $^{o}$C) samples at a current density of 0.2 A g$^{-1}$ are displayed in **Figure 4.5(a)**. As can be clearly seen, each of these data plots is close to linear, demonstrating that these materials behaved as ideal electrical double-layer capacitors with good diffusion of the electrolyte inside the pores [104]. Additionally, each GCD curve shows a similar discharge time, indicating that it has similar gravimetric specific capacitance values. From the data in **Table 4.5**, the gravimetric specific capacitance values of the **KLC-1.33-700**, **KLC-1.33-**

**800**, and **KLC-1.33-900** specimens at a current density of 0.2 A g$^{-1}$ were calculated to be 29.4, 31.1, and 31.8 F g$^{-1}$, respectively, all of which are higher than that of the commercially available activated carbon Kuraray YP-50F (29.2 F g$^{-1}$). With the increase in the carbonization temperature, the specific surface areas of each of the **KLC-1.33-Y** samples was increased (more than 2000 m$^2$ g$^{-1}$), however, the specific capacitance values were not significantly improved. Some previous studies have demonstrated that the theoretical specific capacitance of carbon material in an electrolyte can be calculated according to this equation: $C = \varepsilon_r\varepsilon_0 A/d$, where $\varepsilon_r$ is the relative dielectric constant of the electrolyte, $\varepsilon_0$ is the dielectric constant of a vacuum, $A$ is the electrode surface area, and $d$ is the effective thickness of the double layer (that is, the charge separation distance) [105]. This equation shows that the specific capacitance is directly proportional to the surface area of the electrode material. Therefore, we assumed that the use of a high carbonization temperature can enhance the specific surface area of the material, which is favorable to the specific capacitance performance. However, in the present work, although we identified a positive correlation between the specific surface area and gravimetric specific capacitance, the enhancement of specific capacitance values was not significantly improved. A relationship between these two factors (*e.g.* specific surface area and gravimetric specific capacitance) for carbon materials has been frequently observed in prior research, and this phenomenon can be attributed to several factors, namely (i) the formation of pores during the activation process that is smaller than the size of electrolyte ions, leading to the entry of the electrolyte into the pores difficult and a fraction of the surface area being underutilized; (ii) decomposition of the electrolyte at active sites on the carbon electrode; (iii) poor electrical conductivity and high interparticle resistance caused by a low electrode density; and (iv) an affinity of the carbon surface for the electrolyte solution resulting from wettability or hydrophilicity/hydrophobicity [26,106]. In this work, the specific surface areas were determined by nitrogen adsorption/desorption, and an aqueous KOH solution was used as the electrolyte. The diameter of nitrogen is 0.363 nm [105], while the bare and hydrated ion sizes of K$^+$ are 0.133 and 0.331 nm, and those of the OH$^-$ ion are 0.176 and 0.300 nm, respectively [107]. Therefore, the pores accessible to nitrogen molecules would also be available for the dehydrated K$^+$ and OH$^-$. It is also reasonable to assume that if the electrode material is completely wetted and the supercapacitor is charged/discharged at a sufficiently low rate so as to maintain

thermodynamic equilibrium, all the surface area determined from nitrogen adsorption/desorption data would be accessed by the dehydrated ions, and this would make a positive contribution to the specific capacitance. In addition, the inorganic KOH electrolyte would not be expected to decompose at active sites in the potential range applied. Based on the discussions above, reasons (i) and (ii) can be reasonably ruled out. Therefore, it can be concluded that although the specific surface area is an important parameter, the electrode density was most likely the primary factor determining the specific capacitance of the samples. In general, a low electrode density will lead to reducing the volumetric energy density in a supercapacitor because a greater amount of electrolyte will be required to fill the significant void space in the electrode [108]. As shown in **Table 4.5**, the electrode density values of the **KLC-1.33-700**, **KLC-1.33-800**, and **KLC-1.33-900** samples were calculated to be 0.63, 0.50, and 0.46 g cm$^{-3}$, respectively. These values are relatively low and would be expected to seriously lower the specific capacitance. According to these explanations, we would expect the capacitance to be increased in the case of samples with high specific surface areas and high electrode densities compared with samples having higher specific surface areas but low electrode densities. This is the reason why the **KLC-1.33-900** specimen showed a higher specific surface area (2424.8 m$^2$ g$^{-1}$) than the **KLC-1.33-700** (1996.2 m$^2$ g$^{-1}$) and **KLC-1.33-800** (2207.3 m$^2$ g$^{-1}$) but only a slight increase in the specific capacitance because the former had a lower electrode density. Therefore, in our future plan, along with the basic requirements to have a high specific surface area and large pore volume, it would be highly desirable to optimize the synthesis conditions to obtain particles having high electrode densities and appropriate pore structures so as to provide ideal supercapacitor electrode materials.

The capacitive performances of the **KLC-1.33-Y** electrodes were assessed by carrying out EIS measurements using a symmetric supercapacitor cell. **Figure 4.5(b)** presents the EIS spectra and Nyquist plots of these **KLC-1.33-Y** electrodes. Generally, the Nyquist plot exhibits a semicircle in the high-frequency region with a straight line at 90° in the low-frequency region [12,106]. The diameter of the semicircle represents the charge transfer resistance between the electrode and electrolyte interface, while the straight line at 90° indicates the double layer capacitance. It is apparent from **Figure 4.5(b)** that, in contrast to the **KLC-1.33-700** and **KLC-1.33-800** electrodes, the **KLC-1.33-900** electrode showed a straight line at 90° and no obvious semicircle in the spectra, which characterize the feature of low resistance between the electrolyte

and electrode with a high double layer capacitance. These results indicate that the **KLC-1.33-900** electrode had a better pore structure along with a suitable pore size distribution and good connectivity of pores. These features would promote rapid diffusion of ions between the electrode and the electrolyte interface, which in turn could enhance the capacitance.
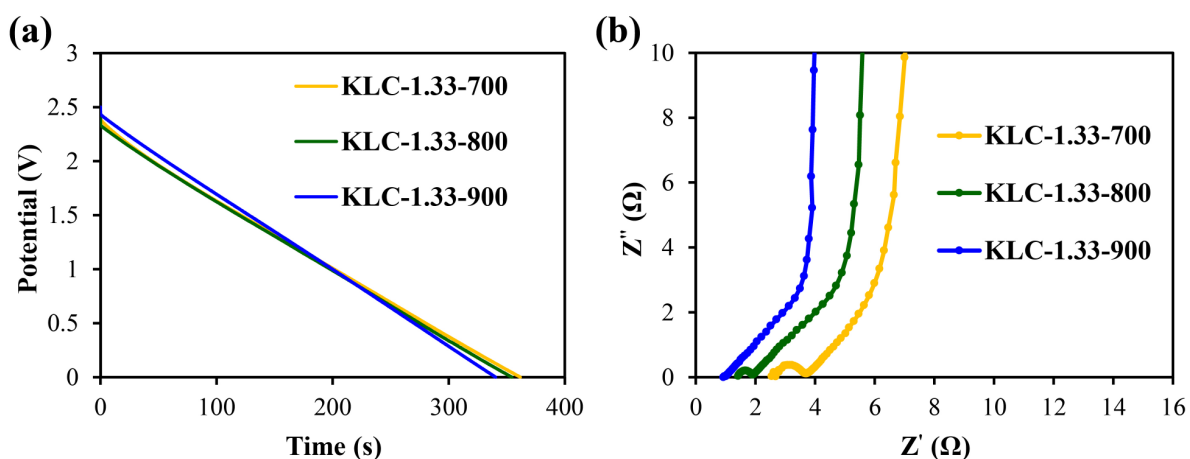


**Figure 4.5.** (a) GCD curves acquired at a current density of 0.2 A g$^{-1}$ and (b) Nyquist plots for the **KLC-1.33-Y** (Y = 700, 800, 900 °C) samples.

**Table 4.5.** Specific capacitance and electrode density values for the **KLC-1.33-Y** (Y = 700, 800, 900 °C) and commercially available activated carbon Kuraray YP-50F samples.

| Sample name | Specific capacitance | Electrode density |
|---|---|---|
| | [F g$^{-1}$] | [g cm$^{-3}$] |
| **KLC-1.33-700** | 29.4 | 0.63 |
| **KLC-1.33-800** | 31.1 | 0.50 |
| **KLC-1.33-900** | 31.8 | 0.46 |
| **Kuraray YP-50F** | 29.2 | 0.71 |

## 4.4. Conclusions

In summary, HCSs derived from sustainable and abundant biomass Kraft lignin have been successfully synthesized through a template-free spray drying method followed by a carbonization process. This fabrication system is simple, cost-effective, applicable to large-scale production, does not require polymeric surfactants or copolymers, and uses much less amount of KOH, which is in accordance with the green chemistry principles. The resulting carbon particles can be obtained with spherical morphologies and hollow structures, high specific surface areas up to 2424.8 $m^2$ $g^{-1}$ with micro-mesoporous structure by simply tuning the KOH concentration. In addition, these HCSs can be used as electrode materials in supercapacitors for energy storage applications. The two-electrode supercapacitor based on HCSs showed a specific capacitance value of 31.8 F $g^{-1}$ at a current density of 0.2 A $g^{-1}$, which is higher than that obtained from the commercial activated carbon Kuraray YP-50F (29.2 F $g^{-1}$). In future, the precise optimization of these HCSs to obtain high electrode densities with appropriate pore structures has the potential for exploiting in electrochemical applications. These promising properties in conjunction with the green synthesis approach in the present work suggest intriguing strategies for the design of HCSs as advanced materials from Kraft lignin as a low-cost raw material. These particles could improve the electrochemical performances of various energy storage and conversion devices.

## 4.5. References

[1]     J. Qi, X. Lai, J. Wang, H. Tang, H. Ren, Y. Yang, Q. Jin, L. Zhang, R. Yu, G. Ma, Z. Su, H. Zhao, D. Wang, Multi-shelled hollow micro-/nanostructures, Chem. Soc. Rev. 44 (2015) 6749–6773.

[2]     L. Zhou, Z. Zhuang, H. Zhao, M. Lin, D. Zhao, L. Mai, Intricate hollow structures: controlled synthesis and applications in energy storage and conversion, Adv. Mater. 29 (2017) 1602914.

[3]     T. Ogi, A.B.D. Nandiyanto, K. Okuyama, Nanostructuring strategies in functional fine-particle synthesis towards resource and energy saving applications, Adv. Powder Technol. 25 (2014) 3–17.

[4]     E.M. Schneider, S. Taniguchi, Y. Kobayashi, S.C. Hess, R. Balgis, T. Ogi, K. Okuyama, W.J. Stark, Efficient recycling of poly(lactic acid) nanoparticle templates for the synthesis of hollow silica spheres, ACS Sustain. Chem. Eng. 5 (2017) 4941–4947.

[5]     K.L.A. Cao, S. Taniguchi, T.T. Nguyen, A.F. Arif, F. Iskandar, T. Ogi, Precisely tailored synthesis of hexagonal hollow silica plate particles and their polymer nanocomposite films with low refractive index, J. Colloid Interface Sci. 571 (2020) 378–386.

[6]     L. Yu, H. Bin Wu, X.W.D. Lou, Self-templated formation of hollow structures for electrochemical energy applications, Acc. Chem. Res. 50 (2017) 293–301.

[7]     R. Balgis, T. Ogi, W.N. Wang, G.M. Anilkumar, S. Sago, K. Okuyama, Aerosol synthesis of self-organized nanostructured hollow and porous carbon particles using a dual polymer system, Langmuir 30 (2014) 11257–11262.

[8]     Y. Yang, S. Zhang, L. Gu, S. Shao, W. Li, D. Zeng, F. Yang, S. Hao, Stable yolk-structured catalysts towards aqueous levulinic acid hydrogenation within a single Ru nanoparticle anchored inside the mesoporous shell of hollow carbon spheres, J. Colloid Interface Sci. 576 (2020) 394–403.

[9]     Y. Xia, X. Na, J. Wu, G. Ma, The horizon of the emulsion particulate strategy: Engineering hollow particles for biomedical applications, Adv. Mater. 31 (2019) 1–18.

[10]    S. Asgari, A. Pourjavadi, S.H. Hosseini, S. Kadkhodazadeh, A pH-sensitive carrier based-on modified hollow mesoporous carbon nanospheres with calcium-latched gate for drug delivery, Mater. Sci. Eng. C 109 (2020) 110517.

[11]    J. Du, L. Liu, Y. Yu, Z. Hu, B. Liu, A. Chen, N-doped hollow carbon spheres/sheets composite for electrochemical capacitor, ACS Appl. Mater. Interfaces 10 (2018) 40062–40069.

[12]    K.L.A. Cao, A.F. Arif, K. Kamikubo, T. Izawa, H. Iwasaki, T. Ogi, Controllable synthesis of carbon-coated $SiO_x$ particles through a simultaneous reaction between the hydrolysis-condensation of tetramethyl orthosilicate and the polymerization of 3-aminophenol, Langmuir 35 (2019) 13681–13692.

[13] S. Li, A. Pasc, V. Fierro, A. Celzard, Hollow carbon spheres, synthesis and applications–a review, J. Mater. Chem. A 4 (2016) 12686–12713.

[14] A.F. Arif, Y. Kobayashi, E.M. Schneider, S.C. Hess, R. Balgis, T. Izawa, H. Iwasaki, S. Taniguchi, T. Ogi, K. Okuyama, W.J. Stark, Selective low-energy carbon dioxide adsorption using monodisperse nitrogen-rich hollow carbon submicron spheres, Langmuir 34 (2018) 30–35.

[15] A.F. Arif, Y. Kobayashi, R. Balgis, T. Ogi, H. Iwasaki, K. Okuyama, Rapid microwave-assisted synthesis of nitrogen-functionalized hollow carbon spheres with high monodispersity, Carbon 107 (2016) 11–19.

[16] W. Long, B. Fang, A. Ignaszak, Z. Wu, Y.J. Wang, D. Wilkinson, Biomass-derived nanostructured carbons and their composites as anode materials for lithium ion batteries, Chem. Soc. Rev. 46 (2017) 7176–7190.

[17] D.W. Lee, M.H. Jin, J.H. Park, Y.J. Lee, Y.C. Choi, Flexible synthetic strategies for lignin-derived hierarchically porous carbon materials, ACS Sustain. Chem. Eng. 6 (2018) 10454–10462.

[18] D. Kai, M.J. Tan, P.L. Chee, Y.K. Chua, Y.L. Yap, X.J. Loh, Towards lignin-based functional materials in a sustainable world, Green Chem. 18 (2016) 1175–1200.

[19] B.M. Upton, A.M. Kasko, Strategies for the conversion of lignin to high-value polymeric materials: Review and perspective, Chem. Rev. 116 (2016) 2275–2306.

[20] S. Chatterjee, T. Saito, Lignin-derived advanced carbon materials, ChemSusChem 8 (2015) 3941–3958.

[21] H. Qin, R. Jian, J. Bai, J. Tang, Y. Zhou, B. Zhu, D. Zhao, Z. Ni, L. Wang, W. Liu, Q. Zhou, X. Li, Influence of molecular weight on structure and catalytic characteristics of ordered mesoporous carbon derived from lignin, ACS Omega 3 (2018) 1350–1356.

[22] M.J. Valero-Romero, E.M. Márquez-Franco, J. Bedia, J. Rodríguez-Mirasol, T. Cordero, Hierarchical porous carbons by liquid phase impregnation of zeolite templates with lignin

solution, Microporous Mesoporous Mater. 196 (2014) 68–78.

[23]  A. Xie, J. Dai, X. Chen, P. Ma, J. He, C. Li, Z. Zhou, Y. Yan, Ultrahigh adsorption of typical antibiotics onto novel hierarchical porous carbons derived from renewable lignin via halloysite nanotubes-template and in-situ activation, Chem. Eng. J. 304 (2016) 609–620.

[24]  Z.W. He, J. Yang, Q.F. Lü, Q. Lin, Effect of structure on the electrochemical performance of nitrogenand oxygen-containing carbon micro/nanospheres prepared from lignin-based composites, ACS Sustain. Chem. Eng. 1 (2013) 334–340.

[25]  D. Saha, E.A. Payzant, A.S. Kumbhar, A.K. Naskar, Sustainable mesoporous carbons as storage and controlled-delivery media for functional molecules, ACS Appl. Mater. Interfaces 5 (2013) 5868–5874.

[26]  D. Saha, Y. Li, Z. Bi, J. Chen, J.K. Keum, D.K. Hensley, H.A. Grappe, H.M. Meyer, S. Dai, M.P. Paranthaman, A.K. Naskar, Studies on supercapacitor electrode material from activated lignin-derived mesoporous carbon, Langmuir 30 (2014) 900–910.

[27]  A.B.D. Nandiyanto, T. Ogi, W.N. Wang, L. Gradon, K. Okuyama, Template-assisted spray-drying method for the fabrication of porous particles with tunable structures, Adv. Powder Technol. 30 (2019) 2908–2924.

[28]  T. Ogi, H. Fukazawa, A.M. Rahmatika, T. Hirano, K.L.A. Cao, F. Iskandar, Improving the crystallinity and purity of monodisperse Ag fine particles by heating colloidal sprays in-flight, Ind. Eng. Chem. Res. 59 (2020) 5745–5751.

[29]  L. Gradon, R. Balgis, T. Hirano, A.M. Rahmatika, T. Ogi, K. Okuyama, Advanced aerosol technologies towards structure and morphologically controlled next-generation catalytic materials, J. Aerosol Sci. 149 (2020) 105608.

[30]  K.L.A. Cao, A.M. Rahmatika, Y. Kitamoto, M.T.T. Nguyen, T. Ogi, Controllable synthesis of spherical carbon particles transition from dense to hollow structure derived from Kraft lignin, J. Colloid Interface Sci. 589 (2021) 252–263.

[31]    A.B.D. Nandiyanto, K. Okuyama, Progress in developing spray-drying methods for the production of controlled morphology particles: From the nanometer to submicrometer size ranges, Adv. Powder Technol. 22 (2011) 1–19.

[32]    E. Lintingre, F. Lequeux, L. Talini, N. Tsapis, Control of particle morphology in the spray drying of colloidal suspensions, Soft Matter. 12 (2016) 7435–7444.

[33]    K. Okuyama, M. Abdullah, I.W. Lenggoro, F. Iskandar, Preparation of functional nanostructured particles by spray drying, Adv. Powder Technol. 17 (2006) 587–611.

[34]    F. Iskandar, L. Gradon, K. Okuyama, Control of the morphology of nanostructured particles prepared by the spray drying of a nanoparticle sol, J. Colloid Interface Sci. 265 (2003) 296–303.

[35]    Z. Zhao, S. Hao, P. Hao, Y. Sang, A. Manivannan, N. Wu, H. Liu, Lignosulphonate-cellulose derived porous activated carbon for supercapacitor electrode, J. Mater. Chem. A 3 (2015) 15049–15056.

[36]    W. Fang, S. Yang, X.-L. Wang, T.-Q. Yuan, R.-C. Sun, Manufacture and application of lignin-based carbon fibers (LCFs) and lignin-based carbon nanofibers (LCNFs), Green Chem. 19 (2017) 1794–1827.

[37]    S. Iravani, R.S. Varma, Greener synthesis of lignin nanoparticles and their applications, Green Chem. 22 (2020) 612–636.

[38]    J. Pang, W. Zhang, J. Zhang, G. Cao, M. Han, Y. Yang, Facile and sustainable synthesis of sodium lignosulfonate derived hierarchical porous carbons for supercapacitors with high volumetric energy densities, Green Chem. 19 (2017) 3916–3926.

[39]    Z.Z. Pan, L. Dong, W. Lv, D. Zheng, Z. Li, C. Luo, C. Zheng, Q.H. Yang, F. Kang, A hollow spherical carbon derived from the spray drying of corncob lignin for high-rate-performance supercapacitors, Chem. - An Asian J. 12 (2017) 503–506.

[40]    G. Singh, I.Y. Kim, K.S. Lakhi, P. Srivastava, R. Naidu, A. Vinu, Single step synthesis of activated bio-carbons with a high surface area and their excellent $CO_2$ adsorption capacity,

Carbon 116 (2017) 448–455.

[41]   N. Sudhan, K. Subramani, M. Karnan, N. Ilayaraja, M. Sathish, Biomass-derived activated porous carbon from rice straw for a high-energy symmetric supercapacitor in aqueous and nonaqueous electrolytes, Energy and Fuels 31 (2017) 977–985.

[42]   K.S.W. Sing, D.H. Everett, R.A.W. Haul, L. Moscou, R.A. Pierotti, J. Rouquerol, T. Siemieniewska, Reporting physisorption data for gas/solid systems with special reference to the determination of surface area and porosity, Pure Appl. Chem. 57 (1985) 603–619.

[43]   S. Yang, S. Wang, X. Liu, L. Li, Biomass derived interconnected hierarchical micro-meso-macro- porous carbon with ultrahigh capacitance for supercapacitor, Carbon 147 (2019) 540–549.

[44]   F. Zhang, G.D. Li, J.S. Chen, Effects of raw material texture and activation manner on surface area of porous carbons derived from biomass resources, J. Colloid Interface Sci. 327 (2008) 108–114.

[45]   J. Wang, S. Kaskel, KOH activation of carbon-based materials for energy storage, J. Mater. Chem. 22 (2012) 23710–23725.

[46]   M.A. Lillo-Ródenas, D. Cazorla-Amorós, A. Linares-Solano, Understanding chemical reactions between carbons and NaOH and KOH: An insight into the chemical activation mechanism, Carbon 41 (2003) 267–275.

[47]   M. Karnan, K. Subramani, N. Sudhan, N. Ilayaraja, M. Sathish, *Aloe vera* derived activated high-surface-area carbon for flexible and high-energy supercapacitors, ACS Appl. Mater. Interfaces 8 (2016) 35191–35202.

[48]   P. Cheng, T. Li, H. Yu, L. Zhi, Z. Liu, Z. Lei, Biomass-derived carbon fiber aerogel as a binder-free electrode for high-rate supercapacitors, J. Phys. Chem. C 120 (2016) 2079–2086.

[49]   X. Wang, Y. Li, F. Lou, M.E. Melandsø Buan, E. Sheridan, D. Chen, Enhancing capacitance of supercapacitor with both organic electrolyte and ionic liquid electrolyte on

a biomass-derived carbon, RSC Adv. 7 (2017) 23859–23865.

[50]   C.K. Ranaweera, P.K. Kahol, M. Ghimire, S.R. Mishra, R.K. Gupta, Orange-peel-derived carbon: Designing sustainable and high-performance supercapacitor electrodes, C 3 (2017) 25.

[51]   N. Manyala, A. Bello, F. Barzegar, A.A. Khaleed, D.Y. Momodu, J.K. Dangbegnon, Coniferous pine biomass: A novel insight into sustainable carbon materials for supercapacitors electrode, Mater. Chem. Phys. 182 (2016) 139–147.

[52]   W. Qian, F. Sun, Y. Xu, L. Qiu, C. Liu, S. Wang, F. Yan, Human hair-derived carbon flakes for electrochemical supercapacitors, Energy Environ. Sci. 7 (2014) 379–386.

[53]   Y.Q. Zhao, M. Lu, P.Y. Tao, Y.J. Zhang, X.T. Gong, Z. Yang, G.Q. Zhang, H.L. Li, Hierarchically porous and heteroatom doped carbon derived from tobacco rods for supercapacitors, J. Power Sources 307 (2016) 391–400.

[54]   A. Elmouwahidi, Z. Zapata-Benabithe, F. Carrasco-Marín, C. Moreno-Castilla, Activated carbons from KOH-activation of argan (*Argania spinosa*) seed shells as supercapacitor electrodes, Bioresour. Technol. 111 (2012) 185–190.

[55]   J. Xu, Q. Gao, Y. Zhang, Y. Tan, W. Tian, L. Zhu, L. Jiang, Preparing two-dimensional microporous carbon from Pistachio nutshell with high areal capacitance as supercapacitor materials, Sci. Rep. 4 (2014) 1–6.

[56]   X.L. Su, S. Jiang, G.P. Zheng, X.C. Zheng, J.H. Yang, Z.Y. Liu, High-performance supercapacitors based on porous activated carbons from cattail wool, J. Mater. Sci. 53 (2018) 1–15.

[57]   F. Ma, S. Ding, H. Ren, Y. Liu, Sakura-based activated carbon preparation and its performance in supercapacitor applications, RSC Adv. 9 (2019) 2474–2483.

[58]   C. Zequine, C.K. Ranaweera, Z. Wang, S. Singh, P. Tripathi, O.N. Srivastava, B.K. Gupta, K. Ramasamy, P.K. Kahol, P.R. Dvornic, R.K. Gupta, High performance and flexible supercapacitors based on carbonized bamboo fibers for wide temperature applications, Sci.

Rep. 6 (2016) 1–10.

[59]   K. Wu, J. Fu, X. Zhang, X. Peng, B. Gao, P.K. Chu, Three-dimensional flexible carbon electrode for symmetrical supercapacitors, Mater. Lett. 185 (2016) 193–196.

[60]   G.A. Ferrero, A.B. Fuertes, M. Sevilla, From Soybean residue to advanced supercapacitors, Sci. Rep. 5 (2015) 1–13.

[61]   H. Xuan, G. Lin, F. Wang, J. Liu, X. Dong, F. Xi, Preparation of biomass-activated porous carbons derived from torreya grandis shell for high-performance supercapacitor, J. Solid State Electrochem. 21 (2017) 2241–2249.

[62]   X. Li, W. Xing, S. Zhuo, J. Zhou, F. Li, S.Z. Qiao, G.Q. Lu, Preparation of capacitor's electrode from sunflower seed shell, Bioresour. Technol. 102 (2011) 1118–1123.

[63]   M. Olivares-Marín, J.A. Fernández, M.J. Lázaro, C. Fernández-González, A. Macías-García, V. Gómez-Serrano, F. Stoeckli, T.A. Centeno, Cherry stones as precursor of activated carbons for supercapacitors, Mater. Chem. Phys. 114 (2009) 323–327.

[64]   A.E. Ismanto, S. Wang, F.E. Soetaredjo, S. Ismadji, Preparation of capacitor's electrode from cassava peel waste, Bioresour. Technol. 101 (2010) 3534–3540.

[65]   S. Yang, S. Wang, X. Liu, L. Li, Biomass derived interconnected hierarchical micro-meso-macro-porous carbon with ultrahigh capacitance for supercapacitor, Carbon 147 (2019) 540–549.

[66]   D. Wang, Y. Min, Y. Yu, Facile synthesis of wheat bran-derived honeycomb-like hierarchical carbon for advanced symmetric supercapacitor applications, J. Solid State Electrochem. 19 (2014) 577–584.

[67]   Y. Fan, P. Liu, B. Zhu, S. Chen, K. Yao, R. Han, Microporous carbon derived from acacia gum with tuned porosity for high-performance electrochemical capacitors, Int. J. Hydrogen Energy 40 (2015) 6188–6196.

[68]   F.C. Wu, R.L. Tseng, C.C. Hu, C.C. Wang, The capacitive characteristics of activated carbons-comparisons of the activation methods on the pore structure and effects of the

pore structure and electrolyte on the capacitive performance, J. Power Sources 159 (2006) 1532–1542.

[69]  X.L. Su, M.Y. Cheng, L. Fu, J.H. Yang, X.C. Zheng, X.X. Guan, Superior supercapacitive performance of hollow activated carbon nanomesh with hierarchical structure derived from poplar catkins, J. Power Sources 362 (2017) 27–38.

[70]  P. Hao, Z. Zhao, J. Tian, H. Li, Y. Sang, G. Yu, H. Cai, H. Liu, C.P. Wong, A. Umar, Hierarchical porous carbon aerogel derived from bagasse for high performance supercapacitor electrode, Nanoscale 6 (2014) 12120–12129.

[71]  F. Gao, J. Qu, C. Geng, G. Shao, M. Wu, Self-templating synthesis of nitrogen-decorated hierarchical porous carbon from shrimp shell for supercapacitors, J. Mater. Chem. A 4 (2016) 7445–7452.

[72]  Y. Li, G. Wang, T. Wei, Z. Fan, P. Yan, Nitrogen and sulfur co-doped porous carbon nanosheets derived from willow catkin for supercapacitors, Nano Energy 19 (2016) 165–175.

[73]  M. Sevilla, A.B. Fuertes, Sustainable porous carbons with a superior performance for $CO_2$ capture, Energy Environ. Sci. 4 (2011) 1765–1771.

[74]  W. Xing, C. Liu, Z. Zhou, L. Zhang, J. Zhou, S. Zhuo, Z. Yan, H. Gao, G. Wang, S.Z. Qiao, Superior $CO_2$ uptake of N-doped activated carbon through hydrogen-bonding interaction, Energy Environ. Sci. 5 (2012) 7323–7327.

[75]  Y. Guo, J. Qi, Y. Jiang, S. Yang, Z. Wang, H. Xu, Performance of electrical double layer capacitors with porous carbons derived from rice husk, Mater. Chem. Phys. 80 (2003) 704–709.

[76]  Y. Zhao, W. Ran, J. He, Y. Song, C. Zhang, D.B. Xiong, F. Gao, J. Wu, Y. Xia, Oxygen-rich hierarchical porous carbon derived from Artemia cyst shells with superior electrochemical performance, ACS Appl. Mater. Interfaces 7 (2015) 1132–1139.

[77]  Z. Li, L. Zhang, B.S. Amirkhiz, X. Tan, Z. Xu, H. Wang, B.C. Olsen, C.M.B. Holt, D.

Mitlin, Carbonized chicken eggshell membranes with 3D architectures as high-performance electrode materials for supercapacitors, Adv. Energy Mater. 2 (2012) 431–437.

[78] M. Chen, D. Yu, X. Zheng, X. Dong, Biomass based N-doped hierarchical porous carbon nanosheets for all-solid-state supercapacitors, J. Energy Storage 21 (2019) 105–112.

[79] J. Han, Q. Li, J. Wang, J. Ye, G. Fu, L. Zhai, Y. Zhu, Heteroatoms (O, N)-doped porous carbon derived from bamboo shoots shells for high performance supercapacitors, J. Mater. Sci. Mater. Electron. 29 (2018) 20991–21001.

[80] H. Chen, G. Wang, L. Chen, B. Dai, F. Yu, Three-dimensional honeycomb-like porous carbon with both interconnected hierarchical porosity and nitrogen self-doping from cotton seed husk for supercapacitor electrode, Nanomaterials 8 (2018) 412.

[81] H. Jia, S. Wang, J. Sun, K. Yin, X. Xie, L. Sun, Nitrogen-doped microporous carbon derived from a biomass waste-metasequoia cone for electrochemical capacitors, J. Alloys Compd. 794 (2019) 163–170.

[82] Q. Chen, J. Sun, Z. Wang, Z. Zhao, Y. Zhang, Y. Liu, L. Hou, C. Yuan, Sustainable rose multiflora derived nitrogen/oxygen-enriched micro-/mesoporous carbon as a low-cost competitive electrode towards high-performance electrochemical supercapacitors, RSC Adv. 8 (2018) 9181–9191.

[83] Y. Wang, H. Jiang, S. Ye, J. Zhou, J. Chen, Q. Zeng, H. Yang, T. Liang, N-doped porous carbon derived from walnut shells with enhanced electrochemical performance for supercapacitor, Funct. Mater. Lett. 12 (2019) 1950042.

[84] F. Zeng, Z. Li, X. Li, J. Wang, Z. Kong, Y. Sun, Z. Liu, H. Feng, Almond-derived origami-like hierarchically porous and N/O co-functionalized carbon sheet for high-performance supercapacitor, Appl. Surf. Sci. 467–468 (2019) 229–235.

[85] W. Fan, H. Zhang, H. Wang, X. Zhao, S. Sun, J. Shi, M. Huang, W. Liu, Y. Zheng, P. Li, Dual-doped hierarchical porous carbon derived from biomass for advanced supercapacitors and lithium ion batteries, RSC Adv. 9 (2019) 32382–32394.

[86]   N. Guo, M. Li, Y. Wang, X. Sun, F. Wang, R. Yang, Soybean root-derived hierarchical porous carbon as electrode material for high-performance supercapacitors in ionic liquids, ACS Appl. Mater. Interfaces 8 (2016) 33626–33634.

[87]   Y. Lin, Z. Chen, C. Yu, W. Zhong, Heteroatom-doped sheet-like and hierarchical porous carbon based on natural biomass small molecule peach gum for high-performance supercapacitors, ACS Sustain. Chem. Eng. 7 (2019) 3389–3403.

[88]   M. Ren, Z. Jia, Z. Tian, D. Lopez, J. Cai, M.M. Titirici, A.B. Jorge, High performance N-doped carbon electrodes obtained via hydrothermal carbonization of Macroalgae for supercapacitor applications, ChemElectroChem 5 (2018) 2686–2693.

[89]   H. Zhu, J. Yin, X. Wang, H. Wang, X. Yang, Microorganism-derived heteroatom-doped carbon materials for oxygen reduction and supercapacitors, Adv. Funct. Mater. 23 (2013) 1305–1312.

[90]   J. Wang, Q. Liu, Fungi-derived hierarchically porous carbons for high-performance supercapacitors, RSC Adv. 5 (2015) 4396–4403.

[91]   Z. Zou, Y. Lei, Y. Li, Y. Zhang, W. Xiao, Nitrogen-doped hierarchical meso/microporous carbon from bamboo fungus for symmetric supercapacitor applications, Molecules 24 (2019) 3677.

[92]   L. Zhou, H. Cao, S. Zhu, L. Hou, C. Yuan, Hierarchical micro-/mesoporous N- and O-enriched carbon derived from disposable cashmere: A competitive cost-effective material for high-performance electrochemical capacitors, Green Chem. 17 (2015) 2373–2382.

[93]   S. Lv, L. Ma, Q. Zhou, X. Shen, H. Tong, Three-dimensional self-doped hierarchical porous mussel nacre-derived carbons for high performance supercapacitors, J. Mater. Sci. Mater. Electron. 30 (2019) 14382–14390.

[94]   D. Wang, Z. Xu, Y. Lian, C. Ban, H. Zhang, Nitrogen self-doped porous carbon with layered structure derived from porcine bladders for high-performance supercapacitors, J. Colloid Interface Sci. 542 (2019) 400–409.

[95]   C.J. Raj, M. Rajesh, R. Manikandan, K.H. Yu, J.R. Anusha, J.H. Ahn, D.W. Kim, S.Y. Park, B.C. Kim, High electrochemical capacitor performance of oxygen and nitrogen enriched activated carbon derived from the pyrolysis and activation of squid gladius chitin, J. Power Sources 386 (2018) 66–76.

[96]   W. Zhou, S. Lei, S. Sun, X. Ou, Q. Fu, Y. Xu, Y. Xiao, B. Cheng, From weed to multi-heteroatom-doped honeycomb-like porous carbon for advanced supercapacitors: A gelatinization-controlled one-step carbonization, J. Power Sources 402 (2018) 203–212.

[97]   J. Zhou, S. Ye, Q. Zeng, H. Yang, J. Chen, Z. Guo, H. Jiang, K. Rajan, Nitrogen and phosphorus co-doped porous carbon for high-performance supercapacitors, Front. Chem. 8 (2020) 1–8.

[98]   B. Zhu, B. Liu, C. Qu, H. Zhang, W. Guo, Z. Liang, F. Chen, R. Zou, Tailoring biomass-derived carbon for high-performance supercapacitors from controllably cultivated algae microspheres, J. Mater. Chem. A 6 (2018) 1523–1530.

[99]   T. Liang, C. Chen, X. Li, J. Zhang, Popcorn-derived porous carbon for energy storage and $CO_2$ capture, Langmuir 32 (2016) 8042–8049.

[100]  Y. Wang, R. Yang, M. Li, Z. Zhao, Hydrothermal preparation of highly porous carbon spheres from hemp (*Cannabis sativa* L.) stem hemicellulose for use in energy-related applications, Ind. Crops Prod. 65 (2015) 216–226.

[101]  C. Liang, J. Bao, C. Li, H. Huang, C. Chen, Y. Lou, H. Lu, H. Lin, Z. Shi, S. Feng, One-dimensional hierarchically porous carbon from biomass with high capacitance as supercapacitor materials, Microporous Mesoporous Mater. 251 (2017) 77–82.

[102]  Y. Luan, L. Wang, S. Guo, B. Jiang, D. Zhao, H. Yan, C. Tian, H. Fu, A hierarchical porous carbon material from a loofah sponge network for high performance supercapacitors, RSC Adv. 5 (2015) 42430–42437.

[103]  J. Zhou, L. Bao, S. Wu, W. Yang, H. Wang, Chitin based heteroatom-doped porous carbon as electrode materials for supercapacitors, Carbohydr. Polym. 173 (2017) 321–329.

[104] C. Ma, Z. Li, J. Li, Q. Fan, L. Wu, J. Shi, Y. Song, Lignin-based hierarchical porous carbon nanofiber films with superior performance in supercapacitors, Appl. Surf. Sci. 456 (2018) 568–576.

[105] M. Salanne, B. Rotenberg, K. Naoi, K. Kaneko, P.L. Taberna, C.P. Grey, B. Dunn, P. Simon, Efficient storage mechanisms for building better supercapacitors, Nat. Energy 1 (2016) 16070.

[106] J. Pang, W.F. Zhang, J.L. Zhang, H.M. Zhang, G.P. Cao, M.F. Han, Y.S. Yang, Oxygen and nitrogen co-enriched sustainable porous carbon hollow microspheres from sodium lignosulfonate for supercapacitors with high volumetric energy densities, ChemElectroChem 5 (2018) 1306–1320.

[107] C. Zhong, Y. Deng, W. Hu, J. Qiao, L. Zhang, J. Zhang, A review of electrolyte materials and compositions for electrochemical supercapacitors, Chem. Soc. Rev. 44 (2015) 7484–7539.

[108] J.R. Rani, R. Thangavel, S.I. Oh, J.M. Woo, N. Chandra Das, S.Y. Kim, Y.S. Lee, J.H. Jang, High volumetric energy density hybrid supercapacitors based on reduced graphene oxide scrolls, ACS Appl. Mater. Interfaces 9 (2017) 22398–22407.

# Chapter 5

# Conclusions and Future Perspectives

Significant advances have been achieved in the fabrication of spherical carbon-based materials with well-designed morphologies, manipulated porosity, and adjustable functionalities. A special focus has been placed on the synthetic strategies and functionalization of carbon spheres with controllable sizes, structures, surface properties, and their utilization for energy storage devices, such as LIBs and supercapacitors. It is therefore understandable that engineering the carbon sphere materials is a good approach to improve the performance of LIBs and supercapacitors. This dissertation encompasses nanostructuration and functionalization of carbon spheres as a part of engineering the carbon and demonstrates the fabrication of feasible spherical carbon-based materials. The major highlights of this dissertation comprise the following points.

1. The fabrication of carbon-coated $SiO_x$ ($SiO_x@C$) core−shell particles with spherical morphology and excellent lithium storage performance has been developed via a sol-gel method followed by the carbonization process. Results from this study provide new insight into the design of core−shell particles by using TMOS as an alternative silica precursor rather than conventionally used TEOS for the first time with a well-controlled reaction rate and spherical morphology. In addition, to obtain an in-depth understanding of the formation of core−shell structure, a possible mechanism is also proposed in this research. When tested as an anode material for LIBs, the obtained $SiO_x@C$ particles delivered a reversible capacity of 509.2 mAh $g^{-1}$ at a current density of 100 mA $g^{-1}$. This electrochemical performance is significantly better than those of similar composites without the core−shell structure. The capacity retention after 100 cycles was approximately 80%. These results suggest great promise for the proposed $SiO_x@C$ particles with core−shell structure, which may have potential applications in the improvement of various energy-storage materials.

2. With regard to the synthesis and practical applications of nanostructured materials, the fabrication of carbon materials with perfectly spherical shapes using a simple procedure would be highly beneficial for diverse applications. Therefore, the carbon spheres have been

143

successfully synthesized through a spray drying method followed by the carbonization process, using Kraft lignin as the carbon source and KOH as the activation agent. The proposed method successfully controlled the shape and structure of the carbon particles from dense to hollow by tuning the KOH concentration. Especially, this research represents the first demonstration that KOH plays a crucial role in the formation of particles with good sphericity and dense structures. Furthermore, to get a better understanding of the particle formation of carbon particles, a plausible mechanism is also discussed in this study. The resulting spherical carbon particles exhibited dense structures with a specific surface area (1233 $m^2$ $g^{-1}$) and tap density (1.46 g $cm^{-3}$) superior to those of irregular shape carbon particles. The carbon sphere particles having a high tap density as advanced materials can endow them for a broad prospect of applications in the areas of colloids and interface science as well as sustainable development.

3. Building on our previously reported work, the precise design of hollow carbon spheres (HCSs) with high specific surface area derived from Kraft lignin using an appropriate amount of KOH has been developed through a spray drying technique followed by a simple carbonization process. The high specific surface area (1536.5–2424.8 $m^2$ $g^{-1}$) with micro-mesoporous structure of HCSs can be easily tuned by controlling the mass ratio of KOH to carbon precursor. The KOH-to-lignin mass ratios were utilized below 1.5, lower than those in previous studies typically used higher than 3, which was in accordance with green chemistry principles. In addition, these HCSs have applications as electrode materials in supercapacitors for energy storage devices. The two-electrode supercapacitor based on HCSs showed a specific capacitance value of 31.8 F $g^{-1}$ at a current density of 0.2 A $g^{-1}$, which is higher than that obtained from the commercial activated carbon Kuraray YP-50F (29.2 F $g^{-1}$). These promising properties in conjunction with the green synthesis approach in the present work suggest intriguing strategies for the design of HCSs as advanced materials from Kraft lignin as a low-cost raw material. These particles could improve the electrochemical performances of various energy storage and conversion devices.

Despite significant progresses have been made on both the synthesis and application in energy storage devices, some challenges still exist to be addressed. The understanding over the structure-performance relationships of carbon sphere materials is still in the early stage.

Comprehensive studies are much needed to get in-depth insights in the near future, which are very important for developing new advanced spherical carbon-based materials.

1.   As the anode material for LIBs: carbon spheres have been extensively employed because they are versatile and it is easy to tune their porosity and other structural parameters. Among them, the ones with a core−shell structure and porous shells are especially attractive because they are able to host a series of active species, which can provide them with sufficient electronic conductivity. This is essential for maintaining the stable cycling of these species and their full utilization as well. To enhance the electrochemical performance of spherical carbon-based materials, the particle size, pore size, and structure of the carbon spheres with surface modification should be precisely tailored, so that the number of exposed active sites can be optimized and mass transfer can be improved.

2. As the electrode material for supercapacitors: porous carbon spheres have been employed as the electrode materials for commercial EDLC devices. The spherical structure can decrease the transmission distance of electrolyte ions, so that the electric double-layer can be easily formed between the electrolyte and electrode. However, along with the basic requirements to have a high specific surface area and large pore volume, it would be highly desirable to optimize the synthesis conditions to obtain particles having high electrode densities and appropriate pore structures so as to provide ideal supercapacitor electrode materials.

# List of Publications

1. **K.L.A. Cao**, A.F. Arif, K. Kamikubo, T. Izawa, H. Iwasaki, T. Ogi, Controllable synthesis of carbon-coated $SiO_x$ particles through a simultaneous reaction between the hydrolysis-condensation of tetramethyl orthosilicate and the polymerization of 3-aminophenol, *Langmuir* 35 (2019) 13681–13692.

2. **K.L.A. Cao**, S. Taniguchi, T.T. Nguyen, A.F. Arif, F. Iskandar, T. Ogi, Precisely tailored synthesis of hexagonal hollow silica plate particles and their polymer nanocomposite films with low refractive index, *Journal of Colloid and Interface Science* 571 (2020), 378–386.

3. T. Ogi, H. Fukazawa, A.M. Rahmatika, T. Hirano, **K.L.A. Cao**, F. Iskandar, Improving the crystallinity and purity of monodisperse Ag fine particles by heating colloidal sprays in-flight, *Industrial and Engineering Chemistry Research* 59 (2020), 5745–5751.

4. **K.L.A. Cao**, A.M. Rahmatika, Y. Kitamoto, M.T.T. Nguyen, T. Ogi, Controllable synthesis of spherical carbon particles transition from dense to hollow structure derived from Kraft lignin, *Journal of Colloid and Interface Science* 589 (2021), 252–263.

5. **K.L.A. Cao**, Y. Kitamoto, F. Iskandar, T. Ogi, Sustainable porous hollow carbon spheres with high specific surface area derived from Kraft lignin, *Advanced Powder Technology* 32 (2021), 2064–2073.

6. T.T. Nguyen, A.M. Rahmatika, M. Miyauchi, **K.L.A. Cao**, T. Ogi, Synthesis of high specific surface area macroporous pectin particles by a template-assisted spray drying, *Langmuir* 37 (2021), 4256–4266.

7. E.L. Septiani, J. Kikkawa, **K.L.A. Cao**, T. Hirano, N. Okuda, H. Matsumoto, Y. Enokido, T. Ogi, Direct synthesis of submicron FeNi particles via spray pyrolysis using multiple reduction agents, *Advanced Powder Technology*, under review.

# List of Presentations at Conferences

1. **K.L.A. Cao**, T. Ogi: Controllable synthesis of carbon coated $SiO_x$ particles through a simultaneous reaction between hydrolysis-condensation of tetramethyl orthosilicate and polymerization of 3-aminophenol, Powder Engineering Society-Fall, Osaka, Japan, October 15, 2019 (oral presentation).

2. **K.L.A. Cao**, T. Ogi: Facile synthesis of SiOx@C core−shell particles as the anode material for lithium-ion batteries, National Central University-Hiroshima University Joint Symposium on Materials Chemistry and Physics, Taiwan, November 1, 2019 (***Excellent Poster Award***).

3. 上久保一希, **K.L.A. Cao**, 荻 崇: マイクロ波加熱を利用した $SiO_x$/カーボンコアシェル粒子の制御合成と電池性能評価, 第 57 回粉体に関する討論会 (2019/11/26 広島)

4. **K.L.A. Cao**, T. Izawa, T. Ogi: Facile and efficient synthesis of $SiO_x$@C core−shell particles as an anode material for lithium-ion batteries, SCEJ 85th Annual Meeting and IChES, Osaka, Japan, March 17, 2020 (oral presentation).

5. **K.L.A. Cao**, T. Ogi: Controllable synthesis of hexagonal hollow silica plate particles and their low refractive index in polymer nanocomposite films, SCEJ 51st Autumn Meeting, September 24, 2020 (online presentation).

6. 北本 泰彦, **K.L.A. Cao**, 荻 崇: 噴霧乾燥法によるリグニン由来ポーラスカーボン粒子の合成と特性評価, 第 23 回化学工学会学生発表会（2021/3/6 オンライン開催）

7. T. Ogi, **K.L.A. Cao**: Synthesis of porous, hollow, core-shell structured carbon particles and their electrode applications, K-3 Recent Progress in Energy Conversion and Storage - Nanomaterials Synthesis - in SCEJ 86th Annual Meeting/IChES, March 21, 2021 (online presentation).

8. T.T. Nguyen, **K.L.A. Cao**, 宮内 正人, 荻 崇, : Preparation of Micro-Meso-Macroporous Pectin Particles via Spray Drying, 粉体工学会 2021 年度春期研究発表会 (2021/6/3, オンライン開催).

# Acknowledgement

I would like to show my sincere gratefulness for my Professor Takashi Ogi, who always supported me for all the years in Japan, supervised my research, gave me valuable comments and suggestion for writing the good paper. He also gave me an opportunity to get a Doctoral degree from Hiroshima University. I really appreciate it.

I wish to thank you Professor Mai Thanh Thi Nguyen and Professor Nhan Trung Nguyen for their great support and give me a chance to study at Hiroshima University. My grateful thank is also dedicated to Professor Ferry Iskandar, Dr. Aditya Farhan Arif, Dr. Shuhei Nakakura, and Dr. Annie Mufyda Rahmatika for their suggestion to improve the quality of my manuscript and guidance during my research.

I also want to send my thanks to all members of the Thermal Fluid Materials Engineering Laboratory, special mention goes to Mrs. Tachibana, Hirano, Kamikubo, Taniguchi, Fukazawa, Kikkawa, Eka, Toyoda, Kitou, Tue, Wang, Kitamoto, Kaseda, Tsuboi, Phong, Narui, and Yamashita for their kindness and warm support when I studied in the laboratory. It has been a very memorable time that I have spent with them.

I would also like to thank the Ministry of Education, Culture, Sports, Science and Technology (MEXT) of Japan for proving a doctoral scholarship and the Hosokawa Foundation for supporting the research fund.

Last but not least, I would like to sincerely thank my father Long, my mother Thuy, and my younger brother Khoa in the home country that always give me their biggest love and support. They give me encouragement and motivation during my doctoral study in Japan. Their love also gives me the spirit to complete my study well.

Kiet Le Anh Cao

Higashi Hiroshima, July 2021